STRESS, BOREHOLE STABILITY, AND HYDROCARBON LEAKAGE IN THE NORTHERN NORTH SEA

A DISSERTATION

SUBMITTED TO THE DEPARTMENT OF GEOPHYSICS

AND THE COMMITTEE ON GRADUATE STUDIES

OF STANFORD UNIVERSITY

IN PARTIAL FULFILLMENT OF THE REQUIREMENTS

FOR THE DEGREE OF

DOCTOR OF PHILOSOPHY

David Wiprut

February 2001

I certify that I have read this dissertation and that in my opinion it is fully adequate, in scope and quality, as a dissertation for the degree of Doctor of Philosophy.

_____

Mark D. Zoback (Principal Advisor)

I certify that I have read this dissertation and that in my opinion it is fully adequate, in scope and quality, as a dissertation for the degree of Doctor of Philosophy.

_____

Amos M. Nur

I certify that I have read this dissertation and that in my opinion it is fully adequate, in scope and quality, as a dissertation for the degree of Doctor of Philosophy.

_____

Gary Mavko

Approved for the University Committee on Graduate Studies:

_____

Abstract

Knowledge of the state of stress in hydrocarbon reservoirs is critical for maintaining wellbore stability as well as for understanding the processes of hydrocarbon migration and leakage. The principal goals in this dissertation are to constrain the full in-situ stress tensor using drilling-induced tensile fractures and wellbore breakouts; to determine optimal trajectories for maintaining wellbore stability; and to evaluate potential hydrocarbon leakage and migration pathways in the context of dynamic mechanisms which control fluid flow. I analyze data in four fields in the northern North Sea.

In the Visund field west of the Viking graben, stress analysis obtained using drilling-induced tensile fractures indicates the field has a consistently orientated stress tensor as well as magnitudes of the principal stresses consistent with the strike-slip to reverse faulting stress field observed from earthquake focal plane mechanisms. Analysis of wellbore stability shows that horizontal wells drilled in the direction of the maximum horizontal stress in this field are the most successful. Observations of gas leakage along a normal fault which is optimally oriented for reverse failure in the current stress field are correlated with predictions of leakage. I show that Coulomb frictional failure along well-oriented faults can account for gas leakage from this field.

In the Field 1, Field 2, and Field 3, stress analysis indicates the fields generally have consistently oriented stress tensors and magnitudes of the principal stresses consistent with the strike-slip faulting stress field observed from earthquake focal plane mechanisms. Observations of gas leakage and migration in Field 3, and observations of large pore pressure differences across faults in Field 1 and Field 2, are correlated with predictions of leakage and sealing. I show that predictions of probable leakage and migration in Field 3 can be matched with actual observations of up-fault leakage as well as observations of along fault migration to the south. I also show that predictions of a large sealing potential in Field 1 and Field 2 are matched with quite large pore pressure differences across faults which are poorly oriented for frictional failure in the current stress field.

Pore pressures and hydrocarbon column heights in individual fields appear to be controlled by the potential for reservoir-bounding faults to slip. Fields located in areas with high differential stresses and faults well-oriented for frictional failure tend to have small hydrocarbon column heights, while those with lower stresses and poorly-oriented faults tend to have higher column heights.

Acknowledgments

Quite a few people have helped me in a number of ways to complete this work. First, and of course foremost, I thank Mark Zoback for his guidance and support during my time at Stanford. His insights and enthusiasm have been inspirational, and I feel lucky to have had him as my advisor. I thank Bjorn Larsen, whose proposal to Mark initiated this project, and whose insights have continued to move this project forward over the years. I thank Norsk Hydro for providing me with both the data and financial support for completing this thesis. Thanks to Tor-Harald Hanssen, Linn Arnesen, Nils Telnæs, Chris Dart, Nils Kageson-Loe, Roald Færseth and Paul Gillespie for helping me acquire the data I needed. I especially thank Linn Arnesen and Nils Kageson-Loe for their efforts to provide me with data and for their constructive criticism of this work. My proposal committee members Steve Graham, Amos Nur, and Gary Mavko gave constructive criticism of my work early on, and Steve along with Norm Sleep, George Thompson, and Jerry Harris served on my thesis defense committee. Balz Grollimund has been a great friend and collaborator throughout this project. My discussions with him about our projects greatly improved my work as well as my understanding of stresses in the North Sea.

Thanks also to the people in my research group and the department who have been my friends over the years. I thank Balz Grollimund, Lourdes Colmenares, Carl Chang, Thomas Finkbeiner, Paul Hagin, Stephanie Prejean, and Wendy Wempe whose support and friendship helped me through quite a few difficult days. I especially thank Balz and Lourdes for being such great friends. It has been a pleasure to be a part of their lives together. Thanks to Linda Farwell, Jeannette Ochoa, Laurie Reynolds, and Margaret Muir for their help with administrative and publishing matters.

Finally, I thank my family for their support over the years. My parents and brother Jim have always been here for me, and that has always been a great source of comfort.

Table of Contents

CHAPTER 1

INTRODUCTION - STRESS, BOREHOLE STABILITY, AND HYDROCARBON LEAKAGE IN THE NORTHERN NORTH SEA

1.1 Abstract

Stresses in the earth play a critical role in many geologic processes and engineering problems. In this dissertation I specifically address the process by which stresses are measured and constrained, and how those results can be applied to a number of problems. By relying almost exclusively on drilling-induced tensile fractures seen in exploration wells drilled into four fields, a map of a consistently oriented stress field emerges. Problems such as wellbore stability and hydrocarbon leakage and migration in the northern North Sea can also be addressed once the stress tensor is constrained. Without a well constrained stress tensor predictions about wellbore stability are not possible, and calculations of resolved stresses on faults are unreliable. I show that the maximum horizontal stress is larger than the vertical stress, and the minimum horizontal stress is less than, but nearly equal to the vertical stress in every field investigated. These findings are consistent with the strike-slip to reverse fault stress field seen from earthquake focal-plane mechanisms. I apply the stresses measured in Visund to a single well in order to determine what mud weight should have been used while drilling the well. The analysis and results match precisely with the mud weight used in the wellbore. This well was the most successful well in the Visund field in terms of minimizing lost time during drilling. I also explore the relationship between the in-situ stress and hydrocarbon leakage along reactivated faults in the northern North Sea. I show that even in a relatively static or slowly deforming sedimentary basin such as exists in the North Sea, the stress and pore pressure measurements and observations of leakage are consistent with the observations of Barton et al. (1995), and the leakage mechanism proposed by and Sibson (1990), and Finkbeiner et al. (2001). I also show that the pore pressure never exceeds the critical pore pressure predicted by Coulomb frictional failure. I speculate that if this is the case in sedimentary basins throughout the earth, then hydrofacturing will never take place unless all of the faults bounding the reservoir are almost optimally mis-oriented for frictional slip in the current stress field.

1.2 Introduction

Stresses in the earth play a critical role in many geologic processes and engineering problems. For example, the migration path of hydrocarbons may be determined by stresses in the earth and wells may collapse as a result of the stresses they encounter as they are drilled. In this dissertation I specifically address the process by which stresses are measured, and how those results can be applied to problems such as wellbore stability and

hydrocarbon leakage and migration in the northern North Sea. The northern North Sea contains large hydrocarbon reservoirs found primarily in mid- to early-Jurassic age sedimentary basins. Total production on the Norwegian shelf consists of over 6.6 billion barrels of oil and 400 billion cubic meters of gas. The remaining reserves consist of approximately 8.3 billion barrels of oil and 1.35 trillion cubic meters of gas. These deposits are of interest to over 15 companies currently operating in the northern North Sea. As a result of this work, the cost-effectiveness of drilling to produce hydrocarbons may be greatly improved during both the development and production of new fields in the northern North Sea and in other parts of the world.

1.3 Constraining the Stress Orientation

Constraining the orientation of the stress tensor is a problem that was first effectively addressed by Zoback and Zoback (1980). In 1989, Zoback and Zoback set forth a quality ranking system for stress orientation data which established a qualitative measure of the reliability of the data and the degree to which different stress indicators represent the tectonic stress field. By throwing away unreliable data, and ranking the rest of the data by reliability, a clear and consistent picture of stresses in the earth began to emerge. This study represents the first almost exclusive use of drilling-induced tensile fractures to determine the orientation of the present-day stress field in the northern North Sea. Drilling-induced tensile fractures form as a result of the stress concentration around a wellbore drilled into anisotropically-stressed rock, and form in the direction of the maximum horizontal stress. Because this is a relatively new technique for constraining the in-situ stress, a new quality ranking system had to be created to asses the reliability of this data. An extension to the quality ranking system of Zoback and Zoback (1989) is presented in Appendix A for drilling-induced tensile fractures.

Before this study was undertaken, stress orientation measurements in the northern North Sea showed a great deal of variability. For example, stress orientation measurements from the World Stress Map project show that there is appreciable scatter in the orientation of the maximum horizontal stress in the North Sea (Figure 1, Müller et al., 1993). Despite a consistently oriented stress field in both England and northern Europe, there was a persistent idea that the stress orientations in the North Sea were the result of real changes in the stress field, rather than poor data. Similar maps from other parts of the world show that the stress field is typically consistent throughout a region (Zoback, 1992; Zoback & Zoback, 1989).

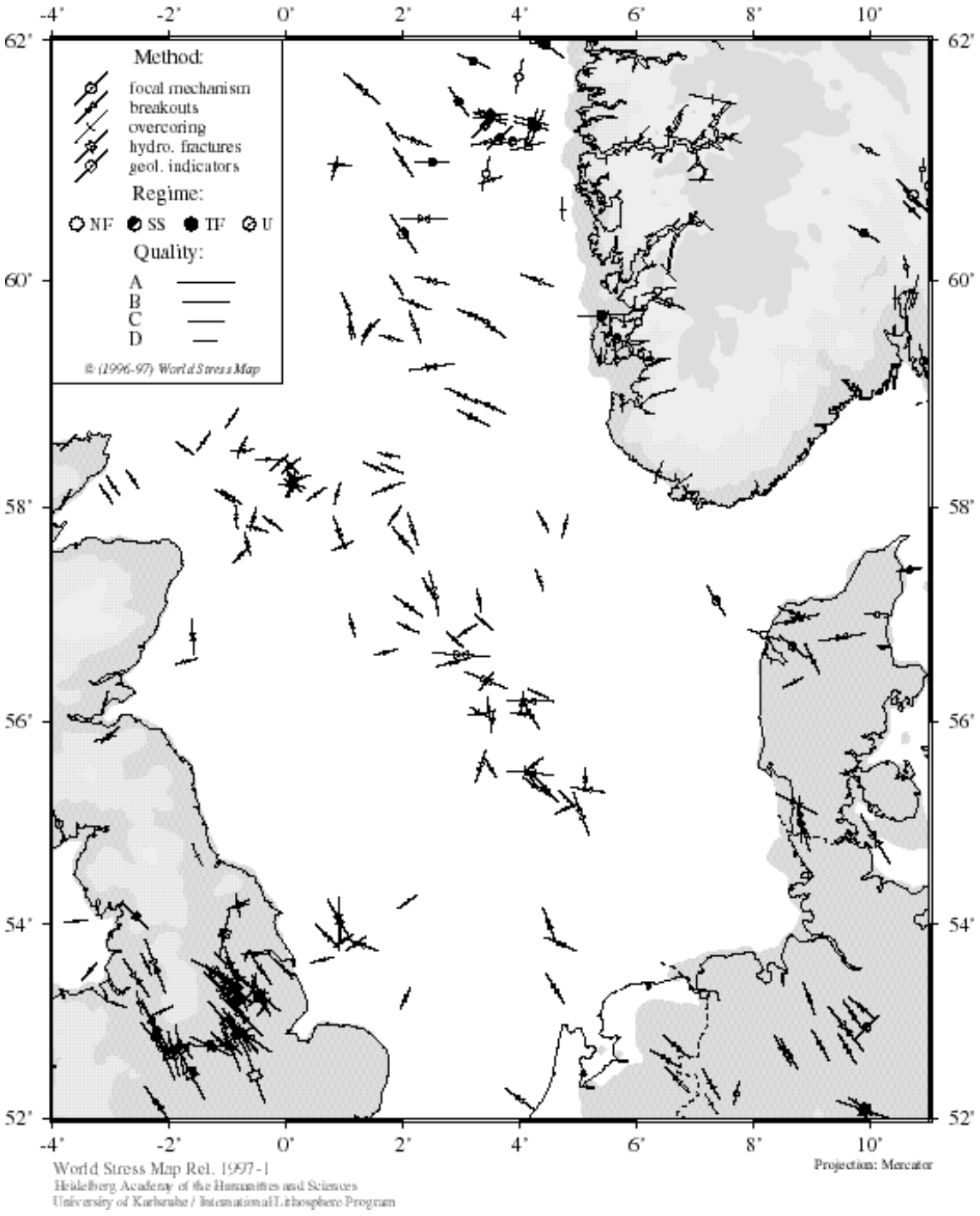

Figure 1.1: Map of maximum horizontal stress orientations from World Stress Map project (Zoback, 1992). Note that stress orientations are consistent in England and northern Europe, but are quite scattered in the North Sea. The majority of data come from breakout analyses conducted in hydrocarbon exploration wells.

One mechanism proposed to explain the scatter in the data was that the sediments in the North Sea were decoupled from the deeper basement. Fejerskov (1996) proposed that the decoupling could be seen at the Cretaceous unconformity. Using wellbore elongations in the Visund field to determine the orientation of the maximum horizontal stress, his data showed a wide range of orientations not only across a single field but within individual wells (Figure 2). Fejerskov assumed that all of the apparent breakout orientations he observed were representative of the stress field. Some investigators working in Field 3, described later in this thesis, proposed that differing stress orientations resulted from local causes rather than being representative of regional tectonic stresses (Figure 3). Considering the high variability of the data, the orientation of the tectonic stress is unclear.

Breakouts, when properly interpreted, are a reliable measure of the orientation of the maximum horizontal stress. Zoback and Zoback (1980), Gough and Bell (1981), Plumb and Cox (1987), Castillo and Zoback (1994), and others have successfully used breakouts to constrain the orientation of the stress field. However, other forms of wellbore elongation may be mistaken for breakouts. Key seats (mechanical erosion of the wellbore wall by the drill string) and washouts (erosion of material from entire well circumference by upward-moving drilling mud) may be mistaken for wellbore breakouts since they produce a similar type of hole ovality. Since all the stress data in the North Sea before this study were obtained using less reliable methods such as breakout analysis and inversion of earthquake focal-plane mechanisms, all of the data in the North Sea was considered unreliable. In many cases of borehole elongation observed in the Visund field, the direction of elongation coincides with, and follows the orientation of, the drilling direction (Figure 4). By plotting the orientation of the breakout along with the orientation of the hole, it becomes clear that the breakouts are following the direction in which the hole was drilled. This is an indication that the hole ovality was caused by pipe-wear on the wellbore wall, rather than because of compressive failure of the formations being drilled.

Chapters 2 and 4 show the results of constraining the orientation of the stress tensor using drilling-induced tensile fractures in four fields in the northern North Sea. Drilling-induced tensile fractures are extremely useful for determining the orientation of the stress field since an image of the wellbore wall provides the opportunity to interpret whether the feature is in fact a fracture, and it provides a more precise measure of the orientation of the maximum horizontal stress. Examples of this data can be seen in Appendix B.

By relying almost exclusively on drilling-induced tensile fractures seen in exploration wells drilled into four fields in the northern North Sea, the stress field becomes clear. Figure 5 shows the results of using tensile fractures to constrain the orientation of the maximum horizontal stress. The most obviously unreliable breakout and earthquake focal-plane

mechanism data were edited and the remaining data are plotted in this figure as well. Note how consistently oriented the stresses are, similar to stress orientations seen in other parts of the world. In some cases the stress tensor may not be oriented exactly vertically and horizontally, but varies slightly. This situation is addressed in Appendix C.

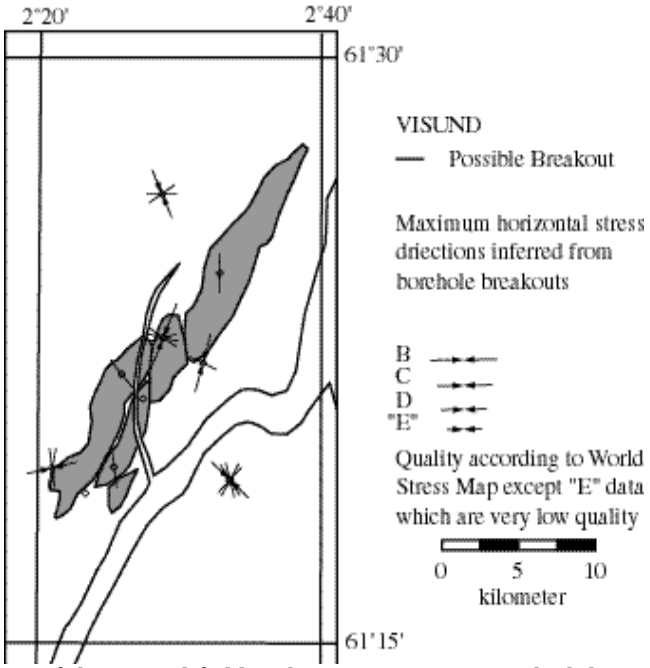

Figure 1.2: Map of the Visund field with stress orientations. Thick lines are the author's preferred interpretations. Thin lines are other possible directions of the maximum horizontal stress. Figure modified from Fejerskov (1996).

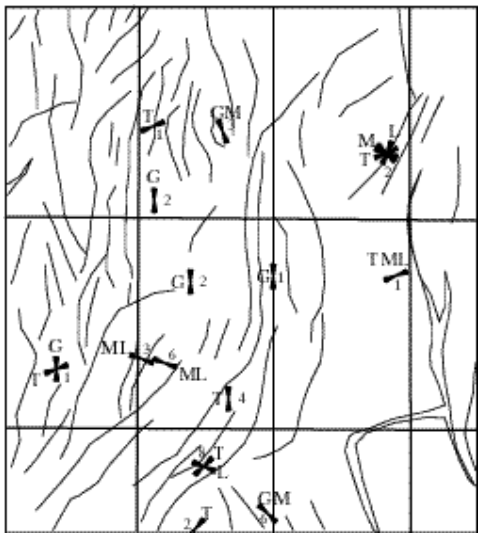

Figure 1.3: Map of stress orientations and the interpreted causes of the stress orientations in Field 3. T=Tectonic, G=Topographic, M=Major Fault, L=Local Fault.

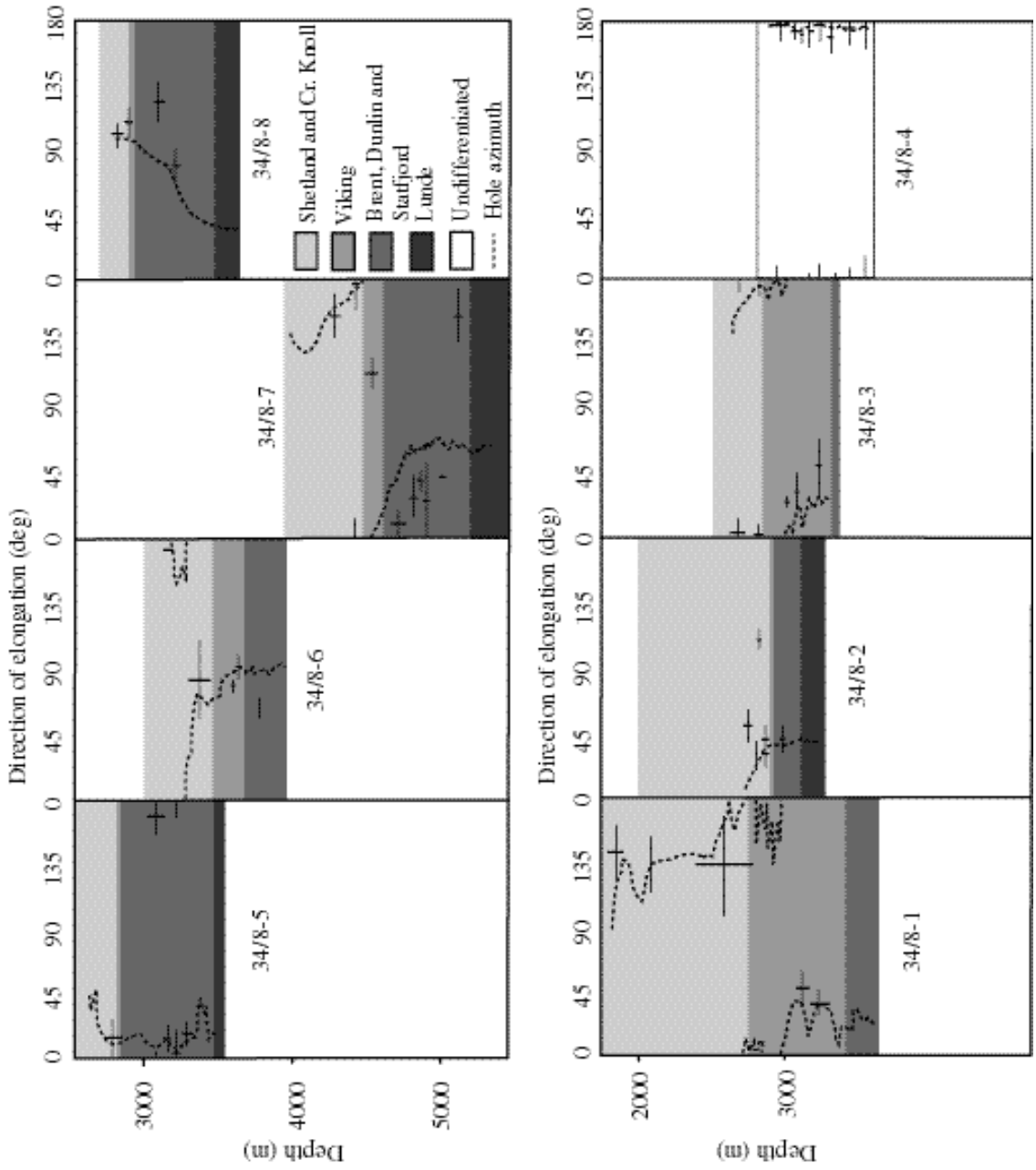

Figure 1.4: Direction of maximum horizontal stress derived from borehole breakout analysis in Visund. Plots show azimuth from 0˚ to 180˚ versus depth of both breakouts and wellbore drilling direction. In each well, short vertical bars indicate depth interval of interpreted breakout, whereas horizontal bars represent standard deviation from mean orientation of maximum horizontal stress. Hole azimuth is plotted as a continuous dashed line. In nearly every well breakouts follow drilling direction. Figure modified from Fejerskov (1996).

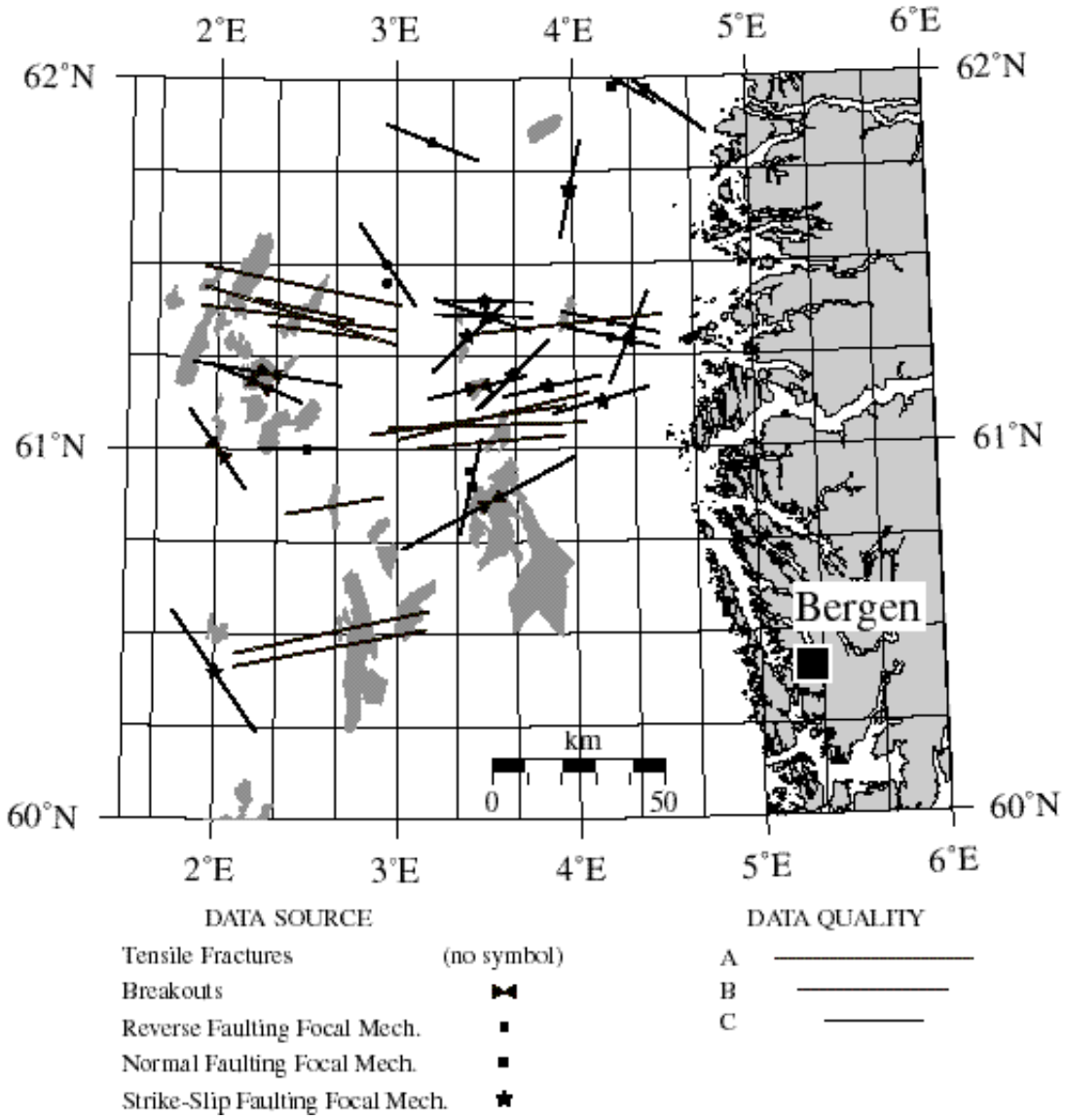

Figure 1.5: Reliable stress orientations in the northern North Sea. Note that the drilling-induced tensile fractures give a very consistent orientation of the maximum horizontal stress.

1.4 Constraining Stress Magnitudes

Previous studies of the in-situ stress along the Norwegian margin have tended to either focus strictly on the orientation of the stress tensor (e.g. Lindholm et al., 1995; Dart et al., 1995; Fejerskov et al., 1995), or the magnitude of only two of the principal stresses (e.g. Zhang et al., 1995). Those investigations that have attempted to model all three principal stresses (e.g. Jørgensen and Bratli, 1995) use highly questionable methodologies and have published relative magnitudes of the principal stresses ($S_v > S_H > S_h$) that are inconsistent

with the strike-slip to reverse faulting stress field seen from earthquake focal-plane mechanisms (Lindholm et al., 1995) (Figure 5). Having a well constrained stress tensor was critically important to every other aspect of this project. Without a well constrained stress tensor predictions about wellbore stability would not be possible, and calculations of resolved stresses on faults would be unreliable. The magnitude and orientation of all three principal stresses were determined following the integrated stress measurement strategy (ISMS) outlined by Zoback et al. (1993) and Brudy et al. (1997) (Figure 6). Using the program Stress and Failure of Inclined Boreholes (SFIB), developed by Peska and Zoback (1995, 1996), it was possible to constrain the magnitude of the maximum horizontal stress. Knowledge of the minimum horizontal stress, the vertical stress, and wellbore failures are used to constrain the range of possible magnitudes for the maximum horizontal stress. Chapters 2 and 4 show how the stress tensor was constrained in detail, and show that the maximum horizontal stress was larger than the vertical stress, and the minimum horizontal stress was nearly equal to the vertical stress in every field investigated. These findings are consistent with the strike-slip to reverse fault stress field seen from earthquake focal-plane mechanisms.

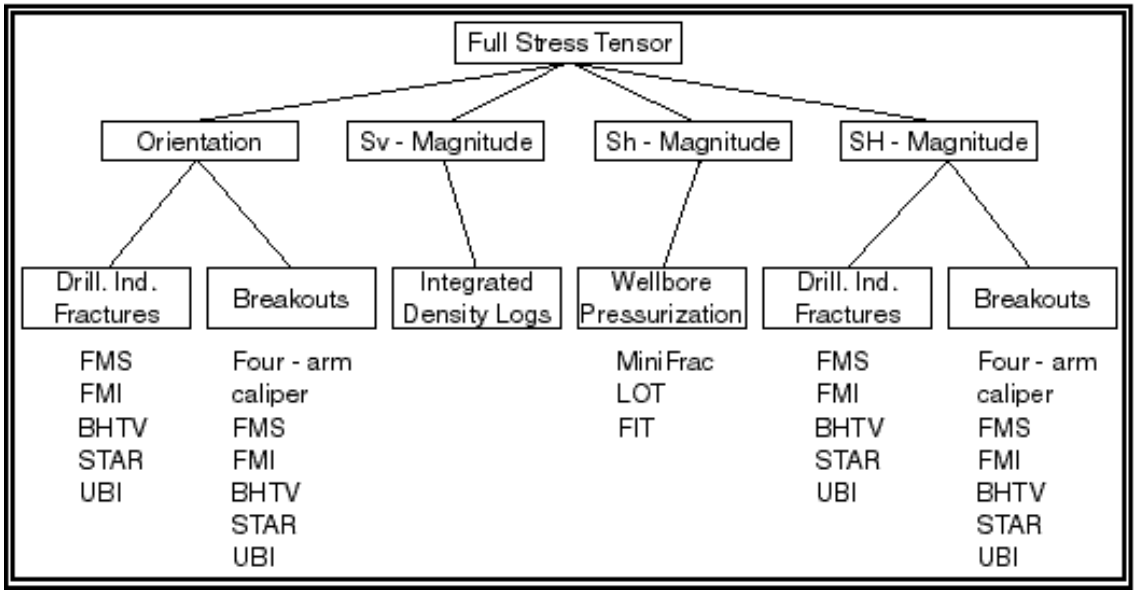

Figure 1.6: The Integrated Stress Measurement Strategy.

1.5 Application of In-Situ Stress to Wellbore Stability

Compressive wellbore failures, if not controlled, may cause drilling problems like hole collapse, stuck pipe, pack-off, and obstructions when running into the hole, as well as

problems while producing the reservoir such as sand production. Prevention of wellbore failure requires that the circumferential stresses around the wellbore be minimized. By utilizing SFIB, the in-situ stress, and rock strength data, a model of the borehole orientations and mudweights that will minimize the circumferential stresses during drilling and production can be created. Chapter 2 applies the stresses measured in Visund to well 10S in order to determine what mud weight should have been used while drilling the well. The analysis and results shown in Chapter 2 match precisely with the mud weight used in the wellbore. Well 10S was the most successful well in the Visund field in terms of minimizing lost time during drilling.

1.6 Application of In-Situ Stress to Hydrocarbon Leakage and Migration

How faults affect the migraton of fluid in petroleum reservoirs is difficult to determine. Faults are known to act as both barriers and conduits to fluid flow through formations. Some faults contribute dramatically to formation permeability (Finkbeiner et al., 1998), yet others provide effective barriers separating distinct reservoir compartments (Hunt, 1990). A number of mechanisms have been proposed to explain hydrocarbon migration along faults and fractures.

Hydrocarbon bearing formations experiencing high overpressure may leak cyclically as a result of hydrofracture as the pore pressure approaches the least principal stress (Nur and Walder, 1990), or as the pore pressure causes faults which are optimally oriented for shear failure to slip (Sibson, 1992). Stresses acting normal to fracture and fault planes have been shown to decrease fracture permeability in both laboratory studies (Trimmer et al., 1980; Tsang and Witherspoon, 1981) and theoretical models (Ayatollahi et al., 1983), and likely contribute to the sealing capacity of faults and fractures in sedimentary basins. In some cases the in-situ stress and pore pressure may not be sufficient to cause faults to reactivate because of the reservoir geometry. Pore pressures in the reservoir may never reach the critical pore pressure for triggering hydrofracture or frictional slip on preexisting faults because the reservoir is not completely charged, pinches out, or leaks through a spill point (Figure 7). Furthermore, if the rate of diffusion or leakage of hydrocarbons through the caprock is the same as the rate at which hydrocarbons enter the reservoir, then the pore pressure will never rise enough to reactivate faults and fractures.

Hermanrud et. al (1997) deduce from seismic chimneys and hydrocarbon shows in caprocks that most overpressured hydrocarbon bearing structures in the northern North Sea

are currently leaking. In contrast, they note that all overpressured structures in the Haltenbanken (to the north) are empty, even though residual oil shows suggest they were once charged. They speculate that the difference between the Haltenbanken and the rest of the North Sea may be the result of different stress histories. Gaarenstroom et al. (1995), and Borgerud and Svare (1995), have noted a relationship between charged and uncharged reservoirs and minimum effective stress (Figure 8). In the Central North Sea Graben, wells are typically dry below a minimum effective stress of approximately 1000 psi (6.9 MPa); and in the Halten Terrace the wells are dry below approximately 3000 psi (20.7 MPa). Gaarenstroom et al., and Borgerud and Svare, have also observed that dry wells typically once contained hydrocarbons. These results imply a strong relationship exists between the in-situ stress and hydrocarbon migration in the North Sea.

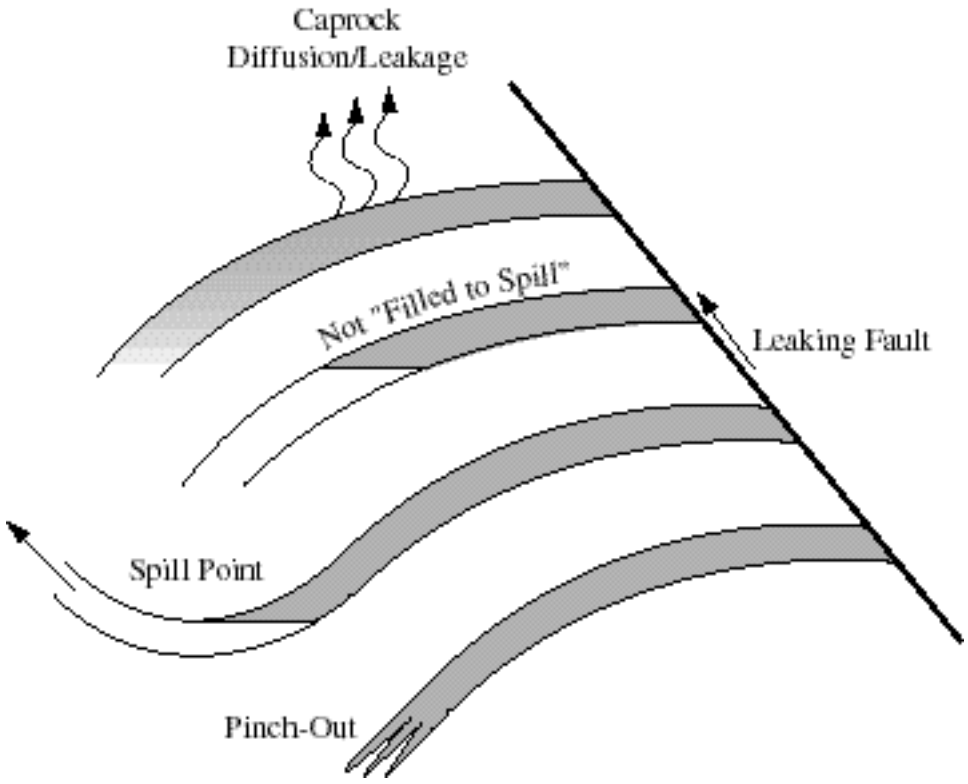

Figure 1.7: Mechanisms which may limit hydrocarbon column heights.

Sibson (1990) speculated that rising shear stress as a result of tectonic loading, coupled with increasing pore pressure will cause faults to slip and leak periodically. Increased permeability as a result of dilatancy allows fluids to escape, and the fault eventually seals as a result of hydrothermal precipitation. Barton et al. (1995) showed that faults with high ratios of shear to normal stress (i.e. above the 0.6 bound determined by Byerlee, 1978) tend

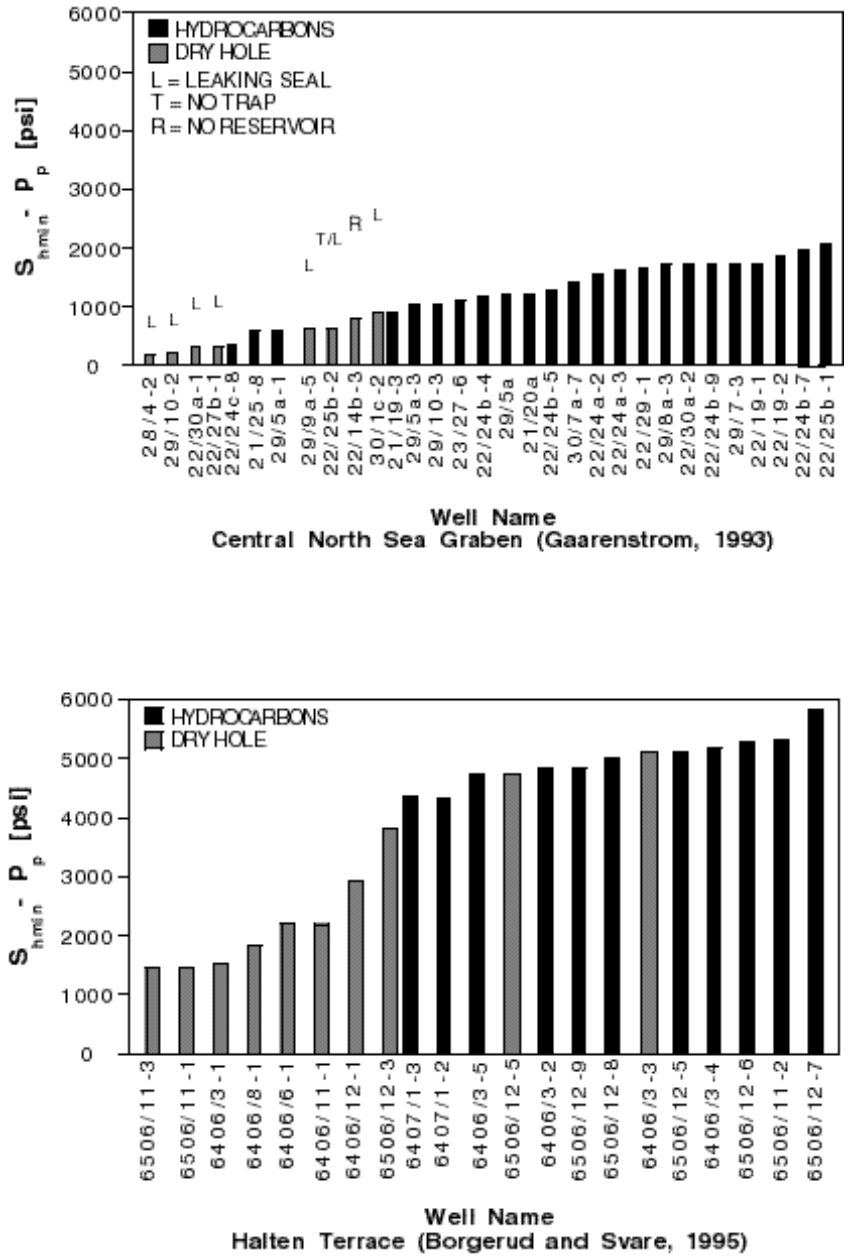

Figure 1.8: Effective minimum horizontal stress vs. hydrocarbon bearing and dry holes.

to conduct fluids, while those with low ratios of shear to normal stress tend to be sealing and non-hydraulically conductive. The study cases of Barton et al., however, have all been done in crystalline rock in actively deforming regions. In Chapters 3 and 5 we explore the relationship between the in-situ stress and hydrocarbon leakage along reactivated faults in the northern North Sea. We show that even in a relatively static or slowly deforming sedimentary basin such as exists in the North Sea, the stress and pore pressure measurements and observations of leakage are consistent with the leakage mechanism

proposed by Barton et al. and Sibson. We also show in Chapters 3 and 5 that the pore pressure never exceeds the critical pore pressure predicted by Coulomb frictional failure. If this is the case in sedimentary basins throughout the earth, then hydrofacturing will never take place unless all of the faults bounding the reservoir are all highly mis-oriented for frictional slip in the current stress field.

Capillary entry pressure, clay smear and fault gouge are other mechanisms which some investigators have proposed to determine the sealing and leaking potential of faults. The capillary entry pressure is the surface tension that hydrocarbons must overcome in order to move through a pore throat. It is unlikely this mechanism is responsible for controlling hydrocarbon leakage in the fields studied because the pore pressures consistently rise only as high as the predicted critical pore pressure. If the predicted capillary entry pressure were lower than the critical pore pressure, then an explanation would be needed for those pore pressures that exceed the capillary entry pressure. If the predicted capillary entry pressure were higher than the critical pore pressure then the mechanism would be meaningless, as the hydrocarbons will leak along the path of least resistance. Leakage would take place along the reactivated fault plane before the pore pressure became high enough to exceed the capillary entry pressure. Clay smear is the most popular explanation for the varying sealing potential of reservoir bounding faults. Clay smear results from the smear of weak clays from the bed rock into the fault plane. An especially soft formation cut by a fault with a large offset is expected to produce a very good seal. However, regardless of fault slip magnitudes and clay smear potential, we show in chapters 3 and 5 that faults that are critically stressed in the northern North Sea tend to be conducting fluids, and those that are not critically stressed tend to be sealing.

CHAPTER 2

CONSTRAINING THE STRESS TENSOR IN THE VISUND FIELD, NORWEGIAN NORTH SEA: APPLICATION TO WELLBORE STABILITY AND SAND PRODUCTION

A slightly shorter version of this chapter was published with Mark D. Zoback as co-author in International Journal of Rock Mechanics and Mining Sciences, v. 37, (2000), pp. 317-336.

2.1 Abstract

In this study we examine drilling-induced tensile wellbore failures in five exploration wells in the Visund oil field in the northern North Sea. We use observations of drilling-induced wellbore failures as well as density, pore pressure, and leak-off test measurements to estimate the magnitudes and orientations of all three principal stresses. Each well yields a very consistent azimuth of the maximum horizontal stress (100˚ ± 10˚), both with depth and laterally across the field. Stress orientations are constrained at depths as shallow as 2500 meters and as deep as 5300 meters in these wells. We show that the magnitudes of the three principal stresses (S_v, S_{hmin}, and S_{Hmax}) are also consistent with depth and reflect a strike-slip to reverse faulting stress regime. The magnitude of the maximum horizontal stress is shown to be significantly higher than the vertical and minimum horizontal stresses (e.g. S_v = 55 MPa, S_{hmin} = 53 MPa, and S_{Hmax} = 71.5 MPa at 2.8 km depth). Data from earthquake focal plane mechanisms (Lindholm et al., 1995) show similar stress orientations and relative magnitudes and thus indicate a stress field that is relatively consistent throughout the thickness of the brittle crust. We illustrate how knowledge of the full stress tensor allows one to place bounds on in-situ rock strength and determine optimally stable trajectories for wellbore stability and sand production during drilling, after the completion of drilling, and as pore pressure is reduced during oil and gas production.

2.2 Introduction

Determination of the full stress tensor in oil fields is critical for addressing engineering problems of wellbore stability and sand production as well as geologic problems such as understanding dynamic constraints on hydrocarbon migration and fracture permeability. Controlling wellbore instabilities requires understanding of the interaction between the rock strength and in-situ stress. Because in-situ stress and rock strength cannot be altered or controlled, the only way to inhibit wellbore failure during drilling is to adjust engineering practice by choosing optimal trajectories and mud weights. Similarly, utilization of an appropriate trajectory can limit sand production by reducing the tendency for failure around a wellbore.

This paper presents an analysis of stress and wellbore stability in the Visund field, which is located in the Norwegian North Sea to the northwest of Bergen, near the western edge of the Viking Graben (Figure 1). The Visund field sits within the approximately 25 km long, 2.5 km wide Visund fault-block, which is the most easterly major fault block on the Tampen Spur (Færseth, 1995). The state of stress in the Norwegian North Sea is

generally characterized by an east-west to northwest-southeast compression, but exhibits appreciable scatter in places (e.g., Müller et al., 1992; Lindholm et al., 1995).

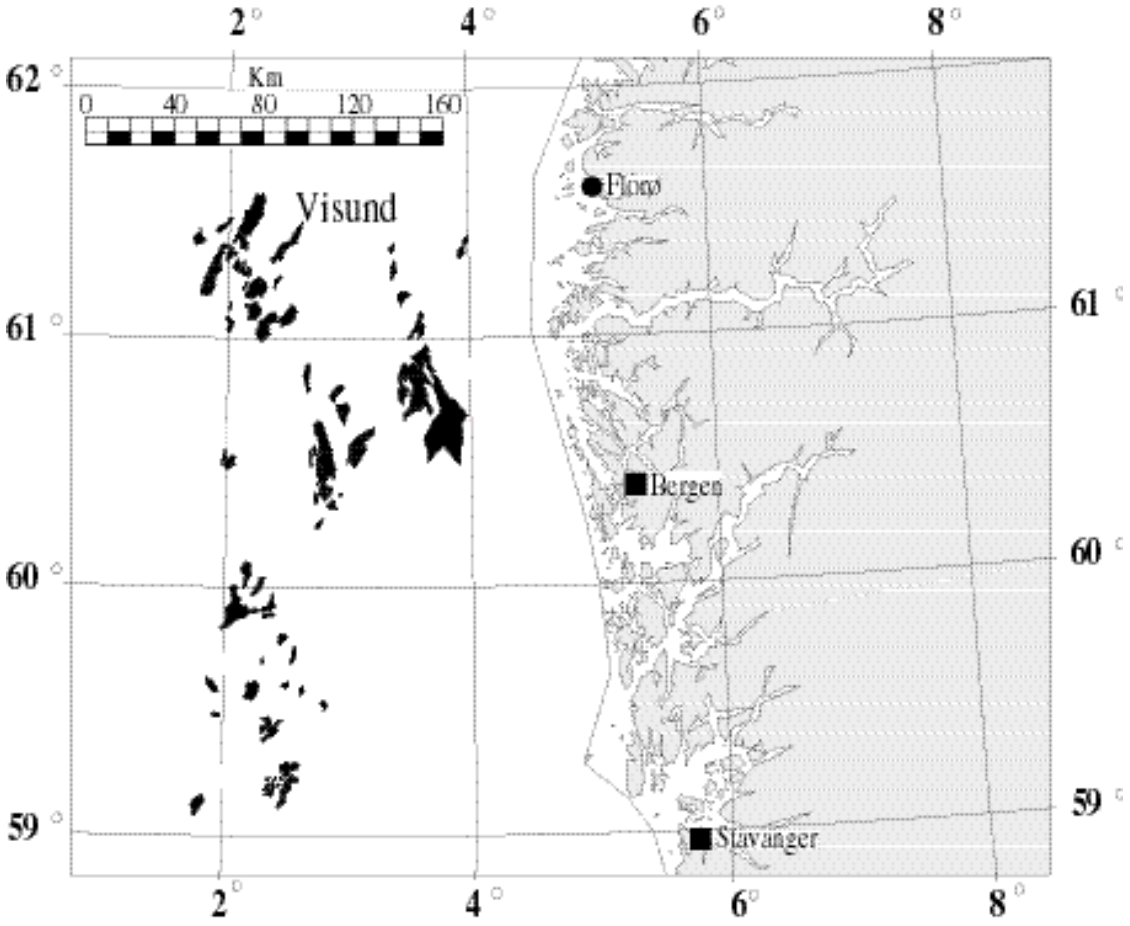

Figure 2.1: Map of the northern North Sea modified from the Norwegian Petroleum Directorate, 1997. The Visund field sits on the western edge of the Viking Graben to the northwest of Bergen, Norway.

In the following sections we describe how observations of drilling-induced compressive failures (e.g., Gough and Bell, 1981; Zoback et al., 1985; Plumb and Hickman, 1985) and wellbore tensile failures (e.g. Aadnoy, 1990; Moos and Zoback, 1990; Brudy and Zoback, 1993; Brudy and Zoback, 1999) can be integrated with other routinely available wellbore information to constrain the full stress tensor. Our approach follows an integrated stress measurement strategy (ISMS), outlined by Zoback et al. (1993), and Brudy et al. (1997), to constrain the magnitudes and orientations of all three principal stresses. Using our estimates of in-situ stress we place bounds on the effective rock

strength. This information is then used to determine optimally-stable trajectories for drilling and minimizing sand production.

2.3 Observations of Wellbore Failure

Examination of Formation MicroScanner/Formation MicroImager (FMS/FMI) logs (Ekstrom et al., 1986) provided by Norsk Hydro, and run in seven wells, revealed extensive drilling-induced tensile failures in five of the wells. Examples of this data can be seen in Appendix B. We plot the azimuth of the tensile fractures as a function of depth in Figure 2. In each case, black data points represent tensile fractures that are aligned with the axis of the wellbore, and data points representing tensile fractures that are inclined with respect to the axis of the wellbore are shown in gray. Error bars for near-axial tensile failures show the variation in azimuth of each fracture; while error bars for inclined tensile failures show the portion of the wellbore circumference spanned by each fracture. Near the center of each plot, bit trips and "wash and ream" operations are shown by horizontal and vertical lines respectively. A bit trip is plotted each time the drill string is run into the hole. This operation may cause a significant rise in the mud pressure at the bottom of the hole due to a piston effect. Washing and reaming the hole involves scraping the hole clean, and may remove evidence of drilling-induced tensile fractures. There is no visible correlation between the occurrence (or absence) of tensile fractures and these special drilling operations, suggesting that the tensile fractures formed (or did not form) during normal drilling operations, rather than as a result of extreme conditions in the well such as tripping the bit or reaming the hole.

All wells except 10S were drilled nearly vertically to total depth. Near-axial tensile fractures in wells 6, 7, 8, and 11, as well as in the vertical portion of 10S, suggest that the vertical and two horizontal stresses are principal stresses in this field (Brudy and Zoback, 1993). Inclined tensile fractures observed in four of the wells (most prevalent in the 10S well) indicate possible exceptions to this and are discussed in Appendix C.

In order to determine the orientation of the stress field in this region, we focus on the orientation of the tensile fractures aligned with the wellbore axis. We use a circular statistical method developed by Mardia (1972) to obtain the mean azimuth and standard deviation of the maximum horizontal stress for each well (insets of Figure 3). The uncertainty in the azimuth represents two standard deviations from the mean. The frequency is calculated by adding the tensile fractures in 0.2 meter intervals.

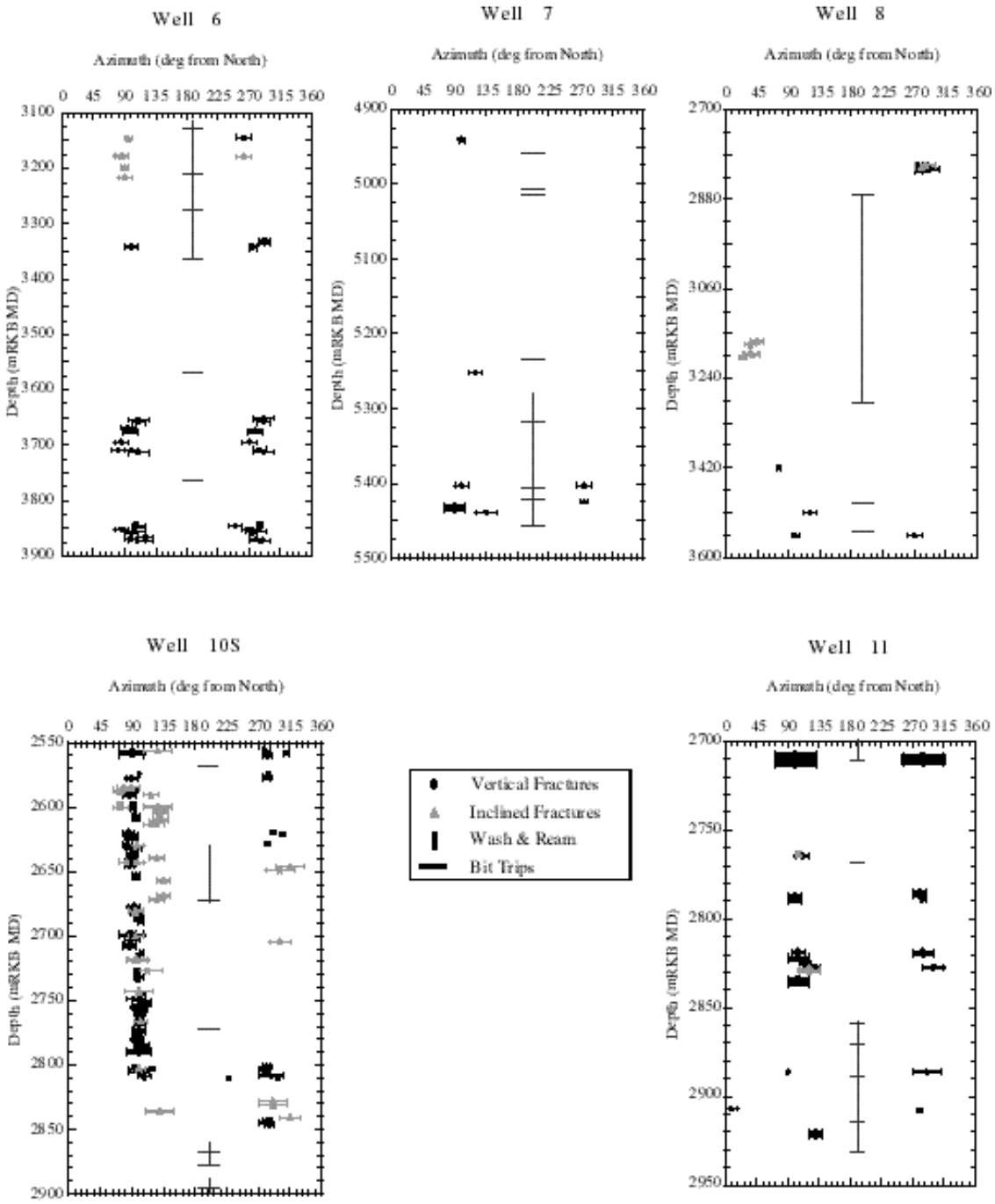

Figure 2.2: Azimuth of drilling induced tensile fractures observed in image logs as a function of depth.

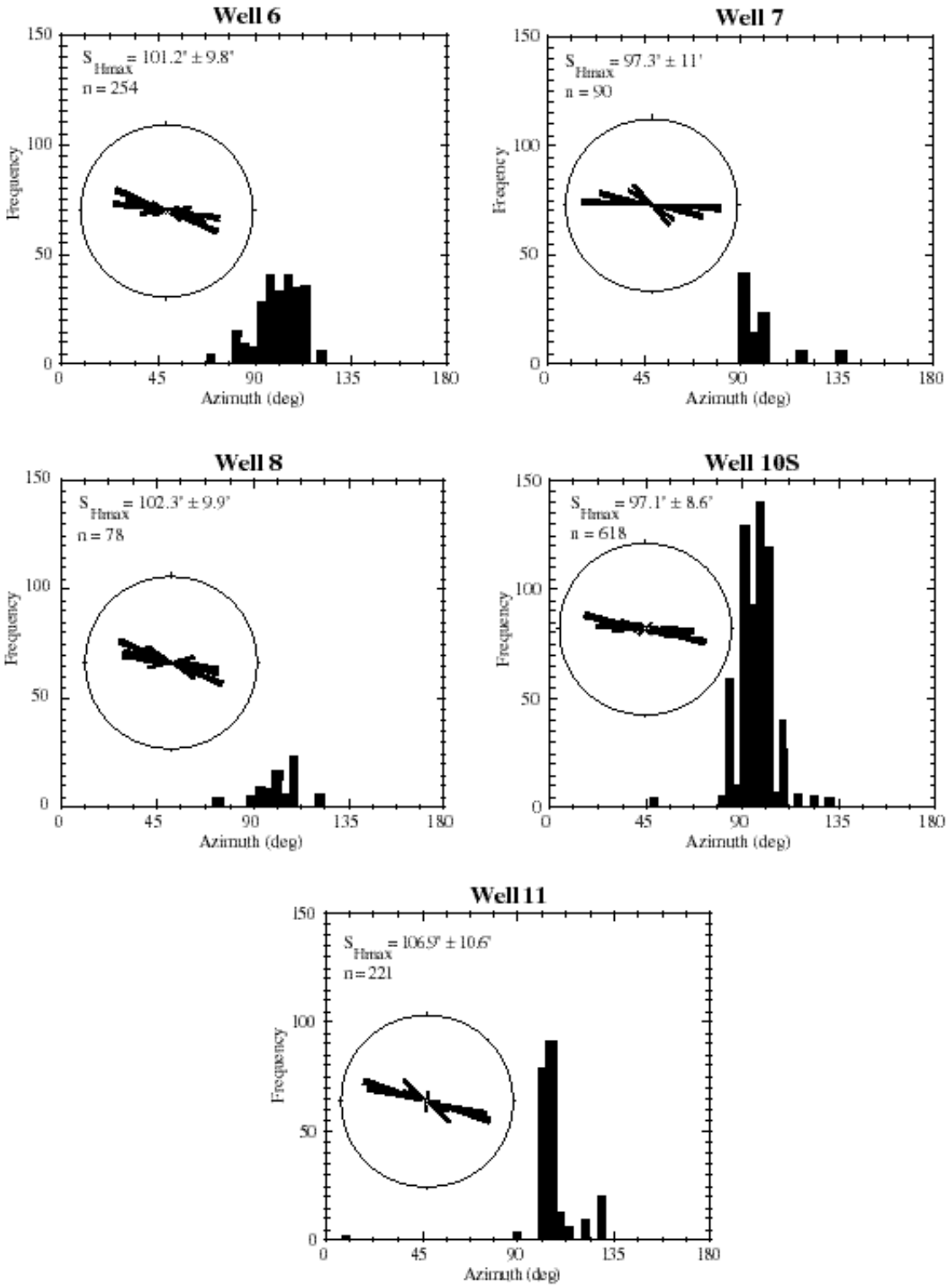

Figure 2.3: Histograms and rose diagrams showing the orientation of the maximum horizontal stress. Each rose plot is normalized by the number of data points, and therefore the length of the bars does not reflect the relative frequency of the tensile fractures between wells. Number of 0.2 meter observations (n) is shown in each case.

An anomalous stress orientation seen from a wellbore breakout [reported by Fejerskov (1996) and later analyzed in this study] and inclined tensile fractures was detected over an approximately 135 meter interval of well 8. This stress orientation was not seen in any of the other wells to the north or south, and appears to be the result of a localized stress anomaly due to slip on a preexisting fault penetrated by this well. The sub-seismic fault responsible for this anomaly can be inferred from the geologic section by noting a repeated sequence of the Brent reservoir sands. The relationship between anomalous stress fields and slip on faults has been noted by other authors (e.g. Shamir and Zoback, 1992; Barton and Zoback, 1994; Paillet and Kim, 1997). We therefore assume that this single anomaly is not representative of the tectonic stress field.

Figure 4 summarizes our findings concerning the orientation of the maximum horizontal stress. The mean orientation of SHmax for each well is plotted in map view and clearly shows a consistently oriented stress field. The rose diagram shows the orientations of all of the tensile fractures from all of the wells. The plot in the lower right shows the depths over which the orientation of SHmax is constrained in each well. Gray shaded regions show portions of each well that were not logged. This plot shows that the maximum horizontal stress is constrained to depths as shallow as 2550 meters and as deep as 5250 meters (RKB TVD). The orientation of the maximum horizontal stress as determined from earthquake focal plane mechanisms (Lindholm et al., 1995) is similar to our findings (azimuths between 90˚ and 120˚). Our data, coupled with these findings, indicate that the orientation of the maximum horizontal stress is consistent across the Visund field as well as throughout the thickness of the brittle crust.

The scatter in stress directions observed in some parts of the northern North Sea (determined from wellbore elongations) has led some investigators to conclude that shallow stress directions are decoupled from the deeper regional stress field (e.g. Borgerud and Svare, 1995). We have shown that close examination of reliable data reveals a consistently oriented stress field, and we further demonstrate in Appendix C that we can use this stress field to explain the occurrence of inclined drilling-induced tensile fractures.

2.4 In-Situ Stress and Rock Strength

We utilize the interactive software package, Stress and Failure of Inclined Boreholes (SFIB), developed by Peska and Zoback (1995), to constrain the maximum horizontal stress magnitudes and to put limits on rock strength. Estimation of the maximum horizontal stress requires prior knowledge of the vertical stress, the minimum horizontal stress, the pore pressure, the mud weight, and the change in temperature at the wellbore wall during

drilling. Final well reports provided by Norsk Hydro contain this information. We analyze each well individually so that estimates of the maximum horizontal stress are not affected by data from wells in different pore pressure compartments or with slightly differing overburden stresses. The vertical stress, S_v, used in this study was derived from integrated density logs. Because these logs are seldom run up to the sea floor, the density must be estimated in the shallow subsurface. The resulting errors in the overburden gradient are negligible in wells 10S and 11 since only a small amount (approximately 50 meters) of sediment is not accounted for by the density logs. In wells 6, 7, and 8, the density logs were only run in the deeper portions (below approximately 2500 meters) of the holes. The densities used in the upper portions of these holes are estimated from shallow measurements in nearby holes. Overburden gradients from wells 6, 7, and 8 nevertheless provide overburden stresses which are similar to those found in wells 10S and 11. We derive the minimum horizontal stress, S_{hmin}, from Leak-off Tests (LOT) and Formation Integrity Tests (FIT) conducted in each well (see Gaarenstroom et al., 1993). In all of the wells the depth at which we wish to constrain the maximum horizontal stress is below the deepest LOT or FIT. We therefore assume a linear stress gradient between LOTs in each well and extrapolate this trend to the depth of investigation. The pore pressure, P_p, was obtained from Repeat Formation Tests (RFT). In order to use a reliable pore pressure value the stress analysis in each well was conducted as close as possible to an RFT depth. Pore pressure data was not available for well 7. Consequently, we do not constrain the maximum horizontal stress in this well. We derive a mud weight value, P_m, from the maximum equivalent circulating density (ECD), which takes into account frictional effects between the wellbore wall and the mud as well as the mud density. We use a static mud weight in well 6 because an ECD value was unavailable. Use of the highest mud density value is required since it is impossible to determine the precise mud weight at which the tensile cracks initiated. Although the tensile fractures may have formed at mud pressures lower than the ones we use, our utilization of the highest mud pressure allows us to calculate a reasonable lower bound for the maximum horizontal stress. An upper bound for the maximum horizontal stress is derived from our analysis of rock strength and compressive failures in these wells. The amount of cooling at the wellbore wall was derived from temperature gradient plots. Each well showed cooling between 20˚ and 30˚C at the depths of investigation. While the temperature change of the wellbore wall was considered in these calculations, it had little effect on the estimation of S_{Hmax}. We examine thermoporoelastic effects on the stress in more detail in Appendix D.

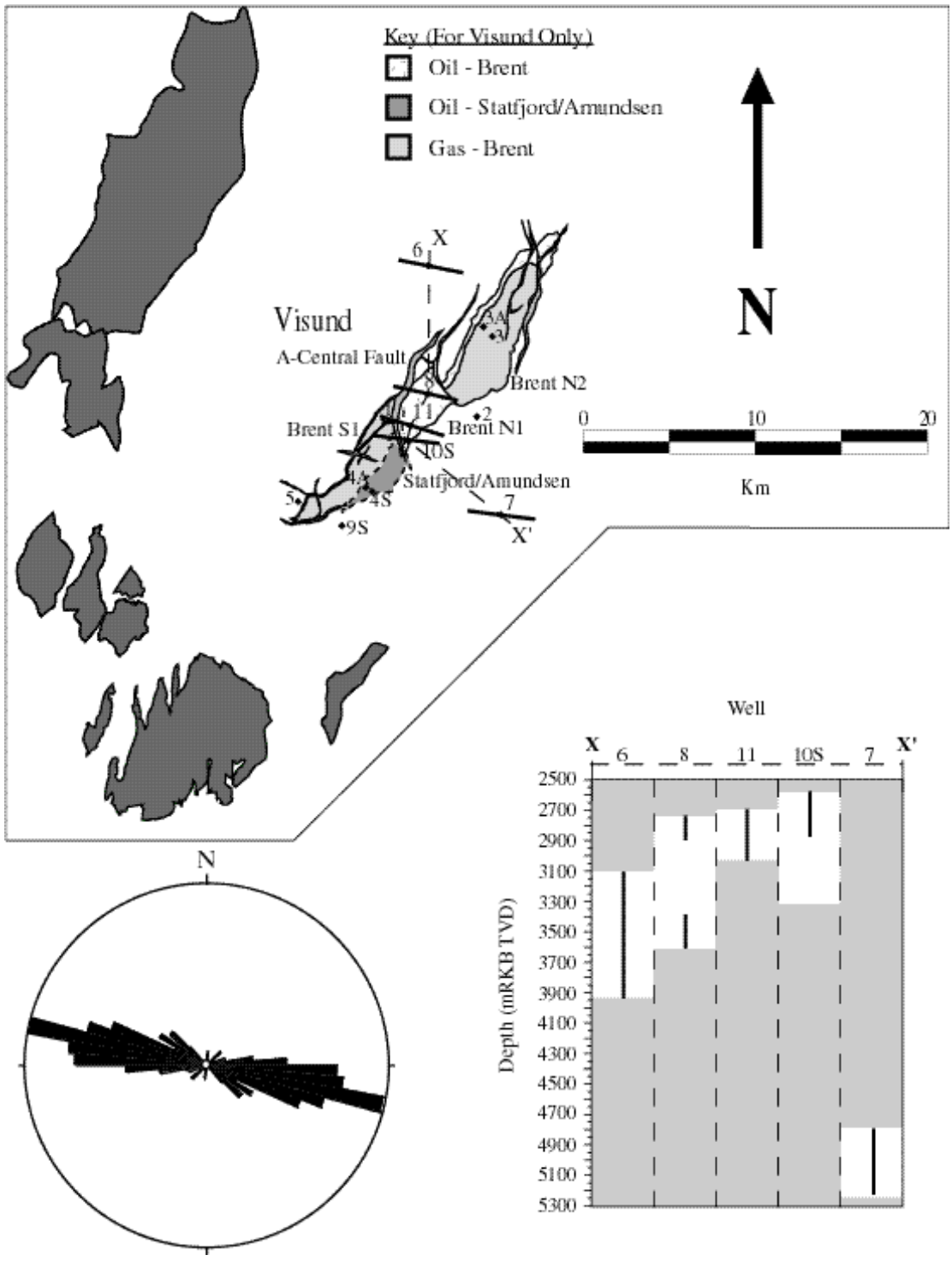

Figure 2.4: Map view of S_{Hmax} orientations (modified from Norwegian Petroleum Directorate and Norsk Hydro maps), rose plot with all orientation data, and plot showing depths over which SHmax is constrained in each well. Gray regions show portions of wells that were not logged. Orientation of the maximum horizontal stress is consistent both laterally and with depth in this field.

Figure 5 shows how we constrain the maximum horizontal stress, S_{Hmax}. The plot represents the allowable stress state at a given depth constrained by 1) Mohr-Coulomb frictional faulting theory for the crust assuming a coefficient of sliding friction of 0.6 (Byerlee, 1978) (four sided polygon), and 2) compressive and tensile wellbore wall failures (thick short dashes and long dashes respectively) (see Moos and Zoback, 1990, for an explanation). Stress magnitudes that fall above the short dashed tensile failure contour (assumed to be zero in this study) indicate stress states consistent with the occurrence of drilling-induced tensile fractures, while values that fall below indicate no tensile failures should occur. Similarly, for a given rock strength, stress magnitudes that fall above one of the long dashed compressive failure contours indicate breakouts should occur, while those that fall below indicate no breakouts should be observed. We constrain the maximum horizontal stress only where tensile fractures were observed in each of these wells, meaning the stress state must be such that it falls above the short dashed tensile failure line in our figures. No breakouts were observed in any of the wells at the depths where we constrain the maximum horizontal stress. This observation is utilized below to place a lower bound on the in-situ rock strength. While coefficients of sliding friction may be as high as 1.0 in some rocks, faults in sediments tend to have lower coefficients of friction. We consider a coefficient of friction of 0.6 to be an upper bound in this case, as the sediments are poorly cemented and consolidated.

2.4.1 Constraining S_{Hmax} In Wells 10S and 11

Wiprut et al. (1997) presented a stress analysis of well 10S using near-axial tensile fractures. The points of departure of this study from the previous study are three-fold: (1) we constrain the maximum horizontal stress in multiple wellbores; (2) we perform a more comprehensive analysis of in-situ rock strength; (3) we analyze inclined tensile fractures observed in well 10S.

Well 10S presents the best opportunity to reliably constrain the magnitude of the maximum horizontal stress. As the well increases in deviation and begins to encounter a different stress field a transition from a stress state in which tensile fractures form, to one in which they do not, occurs. Figure 6 shows that tensile fractures form continuously in this well to a deviation of approximately 35˚, and then abruptly stop. Because tensile failures are present at the depth of investigation, and the tensile cracks stop just below 2830 mTVD (as shown in Figure 6), we expect the value of S_{Hmax} at 2830m to be approximately equal to the value indicated by the short dashed contour line (71.5 ± 4.5 MPa) (Figure 7). The steep slope of the short dashed tensile failure lines in Figure 7 means a small uncertainty in

the minimum horizontal stress creates a large uncertainty in the maximum horizontal stress. We illustrate in Appendix C that the occurrence of inclined tensile fractures is easily explained by this stress tensor, using only minor (±10˚) perturbations to the mean orientation of the stress tensor and slight increases in the mud pressure.

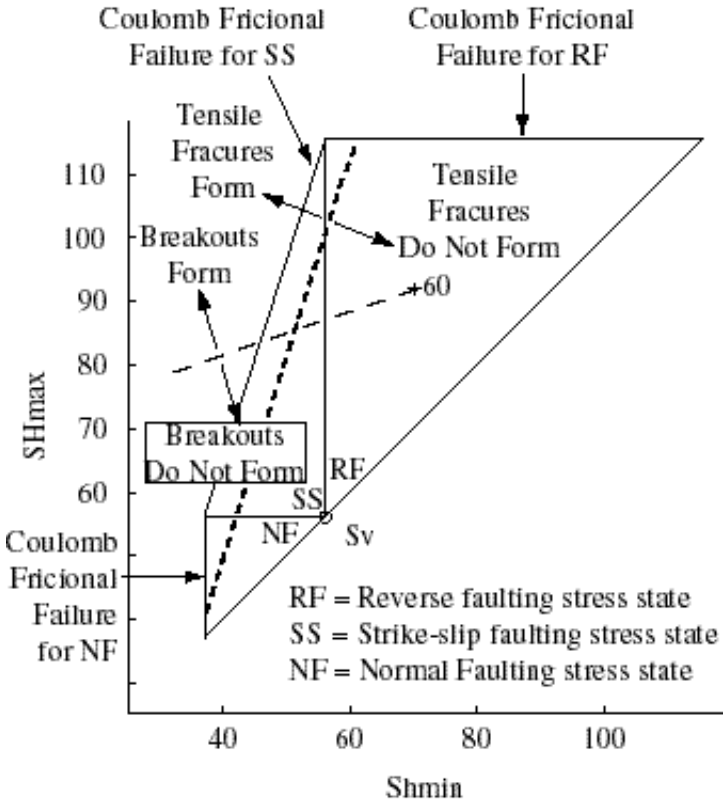

Figure 2.5: Theoretical stress polygon plotted with minimum horizontal stress as a function of maximum horizontal stress. The vertical stress (S_v) plots as a point since the model is run at a specific depth. The polygon is defined by Coulomb frictional failure theory, assuming a coefficient of sliding friction of 0.6. If the stress is such that it plots outside the polygon, then faults which are optimally oriented for frictional failure are expected to begin slipping until the stress plots inside the polygon. Stress is constrained by the polygon and observations of wellbore failure. Stresses that plot above a tensile failure or breakout line imply that mode of failure should be observed. Stresses that plot below one of the failure lines imply that mode of failure should not be observed.

Each compressive failure contour in Figure 7 represents a different uniaxial compressive rock strength (UCS) value, as shown, assuming that a breakout width of at least 40˚ would be required in order to be detected by the wide pads of the FMI tool. Well 10S is the only well in which knowledge of the rock strength is not needed to constrain S_{Hmax} because the stress is constrained by the tensile failure contour. Since no breakouts were detected in this well, the stress values determined above imply the apparent UCS of the rock (assuming a coefficient of internal friction of about 1.0) is greater than 18 MPa.

Laboratory strength measurements conducted by Norsk Hydro on cores taken throughout the region give an average value for the uniaxial compressive rock strength of approximately 25 MPa in the caprocks at this depth. The rock strength may also be constrained by the breakout width if breakouts occur, as weak rock will have wider breakouts than strong rock (Zoback et al., 1985).

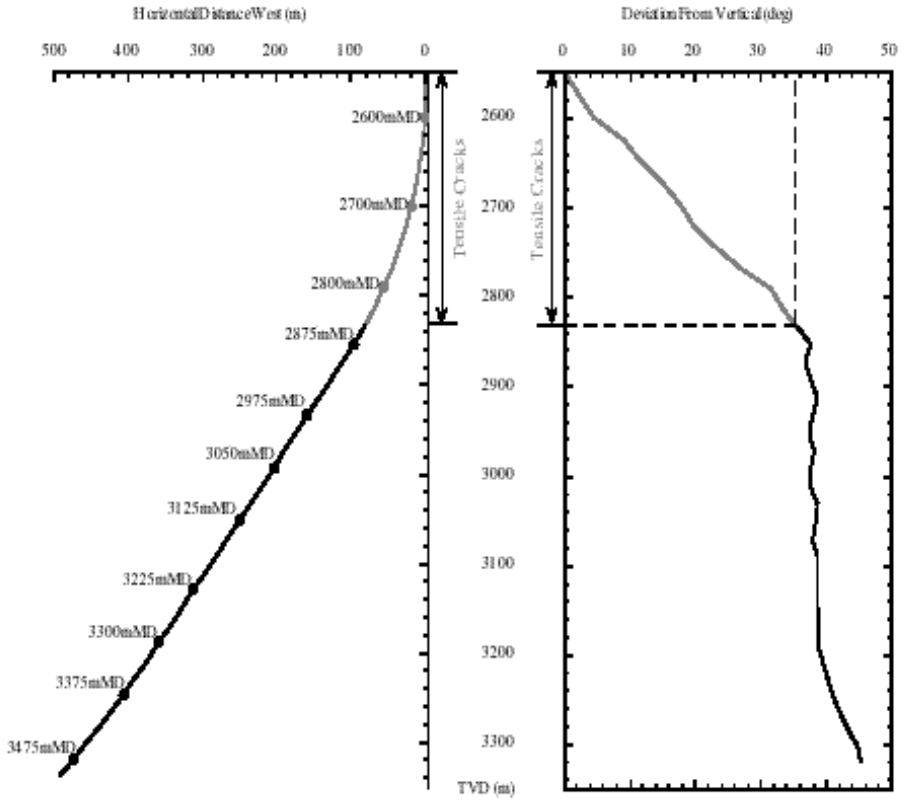

Figure 2.6: Section view of the drilling direction (left) and wellbore deviation as a function of depth (right). Measured depths are plotted along the wellbore path. Tensile fractures were detected from 2550 to 2850 meters measured depth (2550 to 2830 meters true vertical depth). The tensile fractures stopped at a deviation of 35˚ at 2830 mTVD.

In well 11 we use a reasonable upper bound on uniaxial compressive rock strength derived from laboratory tests on core, the upper bound of the minimum horizontal stress, and the lack of breakouts at this depth, in order to constrain the upper bound for the maximum horizontal stress. Since the upper bound on the rock strength determined from the Norsk Hydro laboratory tests on core is approximately 35 MPa at this depth, and in this formation, the maximum horizontal stress must fall below the 35 MPa breakout line. We use the lower bound of S_{hmin}, with the tensile failure contour, to constrain the lower bound of S_{Hmax}. The mean value from this range is our assumed value of S_{Hmax}, and the range is the uncertainty (70 ± 6 MPa) (Figure 7).

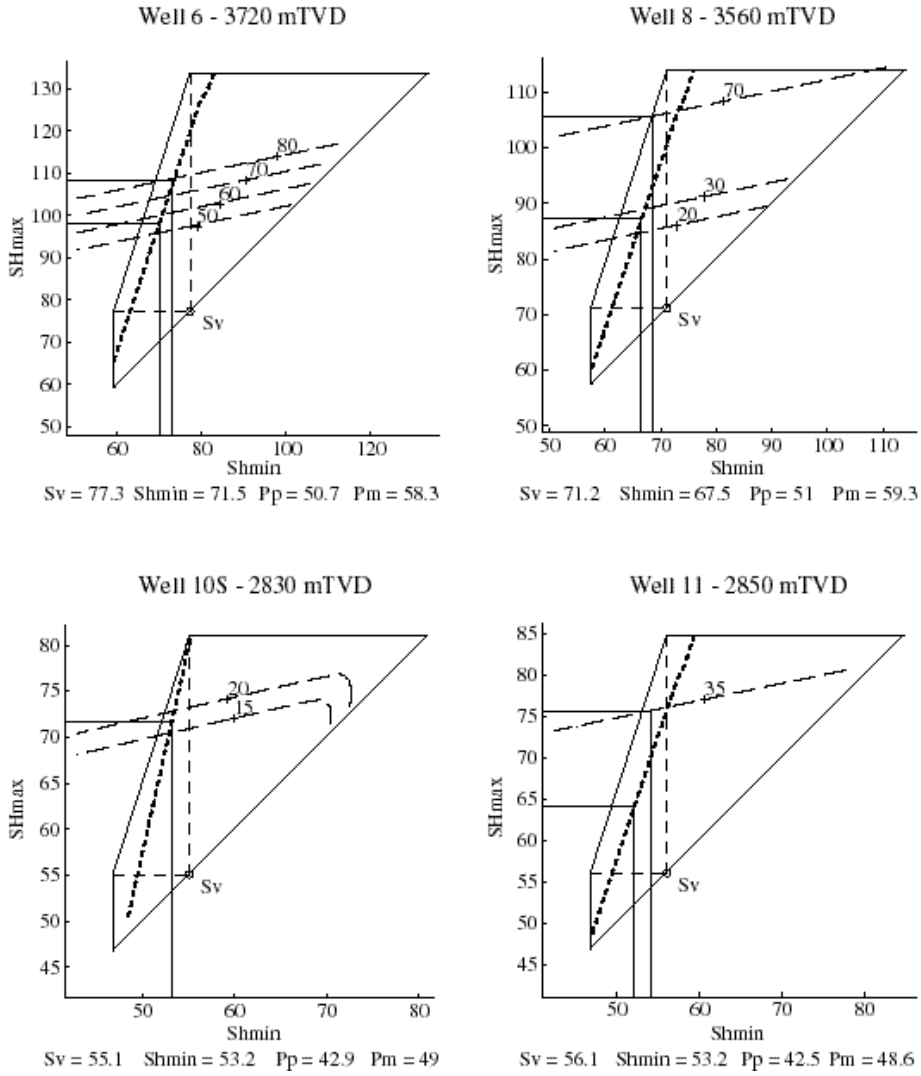

Figure 2.7: Stress polygons showing the constrained values of the maximum horizontal stress in each of the wells. Each analysis is developed for a specific depth shown above the figure. The relevant stress inputs (in MPa) are shown below the figures. Tensile failure contours are thick short dashes, and breakout contours are long dashes. Each breakout line represents a different rock strength value, as shown, assuming that a breakout width of at least 40˚ would be required in order to be detected by the wide pads of the FMI tool.

2.4.2 Constraining S_{Hmax} In Wells 6 and 8

In well 6, the least principal stress at the depth of interest is 71.5 ± 1.5 MPa. To account for the existence of drilling-induced tensile fractures, this requires lower bound values of S_{Hmax} to be 103.5 ± 5.5 MPa (Figure 7). As there are no breakouts observed in this well, these values imply UCS values that exceed 50 - 80MPa. While laboratory UCS tests done on the Etive sands (which occur only 5 meters below the depth at which the stress analysis

is done in well 6) indicate maximum strengths of only 30 MPa, the sandstone at the depth analyzed is more well cemented with silica than is the Etive. A theoretical estimate of strength in clean arenites provides a potential strength of 90 MPa for an average porosity of 15% (Vernik et al., 1993). Although the sandstone in question is not clean, it is reasonable to assume that the UCS is 50-80 MPa. We assume that the lower bound value of S_{Hmax} (103.5 ± 5.5 MPa) is approximately correct because if the value were even slightly higher (as permitted by Coulomb faulting theory, Figure 7), the corresponding rock strengths would be unreasonably high.

In well 8 the upper bound of the maximum horizontal stress is constrained using the upper bound of S_{hmin} and Coulomb faulting theory. Since no breakouts were observed in this well at 3560 mTVD, the upper bound values of S_{hmin} and S_{Hmax} predict that the rock strength is greater than 70 MPa. In this well we use the lower bound of S_{Hmax} as our assumed value of the maximum horizontal stress, and the upper bound as the extent of our uncertainty since both the rock strength and the friction coefficient may be either higher or lower than shown in the figure. The maximum horizontal stress in well 8 is constrained to be 105 MPa ≥ S_{Hmax} ≥ 87 MPa (Figure 7) although the upper bound is only limited by the assumed frictional strength of the crust.

Figure 8 shows a summary of our stress results for the Visund field. We compiled overburden, LOT, and RFT data from all 13 wells drilled in the Visund field. Each data point in this plot is derived as strictly as possible from the most reliable data from each well. The data for the minimum horizontal stress is derived from our analysis of leak-off test curves. Reported leak-off tests without pressure-time curves are not considered in this compilation. The well number is shown next to each data point. The vertical stress is derived using an overburden gradient averaged across the entire field. Small differences in the overburden gradients were detected, but the resulting stress profiles from these gradients were sufficiently similar such that we could neglect any differences. The pore pressure data is compiled from RFT's conducted in all of the wells in the field. Our constrained values for the maximum horizontal stress are shown in gray.

Note that the maximum horizontal stress is significantly larger than the vertical and minimum horizontal stresses, contrary to what other studies have found (Jørgensen and Bratli, 1995). However, our stress magnitudes are consistent with the strike-slip to reverse faulting stress field observed from earthquake focal plane mechanisms in the North Sea (Lindholm et al., 1995). Further evidence of recent reverse faulting deformation was seen in sub-seismic faults inferred from repeated sequences of Brent sands in the lithology logs of several wells. The existing deformation data therefore supports our prediction of high horizontal stresses in this region of the North Sea.

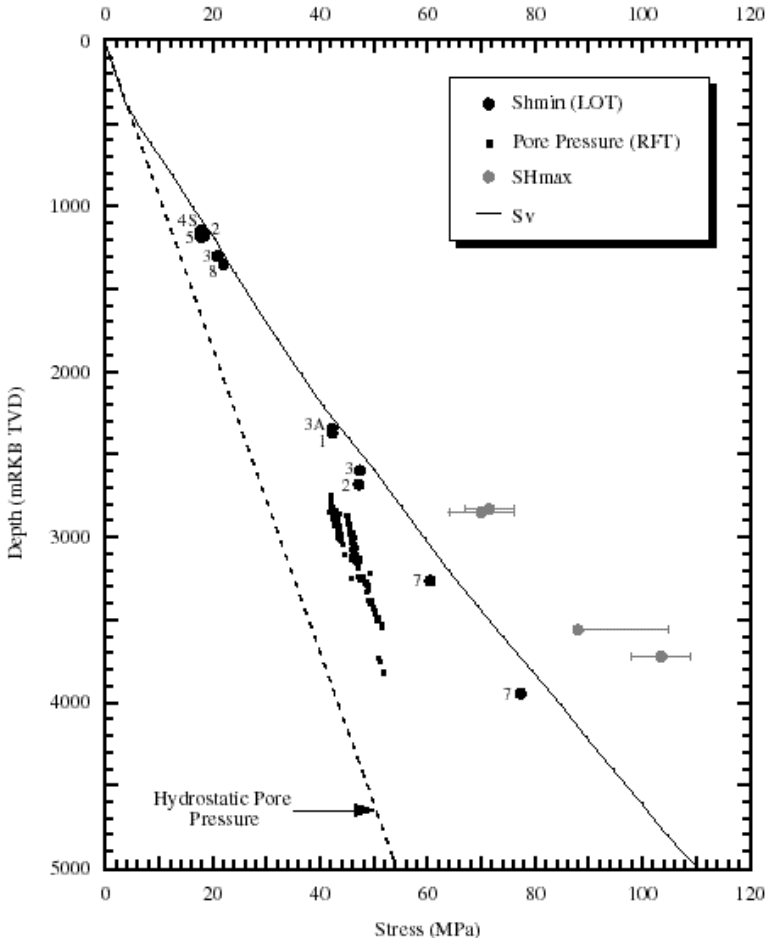

Figure 2.8: Stress Vs. Depth in Visund. Each stress point in this plot is derived as strictly as possible from the most reliable data in the field. Each leak-off test data point shows the well in which the test was run.

Table 1 provides a summary of the stress data found in each of the seven wells. Wells 4A and 4S did not have any interpretable tensile fractures as a result of poor image quality and low wellbore coverage. The tensile fractures observed in well 7 appear at depths far below any pore pressure or leak-off test measurements. We therefore do not provide estimates of stress magnitudes in well 7.

TABLE 1. Stress Tensor in Visund

Well	Log	SH Azimuth	Quality	Depth (mTVD)	SH Mag. (MPa)	Sh Mag. (MPa)	Sv Mag. (MPa)
4A	FMS	-	-	-	-	-	-
4S	FMS	-	-	-	-	-	-
6	FMS	101.2˚ ± 9.8˚	A	3720	103.5 ± 5.5	71.5 ± 1.5	77.3
7	FMS	97.3˚ ± 11˚	C	-	-	-	-
8	FMI	102.3˚ ± 9.9˚	C	3560	87 + 18	67.5 ± 1	71.2

TABLE 1. Stress Tensor in Visund

Well	Log	SH Azimuth	Quality	Depth (mTVD)	SH Mag. (MPa)	Sh Mag. (MPa)	Sv Mag. (MPa)
10S	FMI	97.1˚ ± 8.6˚	A	2830	71.5 ± 4.5	53.2 ± 1	55.6
11	FMI	106.9˚ ± 10.6˚	A	2850	70 ± 6	53.2 ± 1	56.1

2.5 Application to Wellbore Stability

Exploratory wells drilled in Visund prior to the spudding of well 10S frequently encountered drilling problems. Time was lost as a result of tight hole (i.e. hole pack-off, excessive overpull, or obstructions when running into the hole) and because of the extra time needed to ream the hole or circulate mud to clean cuttings from the bottom. Approximately 25% of the total downtime while drilling these holes was caused by hole-related, rather than equipment related, problems. Nearly 1200 cumulative hours of hole-related downtime, or approximately 10% of the total rig time, was lost on these holes. The time lost drilling these holes is almost equal to the time needed to drill well 5 to total depth of 3520 mTVD. Compressive wellbore failures, if not controlled, may cause drilling problems like hole collapse, stuck pipe, pack-off, and obstructions when running into the hole, as well as problems while producing the reservoir such as sand production. Prevention of wellbore failure requires that the circumferential stresses around the wellbore be minimized. Figure 9a shows a stereonet with the differential wellbore pressure ($\Delta P = P_m - P_p$) required to prevent compressive failures during drilling from growing beyond 90˚ in rock with 20 MPa uniaxial compressive strength. The stress state used in this analysis is the one found in the 10S well at 2830 mTVD. Figures 9b - 9e show cross-sections of wellbores for holes drilled in the directions shown in Figure 9a, and assume a differential wellbore pressure of 6 MPa. The cross-sections are cut perpendicular to the axis of the wellbore and show the compressive rock strength needed to prevent the rock from failing and falling into the hole. A north arrow is shown in Figure 9b for the vertical well, and the low side, or bottom, of the hole is shown if the well is inclined. Inclinations are shown next to each cross-section. As wells are increasingly inclined in the direction of the maximum horizontal stress (Figures 9b - 9d), the compressive rock strength needed to prevent failure decreases. A well drilled in this stress field would experience problems if drilled vertically with an insufficient mud weight, and would experience fewer drilling problems as the well was inclined in the direction of the maximum horizontal stress. The most stable orientation is a wellbore drilled horizontally in the direction of the maximum horizontal stress because the nearly isotropic vertical and minimum horizontal stresses would not create large

circumferential stress concentrations around the wellbore (Figure 9d). If a well were drilled in the direction of the minimum horizontal stress it would encounter a stress field similar to that found in a well drilled vertically (Figures 9b, 9e).

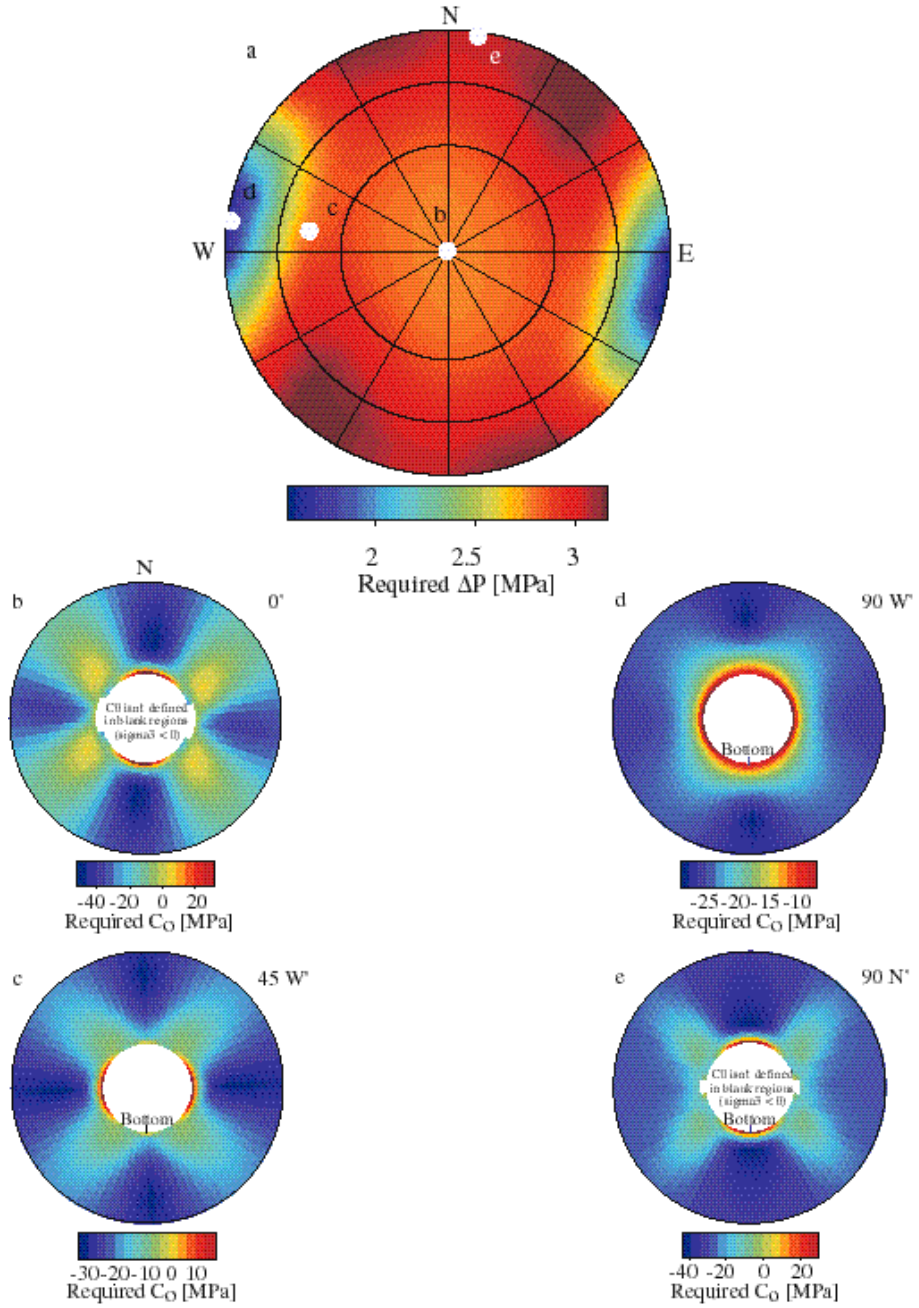

Figure 2.9: a) Stereonet showing the differential pore pressure needed to prevent compressive wellbore failures during drilling. The white points show the orientations of the wellbore cross-sections shown in parts b-e. The colors correspond to the compressive rock strength needed to prevent failure in different parts of the rock surrounding the hole. b) Vertical well. c) Well inclined 45˚ at an azimuth of 280˚. d) Horizontal well drilled toward SHmax. e) Horizontal well drilled toward Shmin.

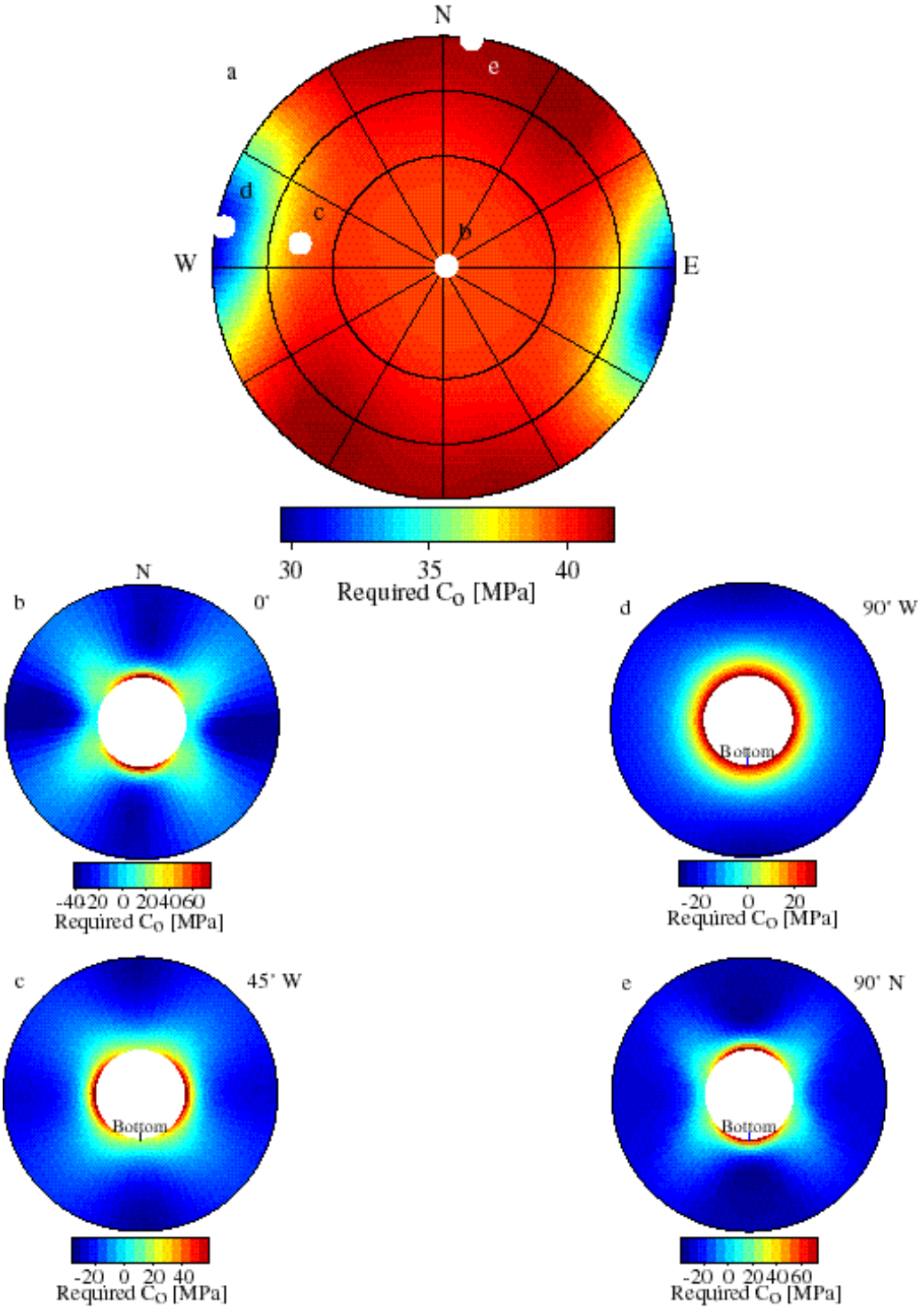

Figure 2.10: a) Stereonet showing the compressive rock strength needed to prevent wellbore failures after the completion of drilling. The white points show the orientations of the wellbore cross-sections shown in parts b-e. The colors correspond to the compressive rock strength needed to prevent failure in different parts of the rock surrounding the hole. b) Vertical well c) Well inclined 45˚ at an azimuth of 280˚. d) Horizontal well drilled toward SHmax. e) Horizontal well drilled toward Shmin.

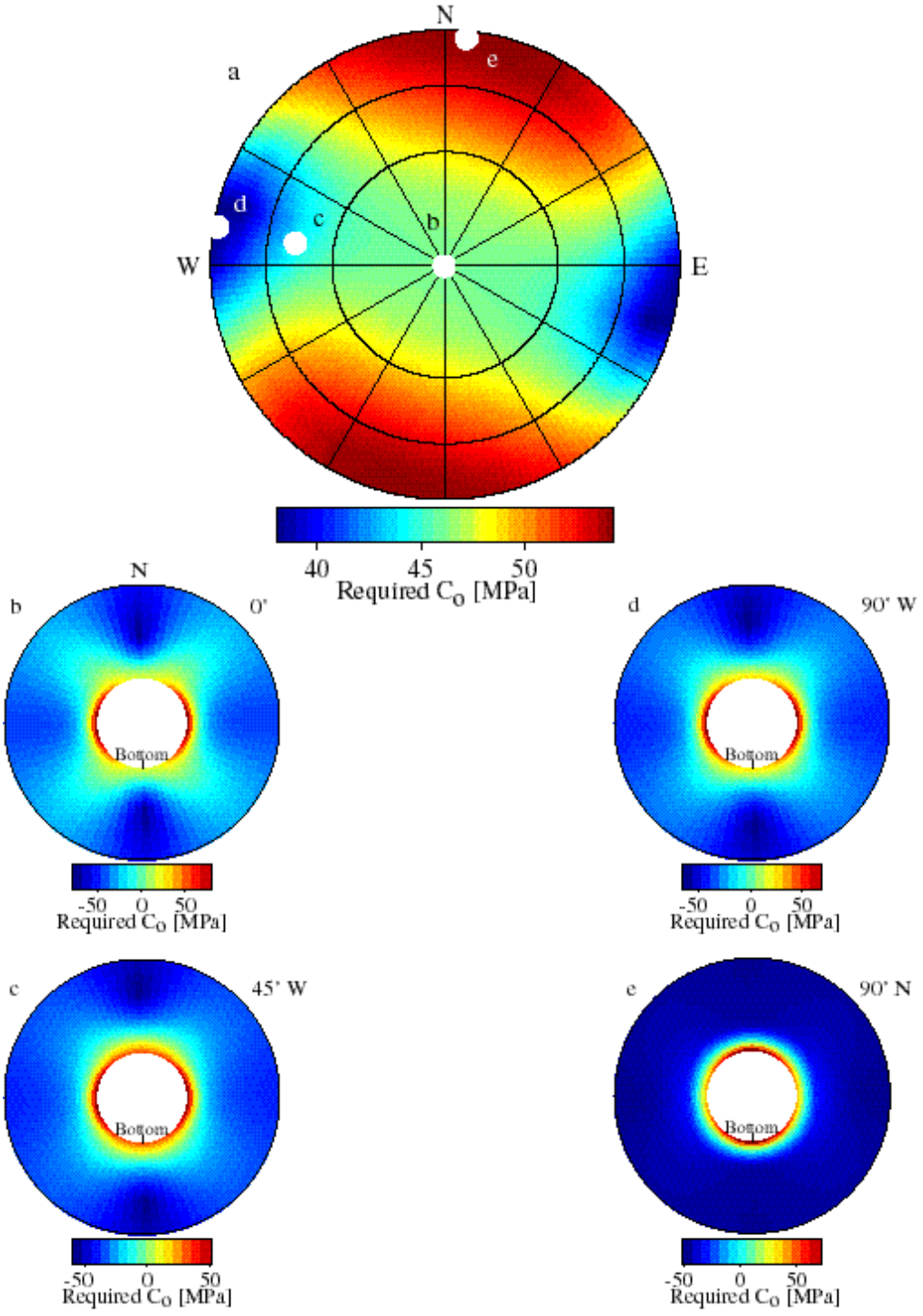

Figure 2.11: a) Stereonet showing compressive rock strength needed to prevent wellbore failures after pore pressure is drawn down by 10MPa and horizontal stresses reduced by 6.5 MPa. White points show orientations of wellbore cross-sections shown in parts b-e. Colors correspond to compressive rock strength needed to prevent failure in different parts of rock surrounding hole. b) Vertical well c) Well inclined 45˚ at an azimuth of 280˚. d) Horizontal well drilled toward SHmax. e) Horizontal well drilled toward Shmin.

Well 10S is deviated in the direction of the maximum horizontal stress, and it had the smallest amount of downtime of any well drilled in Visund. This well was also drilled with higher mud weights than were used in the previous eleven wells drilled in the field. The approach used in drilling this well is consistent with what we expect to be the best drilling strategy in Visund. The success of well 10S compared to every well drilled before it serves to show that our strategy of increasing the mud weight and drilling in an optimal direction would have been effective in reducing drilling problems encountered in wells 1 through 9.

Figure 10a shows the compressive rock strength needed to prevent breakouts from growing beyond 90˚ after the completion of drilling ($\Delta P = 0$), but before any pore pressure reduction has occurred. A wellbore drilled in the direction of the maximum horizontal stress would need compressive rock strengths as high as 30 MPa (Figures 10a, 10d) in order to prevent significant wellbore failure. Because the uniaxial compressive rock strength in the reservoir sands is as low as 9-10 MPa in some sands (and as low as 15-25 MPa in others), we expect the onset of sand production problems in the weaker sands almost immediately after the initiation of production.

Figure 11a shows the compressive rock strength needed to prevent breakouts from growing beyond 90˚ after the pore pressure in the reservoir has been drawn down by 10 MPa. We estimate the reduced horizontal stress by using a poroelastic model and a Poisson's ratio of 0.25, which reduces the horizontal stresses by 6.5 MPa (Engelder and Fischer, 1994). The maximum horizontal stress is 65 MPa and the minimum horizontal stress is 46.7 MPa in this case. Even if the well is drilled in the optimal drilling direction we expect sand production to become significant as the reservoir is drawn down (Figure 11d).

2.6 Conclusions

In this study we have shown that the full stress tensor can be reliably constrained using data that can be straightforwardly obtained as part of hydrocarbon field exploration and development. We demonstrate that in the Visund field, the maximum horizontal stress is significantly larger than the minimum horizontal and vertical stresses; and that our analysis is consistent with observations of recent deformation seen in studies of earthquakes and sub-seismic faults. We also show that the orientation of the stress tensor in this region is consistent both laterally and with depth.

Our analysis of wellbore stability illustrates that knowledge of stress magnitudes and orientations can be critical in designing successful exploration and production wells. By knowing the full stress tensor we are able to plan drilling strategies that minimize wellbore

failure during drilling, and sand production while producing the reservoir. A significant reduction in the number of drilling problems and the amount of downtime of the rig was realized in well 10S by modestly increasing the mud weight and by deviating the well in an optimally-stable direction.

CHAPTER 3

FAULT REACTIVATION AND FLUID FLOW ALONG A PREVIOUSLY DORMANT NORMAL FAULT IN THE NORTHERN NORTH SEA

Note that this chapter is an extended version of an article published with Mark D. Zoback as co-author in Geology, v. 28, no. 7 (July, 2000), pp. 595-598.

3.1 Abstract

Detailed seismic imaging, and in situ stress and pore-pressure measurements are used to analyze reverse-fault reactivation of a long-dormant normal fault in the northern North Sea. Fault reactivation is caused by three factors: (1) a recent increase in the compressional stress in the area associated with postglacial rebound, (2) locally elevated pore pressure due to the presence of natural gas in a hydrocarbon reservoir on the footwall side of the fault, and (3) a fault orientation that is nearly optimally oriented for frictional slip in the present-day stress field. We demonstrate that the combination of these three factors induces fault slippage and gas leakage along sections of the previously sealing reservoir-bounding fault. We argue that similar pore-pressure triggering of fault slip in the crust may occur because of the accumulation of gas columns of CO_2, He, etc., in the vicinity of tectonic faults.

3.2 Introduction

In this study we consider fault reactivation and fluid flow in the Visund oil and gas field in the context of in situ stress and locally high pore pressures due to gas accumulation in a reservoir abutting a long-dormant normal fault. The mechanical role of fluids has long been of interest to scientists studying earthquakes and faulting (see review by Hickman et al., 1992). There are several well-studied cases in which seismicity was induced by high pore pressures resulting from fluid injection at depth (Healy et al., 1968; Raleigh et al., 1976; Zoback and Harjes, 1997). Sahagian and Proussevitch (1992) suggested that high pore pressure due to a buoyant column of gas at the top of magma chambers may be responsible for triggering volcanic eruptions, and Linde et al. (1994) and Sturtevant et al. (1996) suggested that gas dissolution from magma during the passage of seismic waves may trigger further seismicity in geothermal areas.

3.3 Visund oil and gas field

The Visund field is located offshore Norway in the easternmost major fault block of the Tampen spur (Færseth et al., 1995) along the western edge of the Viking graben (Figure 1, inset). The reservoir is divided into several oil and gas compartments, some of which are separated by the A-Central fault. As shown in Figure 1, low seismic reflectivity along the southern part of the A-Central fault is interpreted to be the result of gas leakage from the reservoir. The data in this region are very high quality and there are no changes in lithology that might account for the change in seismic reflectivity. The question of how faults affect

the migration of fluid in petroleum reservoirs is complicated, as faults are known to act as both barriers and conduits. Some faults contribute dramatically to formation permeability (Finkbeiner et al., 1998), yet others provide effective barriers separating distinct reservoir compartments (Hunt, 1990).

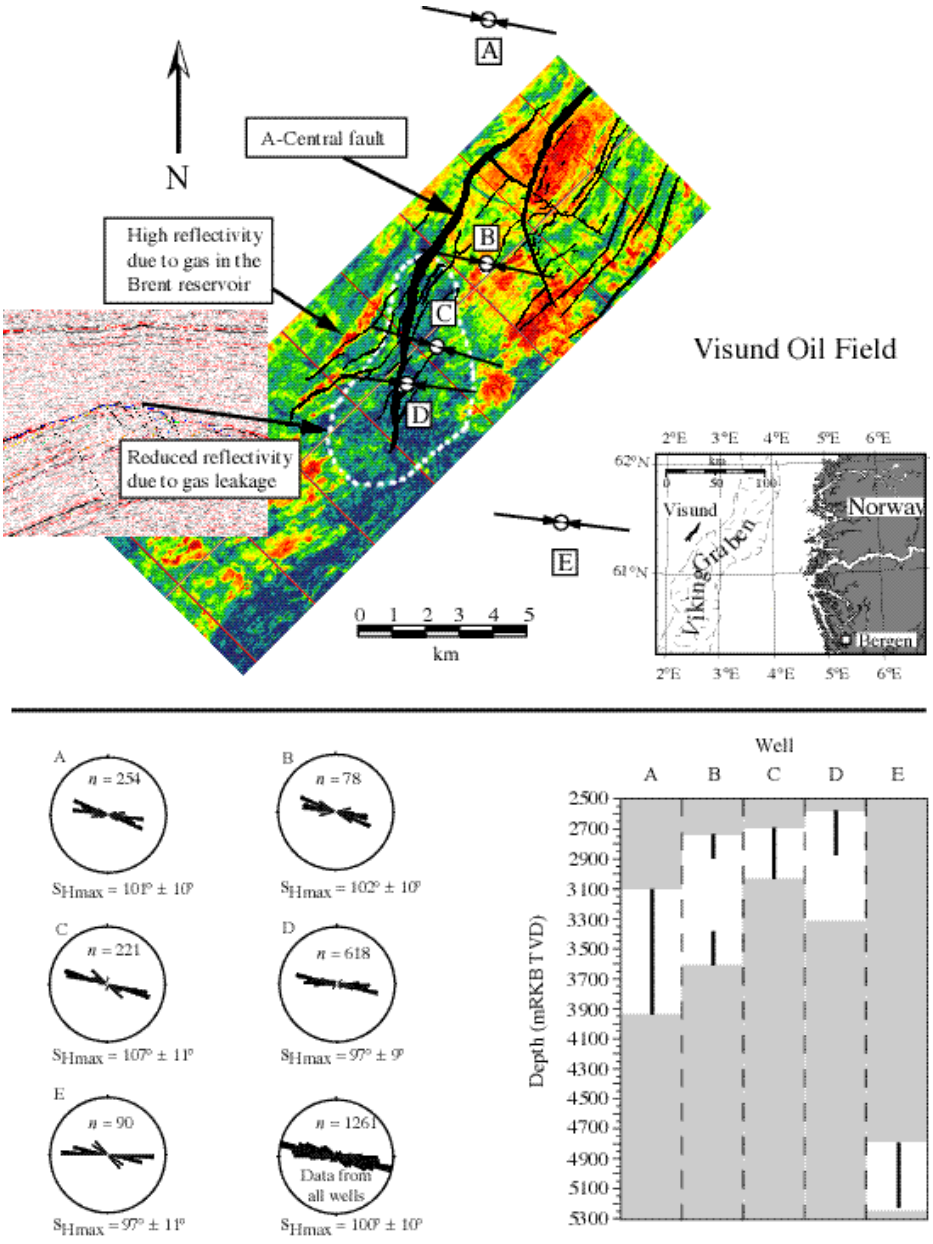

Figure 3.1: Map view of Visund field showing seismic reflectivity of reservoir horizon as well as mean orientation of maximum horizontal stress in five wells (A-E). Inset shows location of Visund field with respect to coast of Norway and Viking graben. Rose diagrams show range of orientations seen in each well. To right of rose diagrams, depths (meters relative to kelly bushing, true vertical depth) over which data could be seen in each well are shown by black lines. Gray regions indicate parts of well that were not logged.

Figure 1 also shows the orientation of the maximum horizontal stress determined in five wells in and near the Visund field from observations of drilling-induced tensile wall fractures (Moos and Zoback, 1990; Brudy and Zoback, 1993, 1999). Drilling-induced tensile wall fractures have been shown to be reliable indicators of the direction of the maximum horizontal stress (Brudy et al., 1997). Five rose diagrams in the lower part of Figure 1 show the consistency of maximum horizontal stress orientations in each well. Each rose diagram shows the mean orientation of the maximum horizontal stress, the $\pm 2\sigma$ error in this orientation, and the number (n) of times the tensile fractures in each well could be subdivided into 0.2-m-long intervals. The final rose diagram shows a compilation of the entire data set. The depths over which the data were observed in each well are shown by vertical black lines in the plot to the right of the rose diagrams. The orientation of the maximum horizontal stress is remarkably consistent, both laterally across the field and with depth.

Figure 2A shows a summary of in situ stress and pore-pressure data for the Visund field over the depth range of principal interest. The pore-pressure data are direct measurements conducted with the Schlumberger Repeat Formation Tester. The vertical stress shown in Figure 2A was derived by using the average overburden gradient for the entire field. We calculated the overburden in each well by integrating density logs. The data for the minimum horizontal stress were derived from analysis of carefully conducted leak-off tests (LOTs) in wells throughout the field. The magnitude of the maximum horizontal principal stress was determined from analysis of the drilling-induced tensile fractures (following Brudy et al., 1997). Determinations of stress magnitude and orientation are described in detail by Wiprut and Zoback (2000). Note that we are able to fit lines quite well to the principal stresses and that the maximum horizontal stress is distinctly larger than the vertical stress, and the minimum horizontal stress is nearly equal to the vertical stress. This result is consistent with the strike-slip and reverse-slip stress field indicated by earthquake focal-plane mechanisms in this part of the North Sea (Lindholm et al., 1995). It is also consistent with the observation of inversion structures resulting from normal faults newly reactivated as reverse faults offshore Norway (Rohrman et al., 1995; Vågnes et al., 1997) and bordering other sections of the northeast Atlantic Margin (Doré and Lundin, 1996). The inset of Figure 2A shows a detailed view of the pore-pressure measurements in the three wells closest to the A-Central fault. Well D was deviated to penetrate the A-Central fault at 2933m true vertical depth (indicated by the horizontal dashed line), whereas wells B and C were drilled vertically. The steep pressure gradient in well D is the result of light oil rather than free gas. A free gas cap was not detected in well D, which is consistent with the reduced seismic reflectivity shown in Figure 1. The pore-pressure data in well D are

discussed in more detail subsequently.

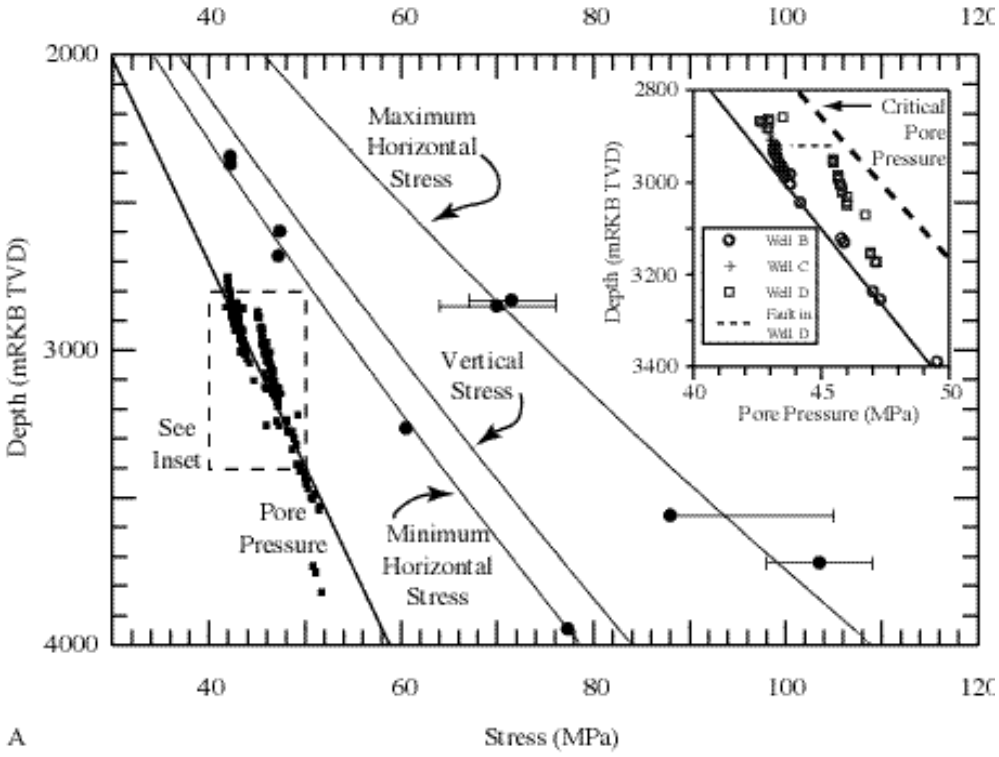

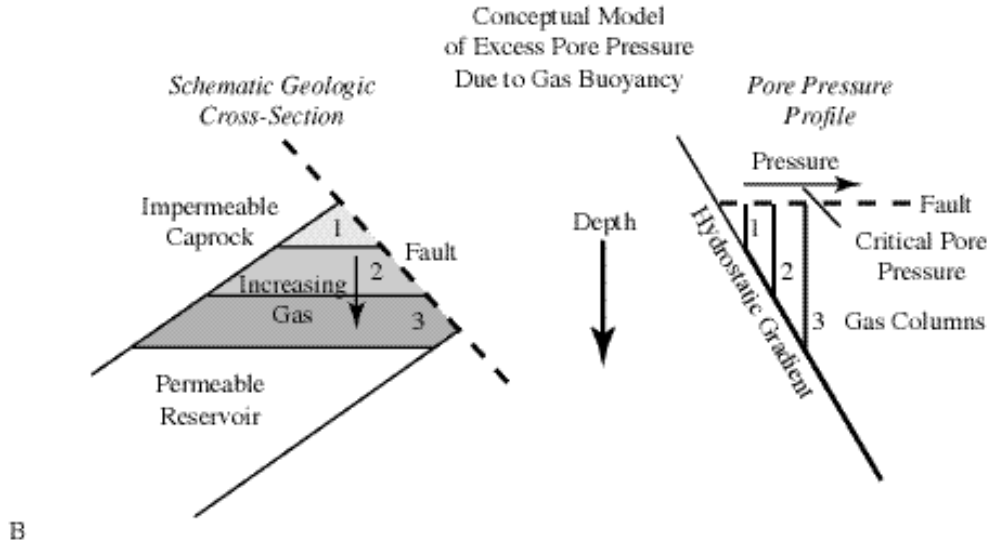

Figure 3.2: A: In-situ stress and pore-pressure data obtained from wells throughout Visund field (Wiprut and Zoback, 2000). Best-fit lines to data are shown. Inset shows pore-pressure measurements in three wells drilled close to A-Central fault. Depths are same as in Figure 1. B: Conceptual model showing increase in pore pressure at a reservoir-bounding fault as a result of an increasing gas column in reservoir.

Figure 3A shows a map view of the top Brent reservoir horizon with the faults, lateral extent of gas leakage (dashed line, see Fig. 1), and mean orientation of the maximum horizontal stress in five wells drilled in this field superimposed on the structural contours. The Brent reservoir consists of a ridge running northeast-southwest with a saddle crossing perpendicular to the ridge between wells B and C. Comparison of the map in Figure 1 and Figure 3A shows the ridge is trapping gas along most of its length except for the portion of the ridge defined by the dashed low-reflectivity area. The southern boundary of the Brent reservoir plunges steeply into the Viking graben as a result of a large northeast-southwest trending graben-bounding fault. The effect of the graben-bounding fault can be seen in Figure 1 as well, where there is a sharp transition from high to low reflectivity in the southern portion of the map.

Figure 3B shows a schematic cross-section running approximately east-west through well D and the A-Central fault. In this area, the A-Central fault juxtaposes Brent reservoir sandstones on the footwall side with cap-rock shales (at the base of the Cretaceous unconformity) on the hanging-wall side at the top of the fault. The A-Central fault developed during the Jurassic as a normal fault with an ~60˚ dip (Færseth et al., 1995) and as much as 300 m of normal throw (Linn Arnesen, Norsk Hydro, 1998, personal communication). Since that time, the fault appears to have rotated and now dips between 30˚ and 45˚. As already mentioned, the focal-plane mechanisms of earthquakes occurring in the vicinity of the Visund oil field (at 5 to 30 km depth), the inversion structures observed in this region, and the in situ stress measurements shown in Figure 2A indicate that the current state of stress in this area is highly compressional. As earthquakes along passive continental margins such as Norway's are quite rare, a number of investigators have suggested that the compressional stress observed in this region may be related to lithospheric flexure associated with Pleistocene deglaciation (Stephansson, 1988; Klemann and Wolf, 1998; Grollimund et al., 1998). If this interpretation is correct, the existence of the current compressional stress in this area is a geologically recent (~10,000-15,000 yr old) phenomenon.

Figure 4 shows two views of the A-Central fault as determined from three-dimensional seismic reflection data. In the upper part of Figure 4, a map view of the fault is shown along with the orientation of the maximum horizontal stress in the three wells closest to the fault. The shaded area shows the lateral extent of gas leakage (simplified from Figure 1). In the lower part of Figure 4, a perspective view of the approximately east-dipping fault surface is shown. The fault surface is colored to show the likelihood of leakage along the surface, and is discussed in further detail below. A dark circle on the fault plane indicates the point where well D penetrates the A-Central fault.

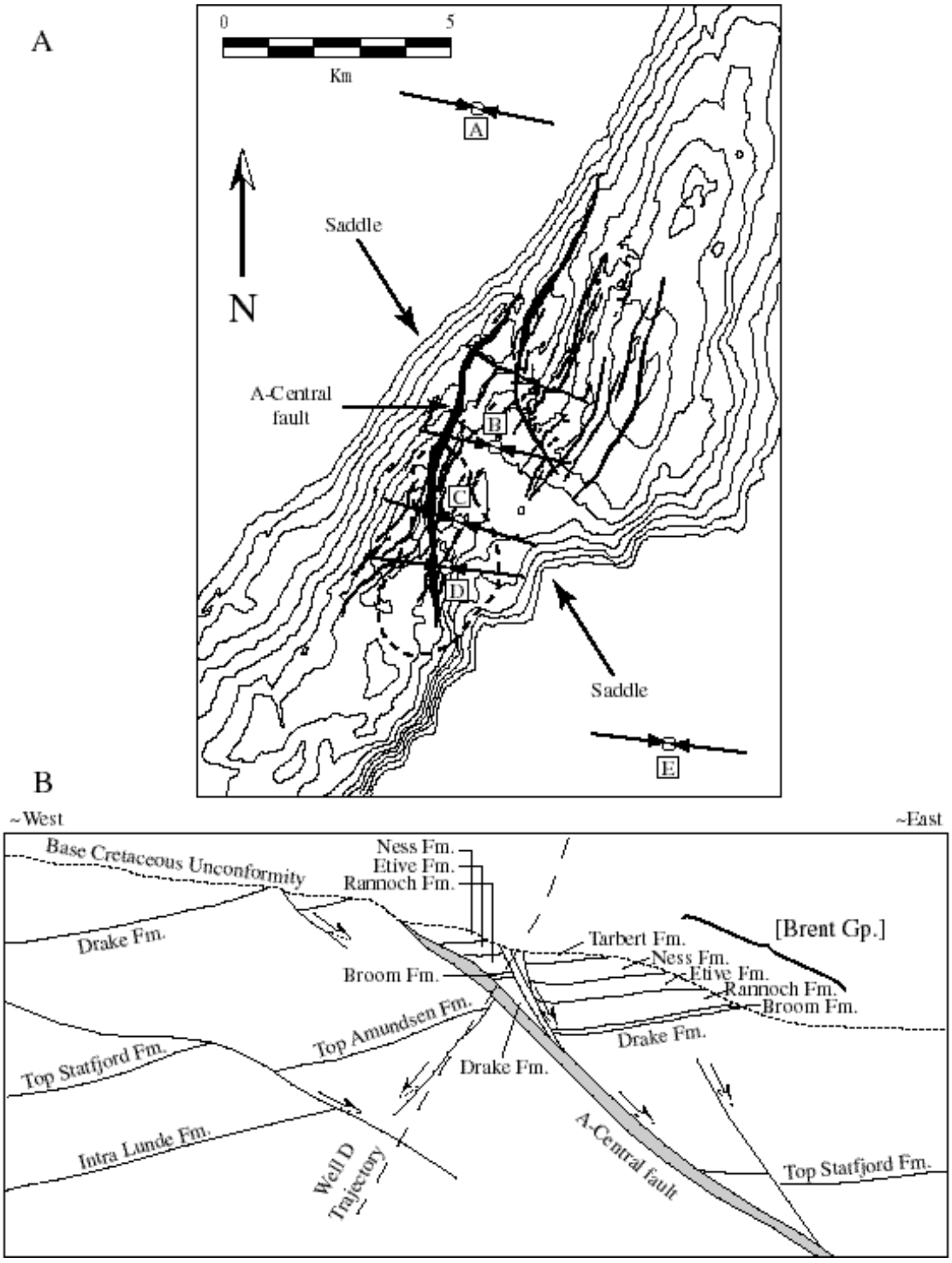

Figure 3.3: A: Contour map of top Brent reservoir horizon. Region of gas leakage inferred from reduced seismic reflectivity shown by dashed line (see Fig. 1). Faults and orientation of maximum horizontal stress in five wells also shown. Saddle defines local structural low along reservoir horizon. B: East-west cross-section through Visund field. Cap rock defined by short-dashed base Cretaceous unconformity. Trajectory of well D through A-Central fault shown with long dashes.

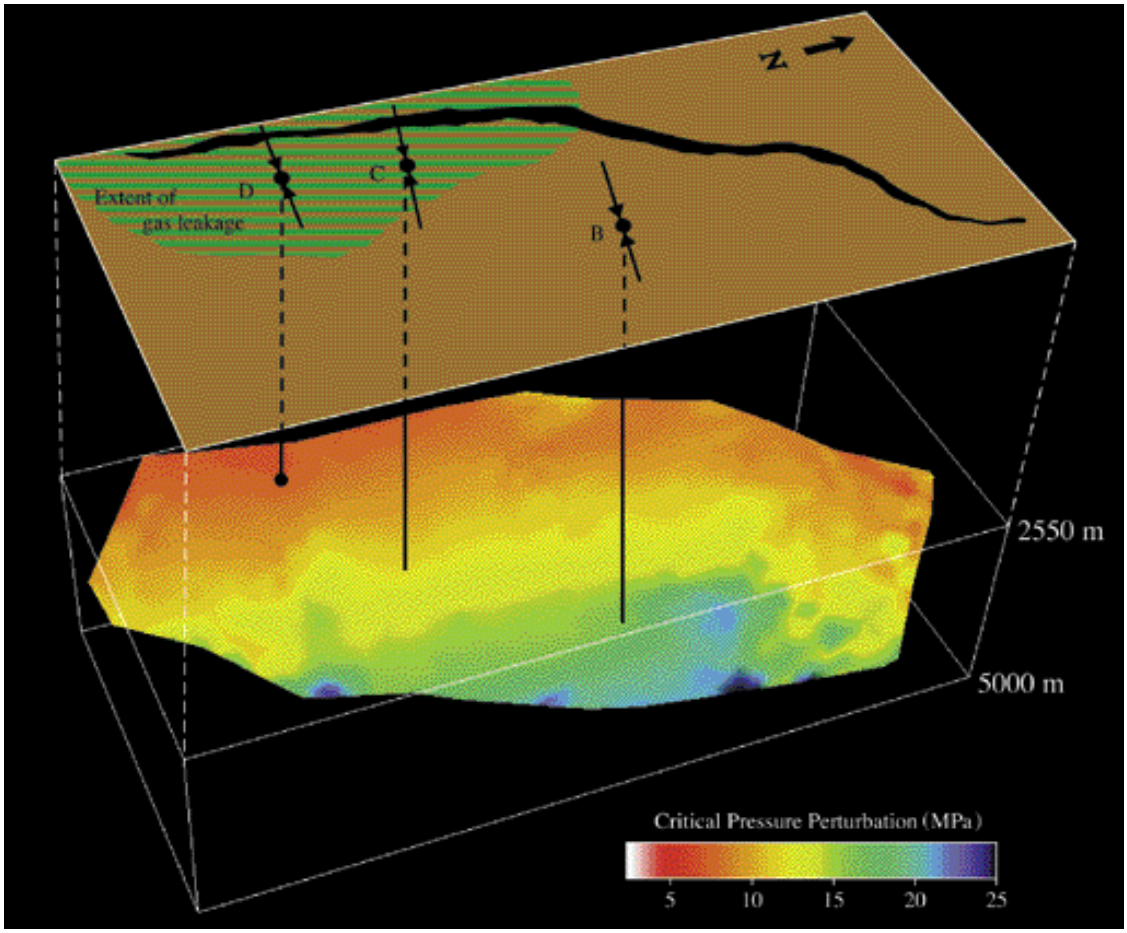

Figure 3.4: Map view and perspective view of A-Central fault as determined from three-dimensional seismic reflection survey. Map view shows region of gas leakage as inferred from reduced seismic reflectivity (see Fig. 1). Perspective view is colored to show excess pore pressure needed to induce fault slip in the current stress field (see text). The part of the fault that is most likely to slip corresponds to that which appears to be leaking.

3.4 Fault slip and hydrocarbon leakage

The evidence for gas leakage in the immediate vicinity of the A-Central fault points to the fault as a possible conduit by which the hydrocarbons are escaping from the reservoir. To investigate this possibility further, we evaluated the state of stress and pore pressure acting on the fault plane in the context of the hypothesis that faults that are critically stressed in the current stress field (i.e., capable of slipping) are permeable, whereas those that are not critically stressed are not permeable. A number of permeability studies in fractured and faulted rock masses appear to confirm this hypothesis (Barton et al., 1995,

1998; Hickman et al., 1998). Figure 2B shows how we apply this hypothesis conceptually to the A-Central fault. As gas accumulates in a permeable reservoir bounded by a sealing fault, the pore pressure at the fault-reservoir interface increases because the pore-pressure gradient in the gas is considerably less than the hydrostatic gradient owing to the extremely low density of gas. As the height of the gas column increases, at some point the pore pressure will be sufficient to induce fault slip, providing a mechanism to increase fault permeability and allow leakage from the reservoir.

To evaluate the hypothesis that parts of critically stressed faults are permeable and are the cause of localized leakage, we resolve the stress orientations and stress magnitudes shown in Figures 1 and 2A onto distinct ~100 m x 100 m triangular elements on the fault plane to determine the shear and normal stress on each part of the A-Central fault. Figure 5 shows a flow chart explaining how we massage the data to create the leakage potential map from the triangular fault elements (see Figure 4). We use Coulomb frictional failure to

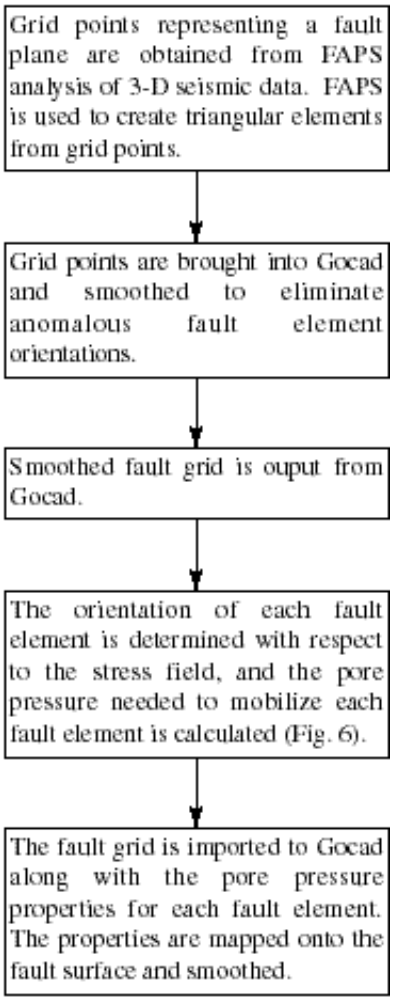

Figure 3.5: Steps in fault leakage analysis.

determine which fault element is expected to slip. Coulomb frictional failure is defined in Eqn. 1, where τ is the shear stress, σ_n is the effective normal stress, and μ is the coefficient

$$\tau = \mu\sigma_n \qquad \text{Eqn. 3.1}$$

of sliding friction. Given that the effective normal stress is the difference between the normal stress (S_n) and the pore pressure (P_p), we solve Eqn. 1 to determine the pore pressure at which a fault element will begin to slip (Eqn. 2). We refer to this pore pressure

$$P_p = S_n - \tau/\mu \qquad \text{Eqn. 3.2}$$

as the critical pore pressure. In order to calculate the shear and normal stress we determine the orientation of the unit normal to the fault element in a coordinate system defined by the stress field. Figure 6A shows the fault element defined in the stress coordinate system. S_1, S_2, and S_3 are the principal stresses, a, b, and c are the vertex points of the fault element, $\hat{\mathbf{n}}$ is the unit normal to the fault element, and t is the traction acting on the surface of the fault element. The unit normal to the fault element is defined in Eqn. 3, where f and g are any two

$$\hat{\mathbf{n}} = \frac{\mathbf{f} \times \mathbf{g}}{|\mathbf{f}||\mathbf{g}|} \qquad \text{Eqn. 3.3}$$

vectors defined by the points a, b, and c. The traction acting on the fault plane is the product of the stress tensor and unit normal vector (Eqn. 4). The stress tensor is defined in Eqn. 5.

$$t = \mathbf{S}\,\hat{\mathbf{n}} \qquad \text{Eqn. 3.4}$$

$$\mathbf{S} = \begin{bmatrix} S_1 & 0 & 0 \\ 0 & S_2 & 0 \\ 0 & 0 & S_3 \end{bmatrix} = \begin{bmatrix} S_{Hmax} & 0 & 0 \\ 0 & S_v & 0 \\ 0 & 0 & S_{hmin} \end{bmatrix} \qquad \text{Eqn. 3.5}$$

We obtain the stress magnitudes from Figure 2A using the middle depth of each fault element. Taking the dot product of the unit normal vector and the traction vector gives the magnitude of the normal stress (Eqn. 6), and the magnitude of the shear stress is determined

$$S_n = \hat{\mathbf{n}} \bullet t \qquad \text{Eqn. 3.6}$$

by the Pythagorean theorem (Eqn. 7). We calculate the critical pore pressure at which the

$$\tau^2 = t^2 - S_n^2 \qquad \text{Eqn. 3.7}$$

fault element will slip using equations 2, 6, and 7 and by assuming a coefficient of sliding friction of 0.6 (Byerlee, 1978). Figure 6B shows a graphical representation of the preceding calculation. A fault element is plotted as a point within the 3-D Mohr circle according to the shear and normal stress resolved on the fault element. The slope of the Coulomb frictional failure line passing through the fault element point uniquely defines the critical pore pressure at the point where the failure line intersects the normal-stress axis.

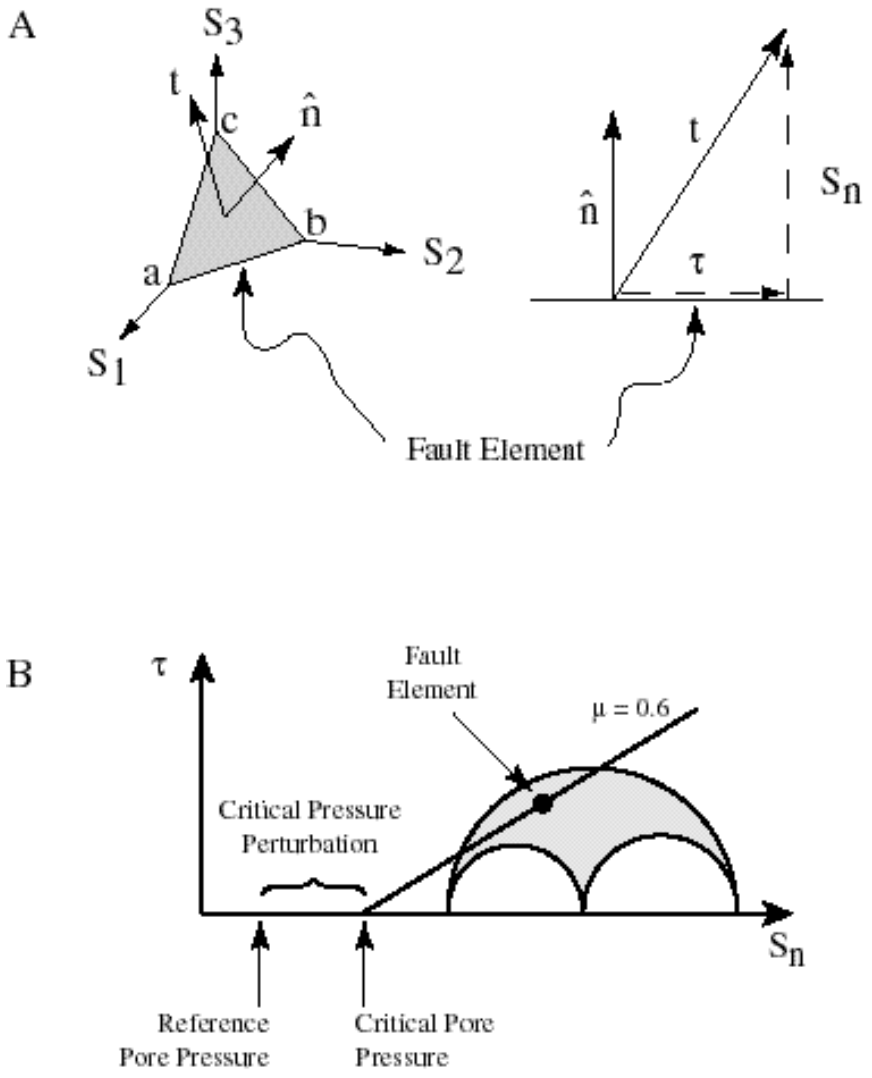

Figure 3.6: A: Orientation of a fault element in stress field. B: Mohr-Coulomb plot showing determination of critical pore pressure and comparison to reference pore pressure.

The color shading on the fault plane shown in Figure 4 indicates the difference between the critical pore pressure and the reference pore pressure line shown in Figure 2A. This difference is called the critical pressure perturbation (Figures 4, 6B). Red colors in Figure 4 indicate that a small increase in pore pressure (<~7 MPa) is enough to bring the fault to failure. Blue colors indicate that the pore pressure must rise significantly (>20 MPa) before those parts of the fault will begin to slip in the current stress field.

Note that the largest parts of the A-Central fault that are most likely to slip (i.e., shaded in red) are located along the same part of the fault where leakage seems to be occurring. Thus, there appears to be a good qualitative correlation between the critically-stressed-fault criterion and the places along the fault where leakage appears to be occurring. Because well D penetrates the fault in this area, we can evaluate this correlation more quantitatively. As shown in the inset of Figure 2A, the pressure below the fault (indicated by the position of the dashed horizontal line) is within ~1 MPa of the theoretical critical pore pressure for fault slippage (the thick dashed line). This value is several megapascals above the background pore pressure, just as predicted in Figure 4. Above the fault, pore pressures are significantly reduced, indicating that there is poor pressure communication across the fault. The A-Central fault is connected at its southern end with the graben-bounding fault described above, preventing hydrocarbons from migrating from the footwall to the hangingwall. Geochemical analysis of gas from both sides of the fault indicates that the hydrocarbons are derived from different sources (i.e., no fluid flow across the fault) (Arnd Wilhelms, Norsk Hydro, 1998, personal communication). It is interesting to note that although the pore pressure in the footwall appears to have caused the A-Central to slip and leak, both the footwall and hangingwall show reduced seismic reflectivity. Increased permeability resulting from fault slip seems to influence every pore pressure compartment in contact with the fault. The pore pressures shown in the inset of Figure 2A indicate wells B, C, and D are in the same pressure compartment on the hangingwall, yet well B does not penetrate an area of reduced reflectivity. This is the result of the saddle shown in Figure 3. The local structural low provided by the saddle effectively separates the gas in well B from wells C and D. Because leakage appears to be localized to the region where the fault is most likely to slip, fault slip rather than capillary-pressure effects seem to be responsible for the gas leakage. Thus, in this case, as with cases reported by Barton et al. (1995), Hickman et al. (1998), and Finkbeiner et al. (1998), fault slip appears to have principally promoted fault-parallel flow.

Pore-pressure-induced faulting and leakage may be a dynamic mechanism that acts to control the hydrocarbon capacity of reservoirs bounded by faults. In Visund the hydrocarbon column heights were smaller than expected (Roald Færseth, Norsk Hydro,

2000, personal communication). Because high water-phase pore pressure brings the fault closer to failure, the potential hydrocarbon column height is diminished. Figure 7 demonstrates the combined effect of high water-phase pore pressure and leakage along reactivated faults on the height of the hydrocarbon column. This effect was observed in the Gulf of Mexico (Finkbeiner et al., 1998) where only small amounts of hydrocarbon could be trapped against reservoir-bounding faults near frictional failure, whereas larger columns could be trapped against faults of different orientation, or with lower water-phase pore pressures, initially further from failure.

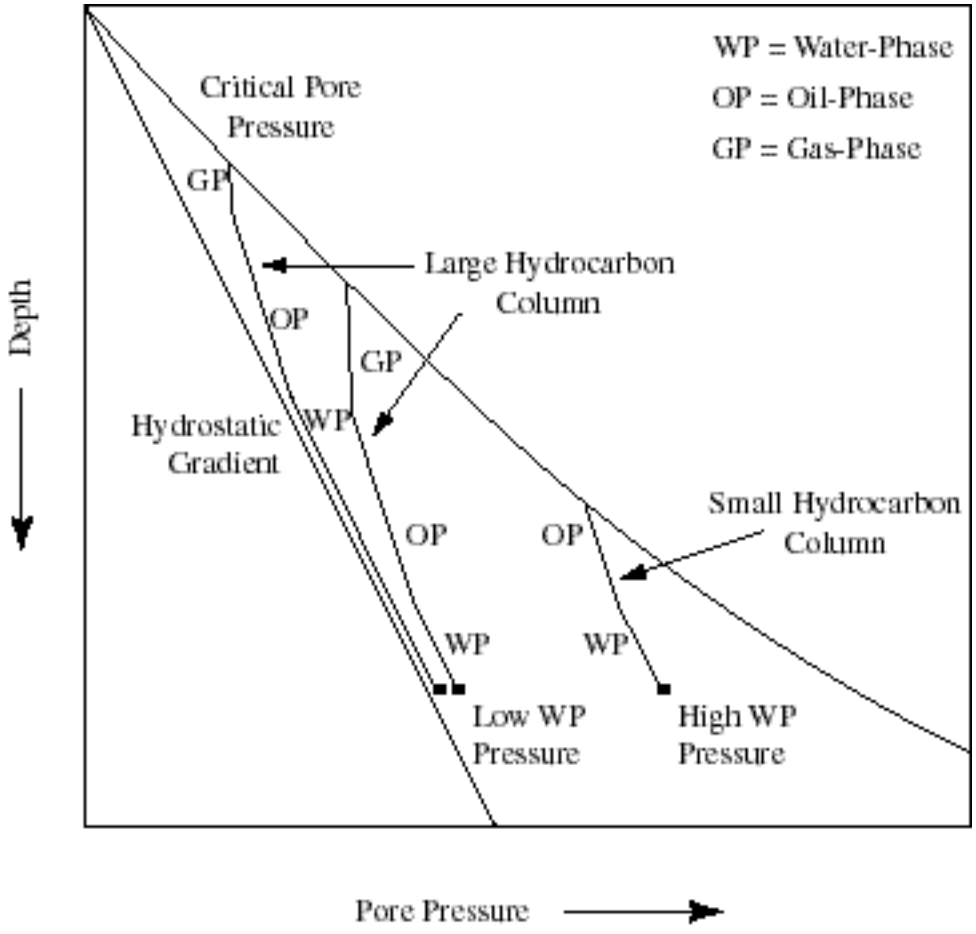

Figure 3.7: Schematic diagram showing effect of high water-phase pressure on potential hydrocarbon column height. Note that the hydrocarbon column is large even with very large water columns. High water-phase pore pressures greatly diminish the potential height of the hydrocarbon column.

It is not clear at this time whether leakage along the A-Central fault is an episodic or steady-state condition. It is possible that once sufficient gas leaks out of the reservoir to reduce the pore pressure, the fault may seal again. The reservoir could subsequently be

recharged by hydrocarbons migrating in from neighboring regions, as chemical analysis of the hydrocarbons in the Visund field and the surrounding areas indicates. This could be the mechanism by which the pore pressure increases to the critical value where the fault fails. It may also be the case that once the fault has been reactivated, it remains permeable, and the hydrocarbons would leak continuously from the reservoir.

The relationship between pressure and fluid flow along reservoir-bounding faults such as the A-Central fault is reminiscent of a pressure-regulated valve. Pore pressure acting against an initially sealing fault can rise only to a certain value before fault slippage occurs and hydrocarbons leak upward along the fault through the cap rock. Sibson (1992) has speculated that some tectonic faults act as valves that (while closed) allow near-lithostatic pore pressures to accumulate. After a pressure-induced earthquake occurs, fracturing of the crust in the region surrounding the earthquake increases permeability and dissipates the high pore pressure. Because columns of naturally occurring nonhydrocarbon gases in the crust (CO_2, He, etc.) can get trapped against locked sections of active tectonic faults, it is perhaps reasonable to speculate that the excess pressure associated with the buoyancy of these gas columns may be capable of nucleating fault slippage. This possibility is especially interesting as increased fluxes of mantle-derived He and CO_2 have been documented in the vicinity of the San Andreas fault (Kennedy et al., 1997).

CHAPTER 4

IN SITU STRESS AND PORE PRESSURE IN FIELD 1, FIELD 2, AND FIELD 3 OIL AND GAS DISCOVERIES

4.1 Abstract

In this study I examine drilling-induced wellbore failures in sixteen exploration wells scattered throughout the Field 1, Field 2, and Field 3 oil and gas discoveries in the northern North Sea. I use observations of drilling-induced tensile and compressive wellbore failures as well as density, pore pressure, and leak-off test measurements to estimate the magnitudes and orientations of all three principal stresses. Most wells yield a consistent orientation of the maximum horizontal stress. Those wells that do not show a consistently oriented direction of maximum horizontal stress either have too little data to confidently constrain the orientation of the stress tensor, or the stress field is perturbed by a nearby fault. I show that the three principal stresses (S_v, S_{hmin}, and S_{Hmax}) are consistent with depth and reflect a strike-slip to reverse faulting stress regime. The maximum horizontal stress is shown to be higher than the vertical and minimum horizontal stresses in all three fields. In general, the maximum horizontal stress orientations rotate from an orientation of approximately 100˚ in the Visund field (Chapter 2) to approximately 90˚ in Field 1 and Field 2, and 80˚ in Field 3. The maximum horizontal stress magnitudes in Visund are slightly higher than the stress magnitudes in Field 1 and Field 2; and those magnitudes are in turn higher than in Field 3, as predicted by Grollimund and Zoback (2000).

4.2 Introduction

Constraint of the stress tensor in oil fields is critical for addressing both engineering problems and geologic problems. In this chapter a stress analysis similar to the analysis done in Visund (Chapter 2) is done for Field 1, Field 2, and Field 3 oil and gas discoveries. The results of these analyses can be used for addressing issues of wellbore collapse during the exploration and production of these fields, as well as being applicable to problems of hydrocarbon leakage and migration. In each field, observations of drilling-induced compressive failures and wellbore tensile failures are integrated with other routinely available wellbore information to constrain the full stress tensor. Field 1, Field 2, and Field 3 are treated separately in this chapter. A section exists for each field, explaining the process of interpreting tensile failures in each well, constraining the vertical and minimum horizontal stresses, and modeling the maximum horizontal stress. Compilations of the stress orientation and stress magnitude results for each field are shown in each section.

A map showing the locations of major oil and gas discoveries is shown in Figure 1. All three fields are located within this region.

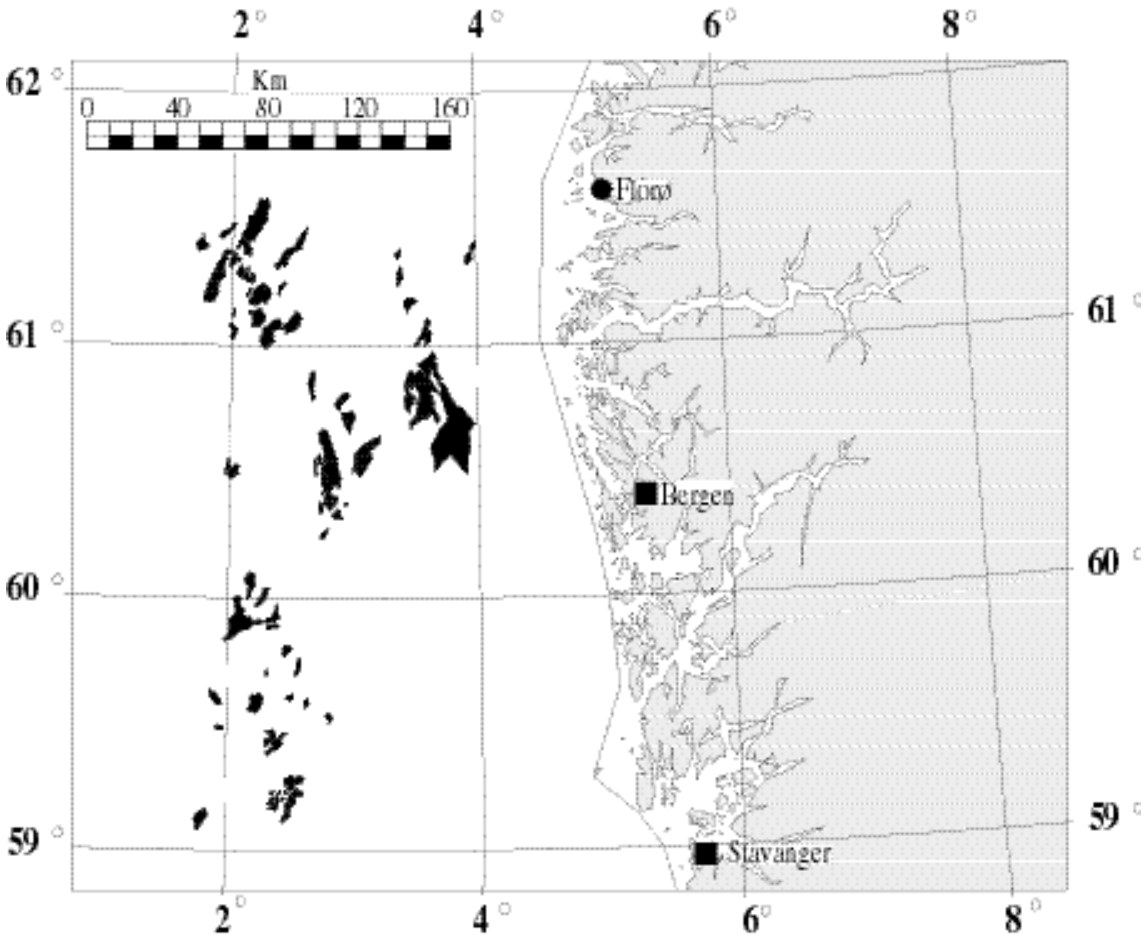

Figure 4.1: Map of northern North Sea showing west coast of Norway and major offshore oil and gas discoveries. Map is modified from Norwegian Petroleum Directorate, 1997.

4.3 Field 1

4.3.1 Observations of wellbore failure

Figure 2 shows a map of Field 1. Formation MicroScanner and Formation MicroImager (FMS/FMI) logs were examined to determine whether drilling-induced tensile fractures could be seen in wells 1S, 2 and 3. Extensive drilling-induced tensile fractures were detected in all three wells. Examples of this type of data are shown in Appendix B. The azimuth of the drilling-induced tensile fractures is plotted as a function of depth in Figure 3. In each case, black data points represent tensile fractures that are aligned with the axis of the wellbore, and data points representing tensile fractures that are inclined with respect to

the axis of the wellbore are shown in gray. Error bars for near-axial tensile fractures show the variation in azimuth of each fracture; while error bars for inclined tensile fractures show the portion of the wellbore circumference spanned by each fracture. Near the center of each plot, bit trips and “wash and ream” operations are shown by horizontal and vertical lines respectively. A bit trip is plotted each time the drill string is run into the hole. This operation may cause a significant rise in mud pressure at the bottom of the hole due to a piston effect. Washing and reaming the hole involves scraping the hole clean, and may remove evidence of drilling-induced tensile fractures. There is no visible correlation between the occurrence (or absence) of tensile fractures and these special drilling operations, suggesting that the tensile fractures formed (or did not form) during normal drilling operations, rather than as a result of extreme conditions in the well such as tripping the bit or reaming the hole.

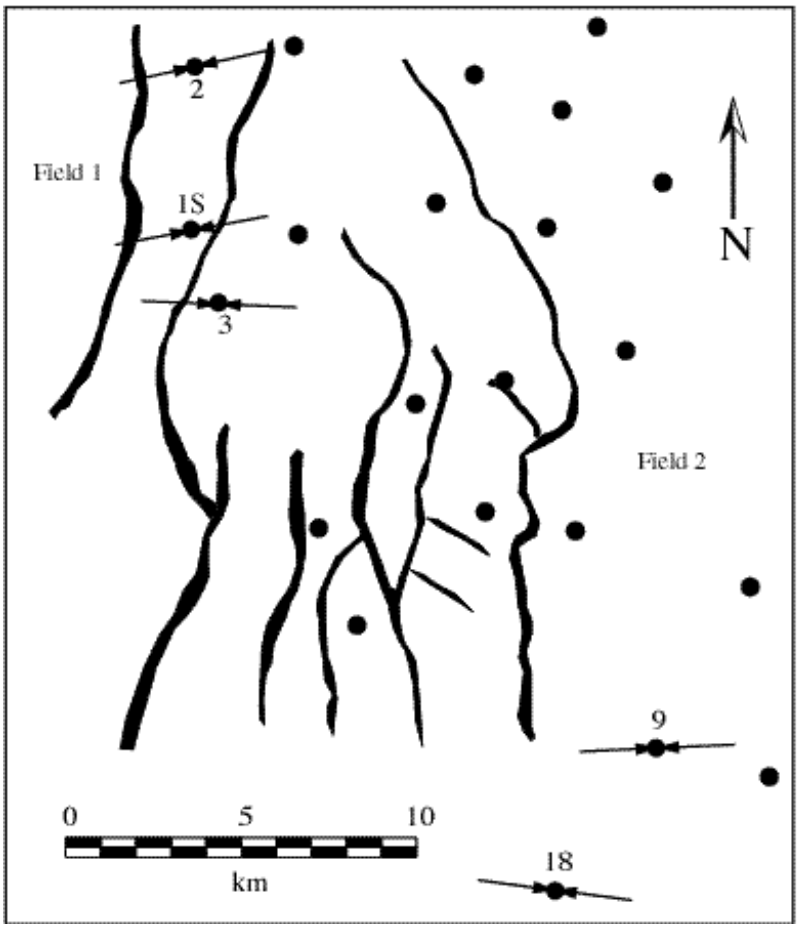

Figure 4.2: Generalized map of Field 1 and Field 2 showing the orientation of the maximum horizontal stress (inward pointed arrows), exploration wells (circles), and major faults.

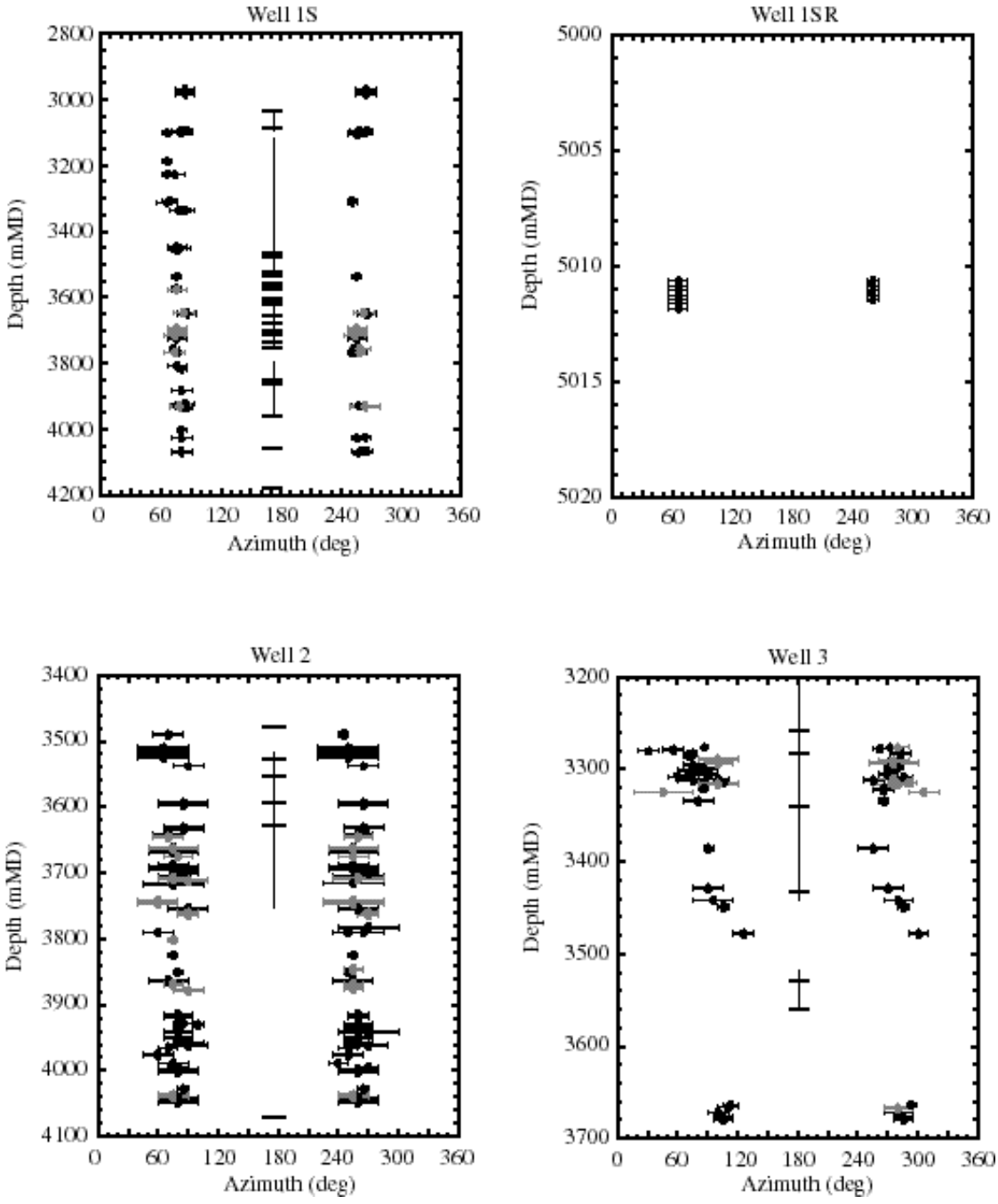

Figure 4.3: Azimuth (degrees from North) of drilling-induced tensile fractures as a function of depth (relative to drilling rig floor) measured along wellbore.

Although both near-axial and inclined tensile fractures were detected in these wells, in order to determine the orientation of the stress field in this region only the orientation of tensile fractures aligned with the wellbore axis will be considered. A circular statistical method developed by Mardia (1972) is used to obtain the mean azimuth and standard

deviation of the maximum horizontal stress for each well shown in Figure 4. The uncertainty in the azimuth represents two standard deviations from the mean. The frequency is calculated by adding the tensile fractures in 0.2m intervals. The rose plots are normalized by the number of data points, and therefore the length of the bars does not reflect the relative frequency of the tensile fractures between wells. Well 1SR has too little data to claim the tensile fractures are representative of the tectonic stress field.

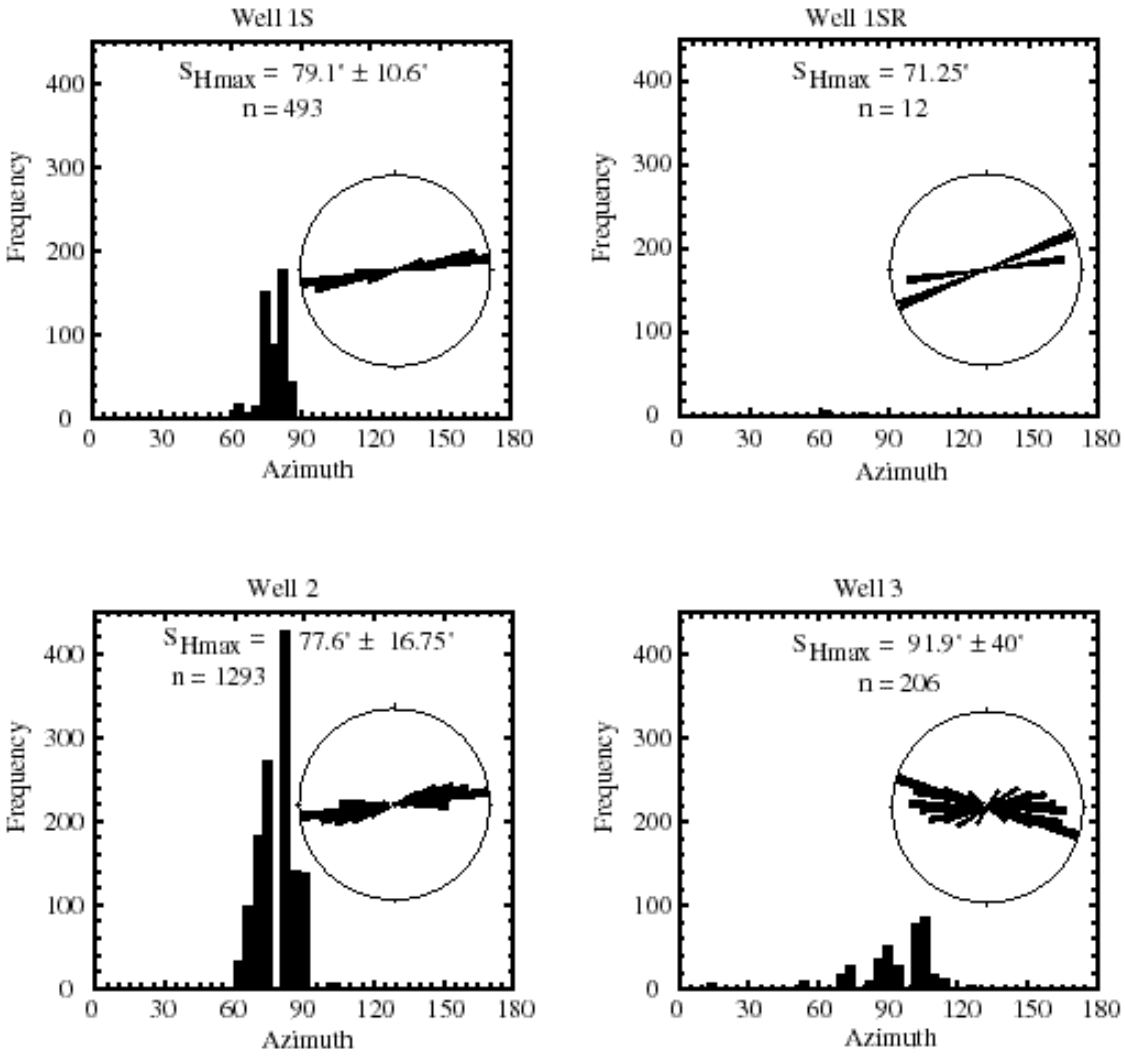

Figure 4.4: Histograms and rose diagrams showing orientation of maximum horizontal stress. Azimuth is measured in degrees from north, and frequency represents number of 0.2m observations (n) within each 4˚ azimuth bin. Note that rose diagrams are normalized in each well and do not reflect differences in amount of data between wells. Statistics follow Mardia (1972).

While there is a large uncertainty in the orientation of the data in well 3, a close examination of the tensile fractures and preexisting faults shows some of this data are representative of the tectonic stress field and other parts of the data are anomalous. The

tensile fractures in well 3 show a strong rotation between 3400 and 3500 meters and are absent between 3500 and 3660 meters (Figure 3). This stress anomaly is not observed in the other two wells and is most likely the result of a localized anomaly due to slip on a preexisting fault penetrated by this well. The fault which is potentially responsible for this anomaly was identified in both seismic and the FMS data. From the FMS data the fault is seen cutting the well between 3645 and 3659 meters. The relationship between anomalous stress fields and slip on faults has been noted by other authors (e.g. Shamir and Zoback, 1992; Barton and Zoback, 1994; Paillet and Kim, 1987).

4.3.2 In situ stress and rock strength

We utilize the interactive software package, Stress and Failure of Inclined Boreholes (SFIB), developed by Peska and Zoback (1995), to constrain the maximum horizontal stress magnitudes and to put limits on rock strength. Estimation of the maximum horizontal stress requires prior knowledge of the vertical stress, the minimum horizontal stress, the pore pressure, the mud weight, and the change in temperature at the wellbore wall during drilling. Final well reports provided by Norsk Hydro contain this information. We analyze each well individually so that estimates of the maximum horizontal stress are not affected by data from wells in different pore pressure compartments or with slightly differing overburden stresses. The vertical stress, S_v, used in this study was derived from integrated density logs. We derive the minimum horizontal stress, Shmin, from Leak-off Tests (LOT) and Formation Integrity Tests (FIT) conducted in each well (see Gaarenstroom et al., 1993). The pore pressure, P_p, was obtained from Repeat Formation Tests (RFT). In order to use a reliable pore pressure value the stress analysis in each well was conducted as close as possible to an RFT depth. We derive a mud weight value, P_m, from the maximum static mud weight. Use of the highest mud density value is required since it is impossible to determine the precise mud weight at which the tensile cracks initiated. Although the tensile fractures may have formed at mud pressures lower than the ones we use, our utilization of the highest mud pressure allows us to calculate a reasonable lower bound for the maximum horizontal stress. An upper bound for the maximum horizontal stress is derived from our analysis of rock strength and compressive failures in these wells. The amount of cooling at the wellbore wall was estimated from temperature gradient plots and from best estimates provided by drilling engineers. Each well is assumed to too cool by as much as 50˚C. This upper bound for the cooling also provides the most conservative lower bound estimate for the maximum horizontals stress. Figures 5, 6 and 7 show the analysis for the maximum horizontal stress, S_{Hmax} in wells 1S, 2 and 3 respectively. The plots represent the allowable stress state at a given depth constrained by 1) Mohr-Coulomb frictional faulting theory for

the crust assuming a coefficient of sliding friction of 0.6 (Byerlee, 1978) (four sided polygon), and 2) compressive and tensile wellbore wall failures (thick short dashes and long dashes respectively) (see Moos and Zoback, 1990, for an explanation). Stress magnitudes that fall above the short dashed tensile failure contour (assumed to be zero in this study) indicate stress states consistent with the occurrence of drilling-induced tensile fractures, while values that fall below indicate no tensile failures should occur. Similarly, for a given rock strength, stress magnitudes that fall above one of the long dashed compressive failure contours indicate breakouts should occur, while those that fall below indicate no breakouts should be observed. We constrain the maximum horizontal stress only where tensile fractures were observed in each of these wells, meaning the stress state must be such that it falls above the short dashed tensile failure line in our figures. While coefficients of sliding friction may be as high as 1.0 in some rocks, faults in sediments tend to have lower coefficients of friction. We consider a coefficient of friction of 0.6 to be an upper bound in this case, as the sediments are poorly cemented and consolidated.

Constraining S_{Hmax} in well 1S

At 3450 mTVD the minimum horizontal stress was determined to be 67.6 MPa (Figure 5). Assuming a ±1 MPa error in this estimate provides the upper and lower bounds for both the minimum and maximum horizontal stresses. The lower bound of the minimum horizontal stress gives an estimate of the lower bound of the maximum horizontal stress of 92 MPa. The upper bound of the maximum horizontal stress is constrained by the stress polygon, and is 103 MPa. The rock strength measured in the lab was between 35 and 40 MPa. A small breakout was detected from the FMS log and a single arm caliper measurement shows the hole is much larger than bit size. These observations are consistent with the stress field seen from modeling the drilling-induced tensile fractures. Since the upper bound of the maximum horizontal stress is constrained by the stress polygon it is not as well constrained as the lower bound. We therefore assume the lower bound is the best estimate of the maximum horizontal stress at this depth (92 MPa).

At 3550 mTVD the minimum horizontal stress was determined to be 70.4 MPa. The lower bound of the maximum horizontal stress in this case is 101 MPa, and the upper bound is 111 MPa. In this case no breakout could be seen in the FMS log, but the single arm caliper shows the hole size is much larger than the bit size. Rock strength measured in the lab for this depth is between 40 and 50 MPa. The compressive failure analysis is consistent with the tensile failure analysis at this depth as well. At this depth we again assume the lower bound is the best estimate of the maximum horizontal stress (101 MPa).

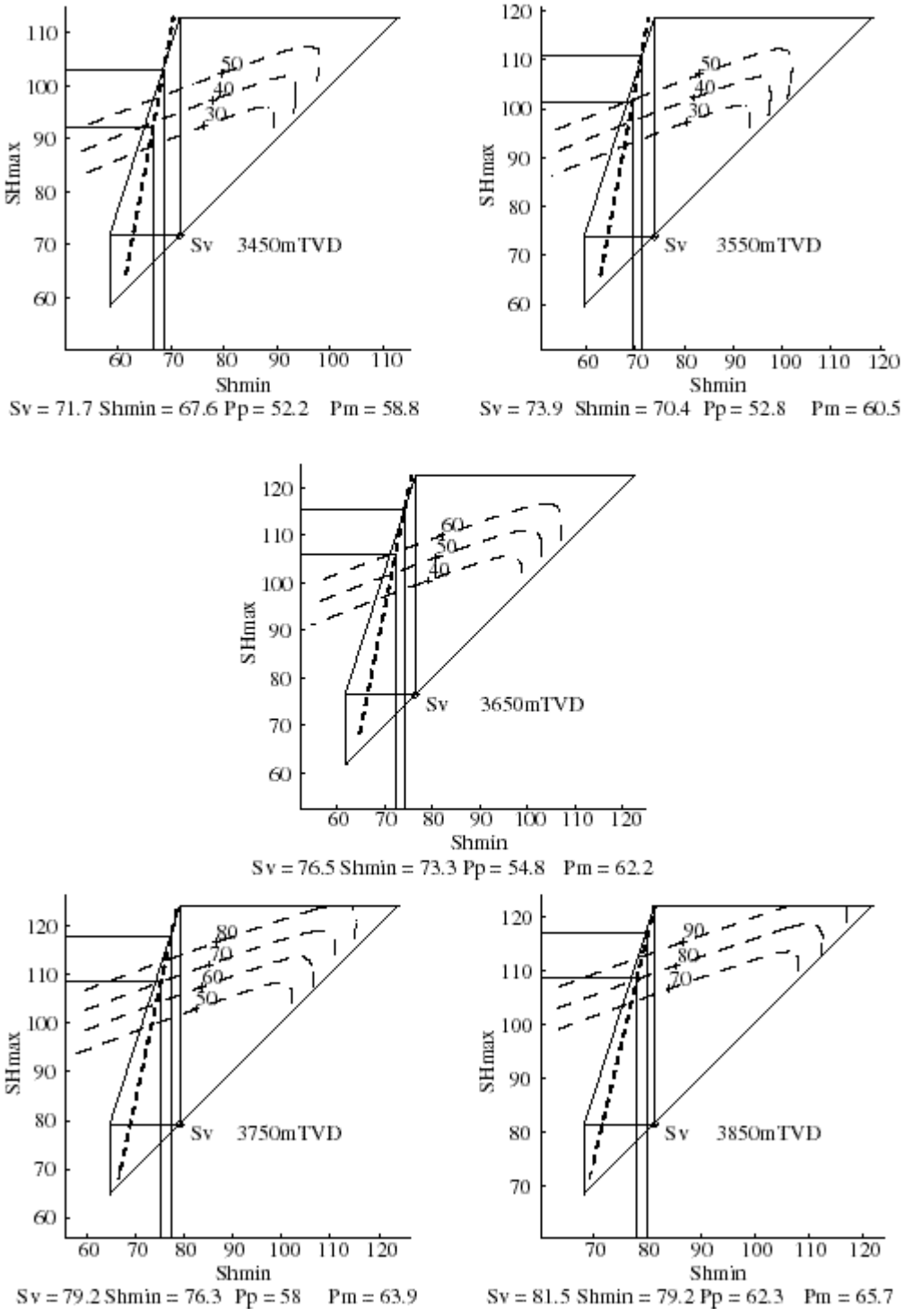

Figure 4.5: Stress polygons showing constrained values of maximum horizontal stress in well 1S. Each analysis is done at a specific depth shown to right of vertical stress. Relevant stress inputs (in MPa) are shown below each polygon. Tensile failure contours are thick short dashes, and breakout contours are long dashes. Each breakout line represents a different rock strength value, as shown, assuming that a breakout width of 40˚ would be required to be detected by wide pads of FMI tool.

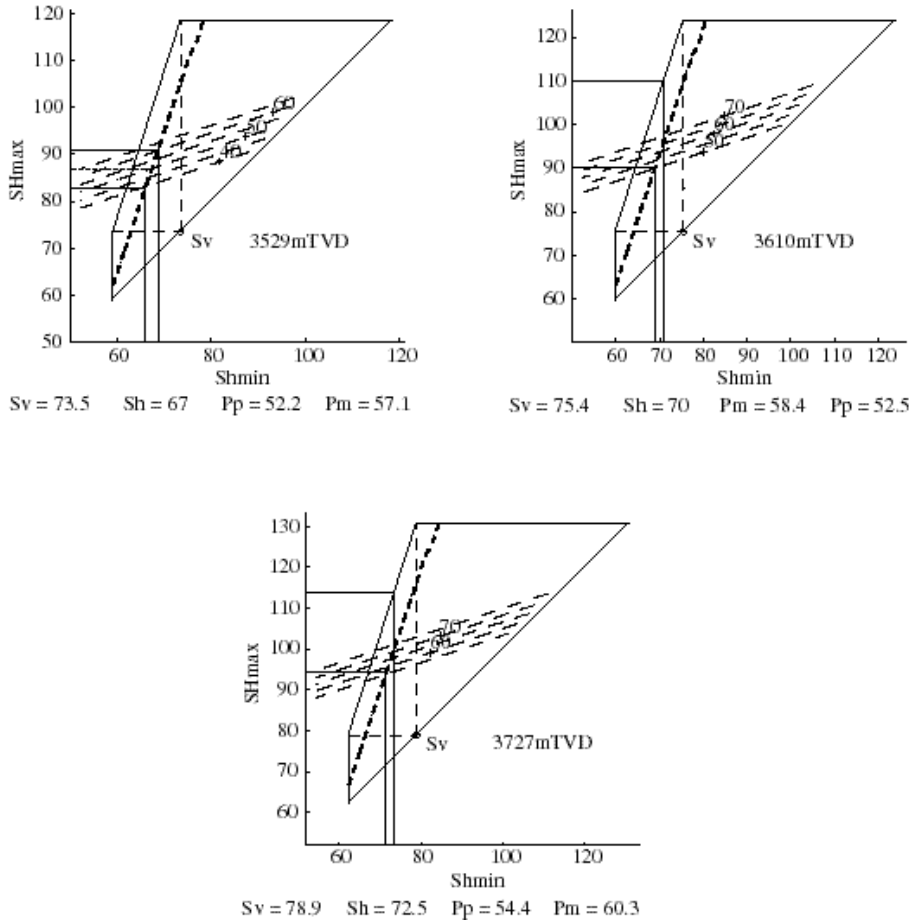

Figure 4.6: Stress polygons showing constrained values of maximum horizontal stress in well 2. See figure 4.5 for explanation.

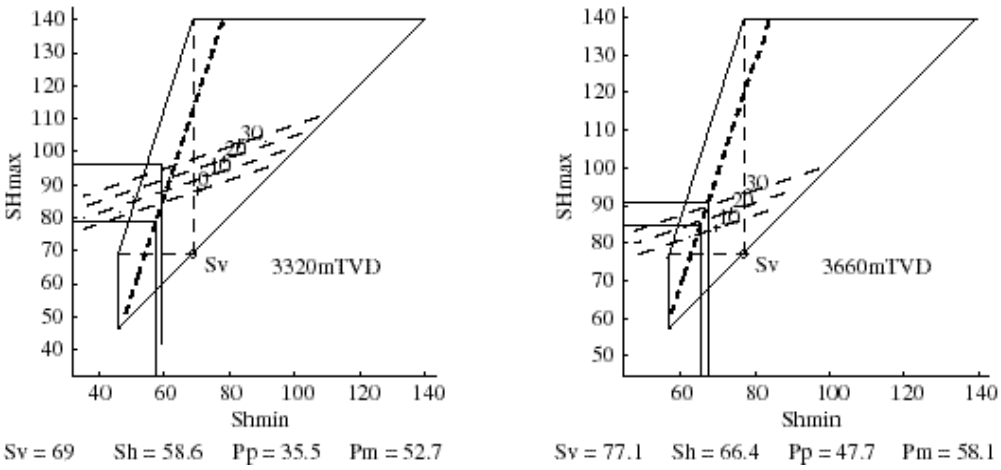

Figure 4.7: Stress polygons showing constrained values of maximum horizontal stress in well 3. See figure 4.5 for explanation.

At 3650 mTVD the minimum horizontal stress was determined to be 73.3 MPa. The lower bound of the maximum horizontal stress in this case is 106 MPa, and the upper bound is 115 MPa. There were no rock strength measurements at this depth, and the hole size is only slightly larger than the bit size. The best estimate of the maximum horizontal stress at this depth is given by the lower bound (106 MPa).

At 3750 mTVD the minimum horizontal stress was determined to be 76.3 MPa. The lower bound of the maximum horizontal stress in this case is 109 MPa, and the upper bound is 118 MPa. There were no rock strength measurements at this depth and the hole size is larger than bit size. A breakout was also observed in the FMS image. These observations allow us to place an upper bound estimate on the rock strength at this depth. Since breakouts will not form if the stress falls below the compressive failure line for a given rock strength, the lower bound of the maximum horizontal stress suggests that the rock strength cannot be greater than approximately 70 MPa. The best estimate of the maximum horizontal stress at this depth is given by the lower bound (109 MPa).

At 3850 mTVD the minimum horizontal stress was determined to be 79.2 MPa. The lower bound of the maximum horizontal stress in this case is 109 MPa, and the upper bound is 117 MPa. There were no rock strength measurements at this depth and the hole is in gage. Assuming the lower bound of the maximum horizontal stress is the best estimate, the absence of breakouts at this depth suggests the rock strength is greater than approximately 80 MPa. The best estimate of the maximum horizontal stress at this depth is given by the lower bound (109 MPa).

Constraining S_{Hmax} in well 2

At 3529 mTVD the minimum horizontal stress was determined to be 67 MPa (Figure 6). The lower bound of the maximum horizontal stress is 83 MPa. The upper bound of the maximum horizontal stress is constrained by noting the absence of breakouts in the caliper and image logs. The rock strength measured at this depth is between 50 and 60 MPa. If the rock strength is 50 MPa then the upper bound of the maximum horizontal stress is 87 MPa (shown by dashed horizontal line). If the rock strength is 60 MPa then the upper bound of the maximum horizontal stress is 91 MPa. The best estimate of the maximum horizontal stress at this depth is determined by taking the mean value of the higher upper bound and the lower bound values of S_{Hmax} (87 MPa). This estimate may be high if the rock strength is less than 60 MPa.

At 3610 mTVD the minimum horizontal stress was determined to be 70 MPa. The lower bound of the maximum horizontal stress is 90 MPa, and the upper bound is constrained by the stress polygon and is 110 MPa. No breakouts were detected in the caliper

or image logs at this depth, and there are no rock strength measurements. The stress results imply the rock strength is at least approximately 52 MPa at this depth. The best estimate of the maximum horizontal stress at this depth is given by the lower bound (90 MPa).

At 3727 mTVD the minimum horizontal stress was determined to be 72.5 MPa. The lower bound of the maximum horizontal stress is 94 MPa, and the upper bound is constrained by the stress polygon and is 114 MPa. No breakouts were detected in the caliper or image logs at this depth, and there are no rock strength measurements. The stress results imply the rock strength at least approximately 57 MPa at this depth. The best estimate of the maximum horizontal stress at this depth is given by the lower bound (94 MPa).

Constraining S_{Hmax} in well 3

At 3320 mTVD the minimum horizontal stress was determined to be 58.6 MPa (Figure 7). The lower bound of the maximum horizontal stress is 79 MPa. The upper bound of the maximum horizontal stress is determined by noting the absence of breakouts in the caliper and image logs. The rock strength at this depth in nearby wells is approximately 35 MPa, giving an upper bound of the maximum horizontal stress of 96 MPa. The best estimate of the maximum horizontal stress is determined by taking the mean value of the upper and lower bounds (87.5 MPa).

At 3660 mTVD the minimum horizontal stress was determined to be 66.4 MPa. The lower bound of the maximum horizontal stress is 85 MPa. The upper bound is determined by noting the absence of breakouts. The rock strength at this depth in surrounding wells is approximately 35 MPa, giving an upper bound of the maximum horizontal stress of 90 MPa. Since the rock strength is likely greater at this depth than at 3320 meters we have probably under-estimated the upper extent of the possible maximum horizontal stress. We therefore use the upper bound as our best estimate of the maximum horizontal stress (90 MPa).

4.3.3 Field 1 Summary

Inclined tensile fractures were detected in the deeper portions of well 1S. If the wellbore azimuth is aligned with one of the principal stress axes, then tensile fractures which are aligned with the axis of the wellbore should be detected. Inclined tensile fractures form when the wellbore is deviated with respect to the stress tensor. The inclined tensile fractures are not detected in well 1S until approximately 3600 meters. Wells 1S was deviated at an azimuth of approximately 260˚ to the west starting at 2600 meters. The maximum deviation along the wellpath is approximately 40˚. At 3600 meters the well turns from an azimuth of 260˚ to an azimuth of 280˚. This wellpath is rotated 20˚ clockwise from the orientation of

the maximum horizontal stress, and may be the reason inclined tensile fractures begin to form as the well becomes deeper. The tensile fractures continue to form in the steeply deviated portion of well 1S unlike the tensile fractures in Visund well 10S. This is likely the result of both the higher pore pressure in the tensile fracture interval and the lower maximum horizontal stress in Field 1 compared to Visund. A large number of inclined tensile fractures are also detected in well 2. The near-axial tensile fractures similarly tend to cover a larger portion of the well circumference, indicating that the well may not be perfectly aligned with the stress field. However, in each well the majority of tensile fractures are aligned with the axis of the well, indicating that the vertical and two horizontal stresses are principal stresses in this field. Appendix C discusses a method for using inclined tensile fractures to constrain the variability in the orientation of the stress tensor.

Figure 2 shows the mean orientation of the maximum horizontal stress in the three wells in Field 1. While the orientation of the stress field in well 3 is different from that in wells 1S and 2 the difference is still less than 10˚; which is within the accuracy of this type of data. Therefore, the stresses in Field 1 are consistent both laterally and with depth.

Table 1 summarizes the stress orientation and magnitude data measured in each of the three wells. Figure 8 shows a summary of the stress magnitude results. Minimum horizontal stress data are taken from both the field and nearby wells.

TABLE 1. Stress Tensor in Field 1

Well	Log	SH Azimuth	Quality	Depth (mTVD)	SH Mag. (MPa)	Sh Mag. (MPa)	Sv Mag. (MPa)
1S	FMS	79.1˚ ± 10.6˚	A	3450	92 + 11	67.6 ± 1	71.7
1S	FMS	79.1˚ ± 10.6˚	A	3550	101 + 10	70.4 ± 1	73.9
1S	FMS	79.1˚ ± 10.6˚	A	3650	106 + 9	73.3 ± 1	76.5
1S	FMS	79.1˚ ± 10.6˚	A	3750	109 + 9	76.2 ± 1	79.2
1S	FMS	79.1˚ ± 10.6˚	A	3850	109 + 8	79.2 ± 1	81.5
1SR	FMS	71.25˚	D	-	-	-	-
2	FMI	77.6˚ ± 16.8˚	A	3529	87 ± 4	67 ± 1	73.5
2	FMI	77.6 ˚± 16.8˚	A	3610	90 + 20	70 ± 1	75.4
2	FMI	77.6˚ ± 16.8˚	A	3727	94 + 20	72.5 ± 1	78.9
3	FMS	91.9˚ ± 40˚	B	3320	87.5 ± 8.5	58.6 ± 1	69
3	FMS	91.9˚ ± 40˚	B	3660	90 - 5	66.4 ± 1	77.1

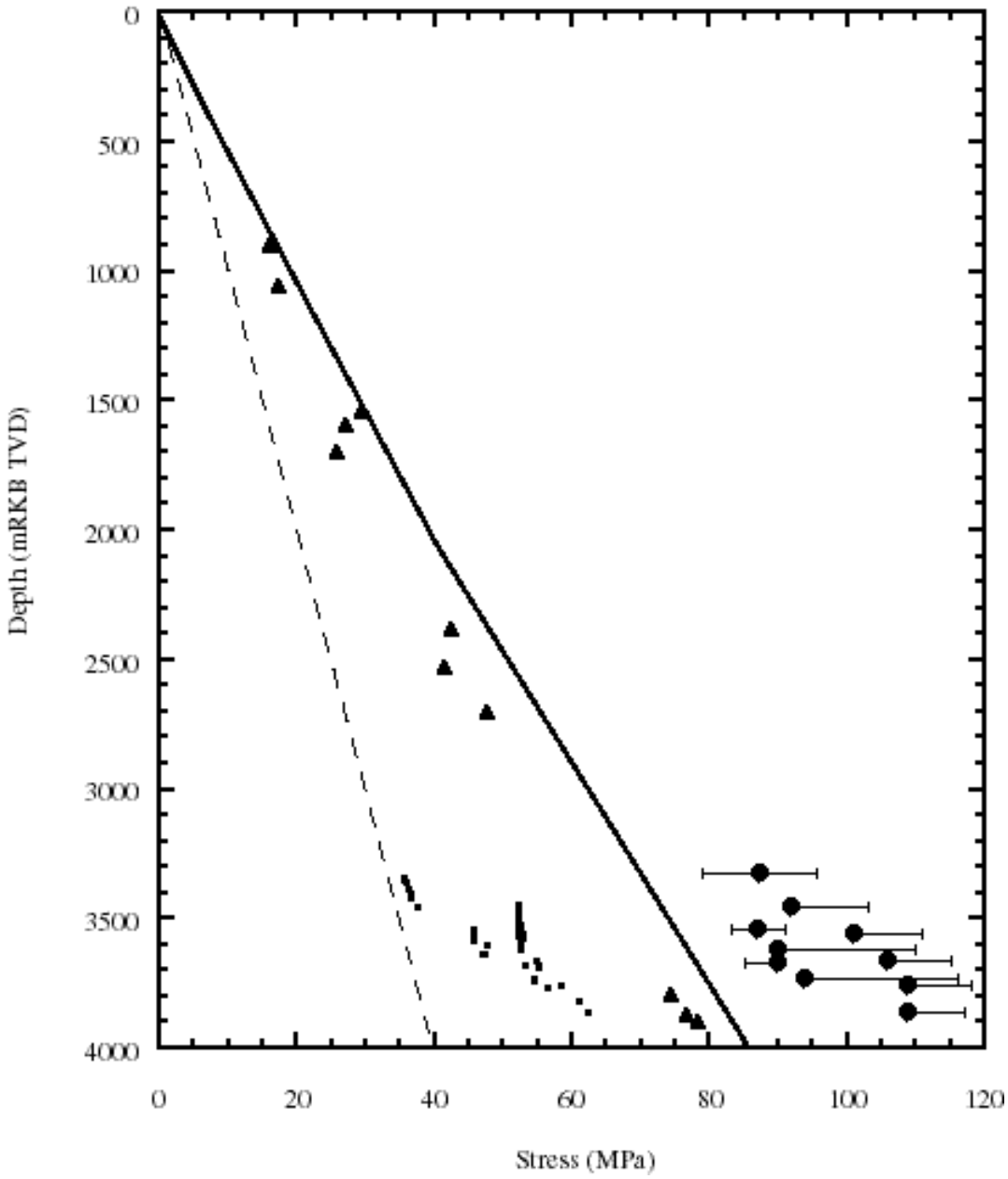

Figure 4.8: Stress vs. depth in Field 1. Hydrostatic pore pressure shown with dashed line. Pore pressure measurements shown with small squares. Minimum horizontal stress shown with triangles. Vertical stress shown with solid line. Maximum horizontal stress shown with circles. Depth is in meters relative to kelley bushing true vertical depth.

4.4 Field 2

4.4.1 Observations of wellbore failure

Figure 2 shows a map of Field 2. Formation MicroScanner and Formation MicroImager (FMS/FMI) logs were examined to determine whether drilling-induced tensile fractures could be seen in wells 3, 9, 10, 11, 11A, 16, and 18. Drilling-induced tensile fractures could only be detected in wells 3, 9, and 18. Examples of this type of data can be seen in Appendix B. The azimuth of the drilling-induced tensile fractures in wells 9 and 18 are plotted as a function of depth in Figure 9. Well 3 is treated separately because it is far north of Field 2. Black data points in Figure 9 represent tensile fractures that are aligned with the axis of the wellbore, and data points representing tensile fractures that are inclined with respect to the axis of the wellbore are shown in gray. Error bars for near-axial tensile fractures show the variation in azimuth of each fracture; while error bars for inclined tensile fractures show the portion of the wellbore circumference spanned by each fracture. Near the center of each plot, bit trips and "wash and ream" operations are shown by horizontal and vertical lines respectively. A bit trip is plotted each time the drill string is run into the hole. This operation may cause a significant rise in mud pressure at the bottom of the hole due to a piston effect. Washing and reaming the hole involves scraping the hole clean, and may remove evidence of drilling-induced tensile fractures. There is no visible correlation between the occurrence (or absence) of tensile fractures and these special drilling operations, suggesting that the tensile fractures formed (or did not form) during normal drilling operations, rather than as a result of extreme conditions in the well such as tripping the bit or reaming the hole.

Compared to analyses of drilling-induced tensile fractures in other wells, there are few tensile fractures in wells 9 and 18. These data, combined with the observation that there are no data in three of the wells analyzed in north of Field 2 indicate that the stress anisotropy is not high enough to cause tensile fractures to form in most cases. These observations are utilized below to place bounds on the maximum horizontal stress.

As in Field 1 and Visund, only the orientation of tensile fractures aligned with the wellbore axis will be considered in constraining the orientation of the maximum horizontal stress. The Mardia (1972) method is used to obtain the mean azimuth and standard deviation of the maximum horizontal stress (Figure 10). The uncertainty in the azimuth represents two standard deviations from the mean. The frequency is calculated by adding the tensile fractures in 0.2m intervals.

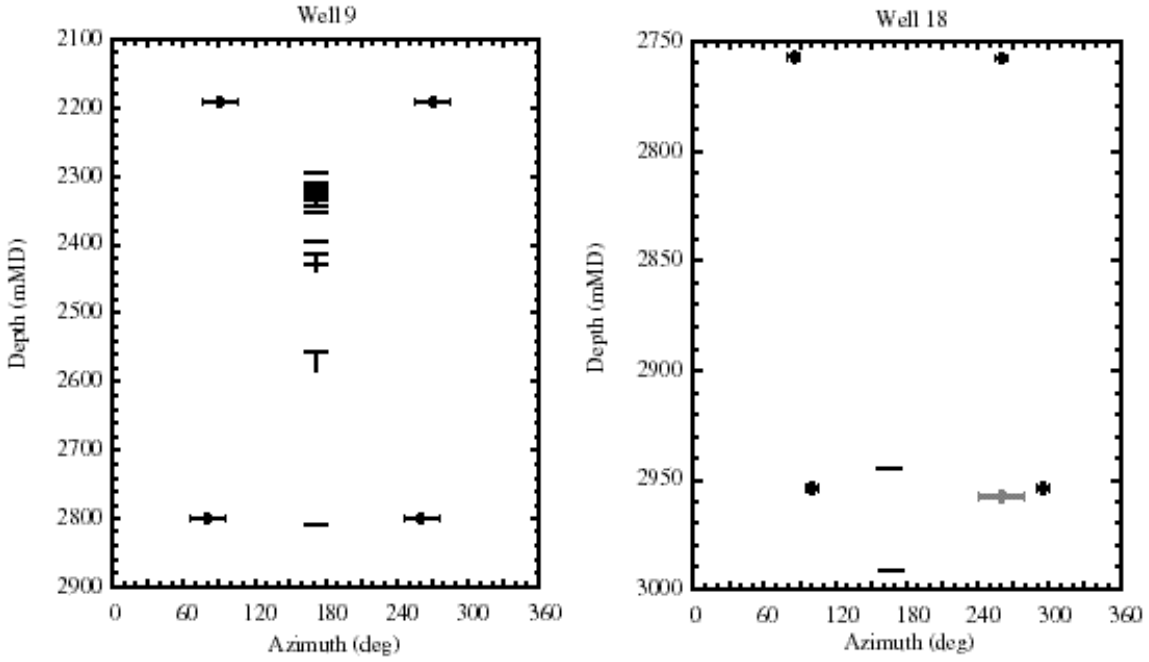

Figure 4.9: Azimuth (degrees from North) of drilling-induced tensile fractures as a function of depth (relative to drilling rig floor) measured along wellbore.

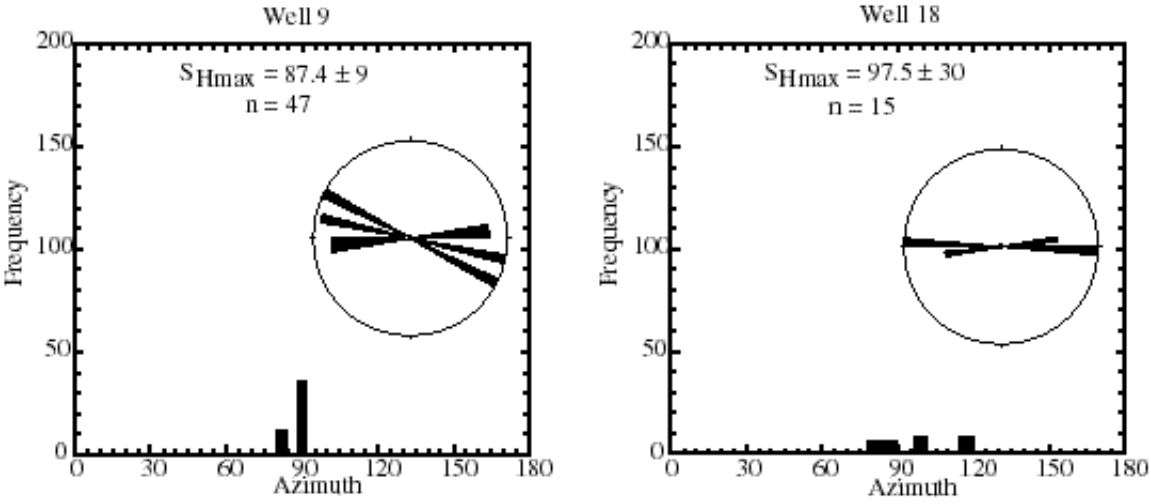

Figure 4.10: Histograms and rose diagrams showing orientation of maximum horizontal stress in Field 2. See Figure 4.4.

The analysis of drilling-induced tensile fractures in well 3 is shown in Figure 11. The data coverage is as sparse in this well as in wells 9 and 18. The orientation of the maximum horizontal stress in this well is consistent with the wells which penetrate the field.

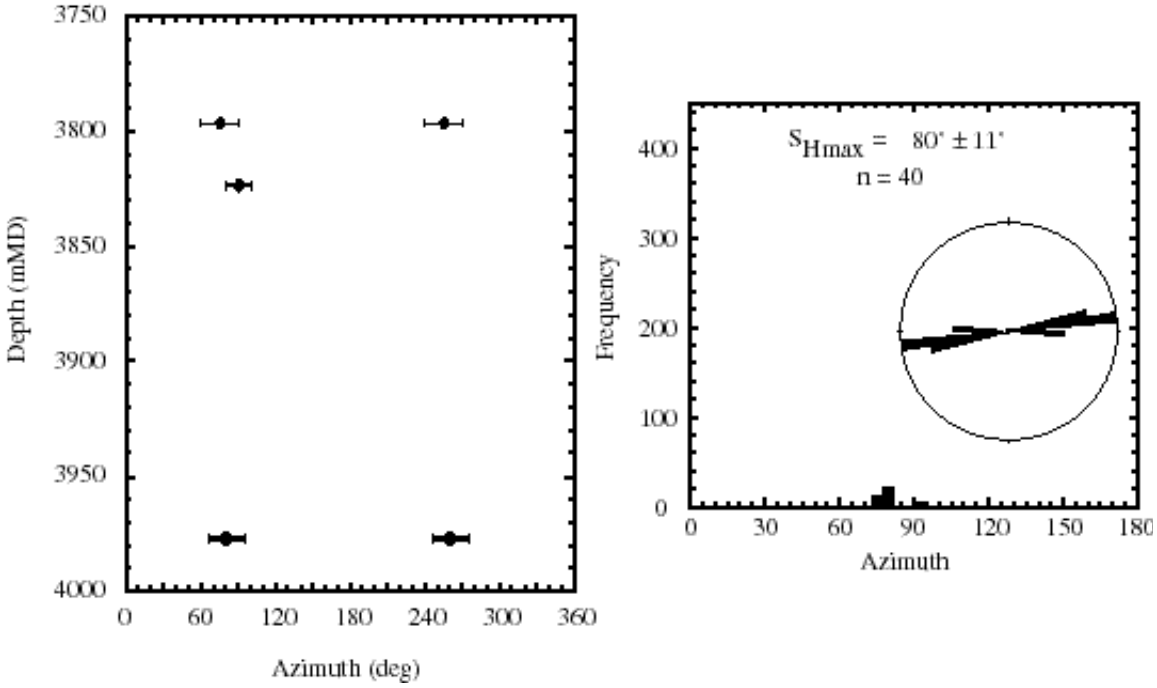

Figure 4.11: Azimuth of drilling-induced tensile fractures as a function of depth measured along wellbore (left) and histogram and rose diagram showing orientation of maximum horizontal stress (right) in well 3.

4.4.2 In situ stress and rock strength

As in Field 1, we utilize SFIB to constrain the maximum horizontal stress magnitudes and to put limits on rock strength. All of the stresses were constrained in the same manner as in Field 1, and a more complete discussion of the process can be seen above. Figures 12, 13 and 14 show the analysis for the maximum horizontal stress, S_{Hmax} in wells 9, 18 and 3 respectively.

Constraining S_{Hmax} in well 9

At 2800 mTVD the minimum horizontal stress was determined to be 49 MPa (Figure 12). Assuming a ±1 MPa error in this estimate provides the upper and lower bounds for both the minimum and maximum horizontal stresses. The lower bound of the minimum horizontal stress gives an estimate of the lower bound of the maximum horizontal stress of 77 MPa. The upper bound of the maximum horizontal stress is constrained by the tensile failure contour as well. Since so few tensile fractures were detected in this field, and many wells had no evidence of any tensile fractures, we assume the stress state must be close to the tensile failure contour. We use this observation in all of the wells in this field. The upper bound of the maximum horizontal stress in this case is 83 MPa. There are no rock strength

measurements in this well, and no caliper data was available so we cannot estimate the rock strength at this depth. The best estimate of the maximum horizontal stress at this depth is determined by taking the mean of the upper an lower bounds (80 MPa).

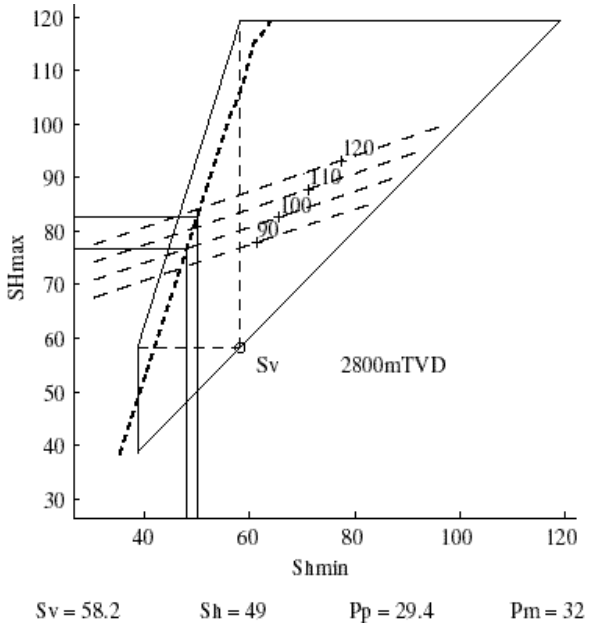

Figure 4.12: Stress polygon showing constrained values of maximum horizontal stress in well 9. See figure 4.5 for explanation.

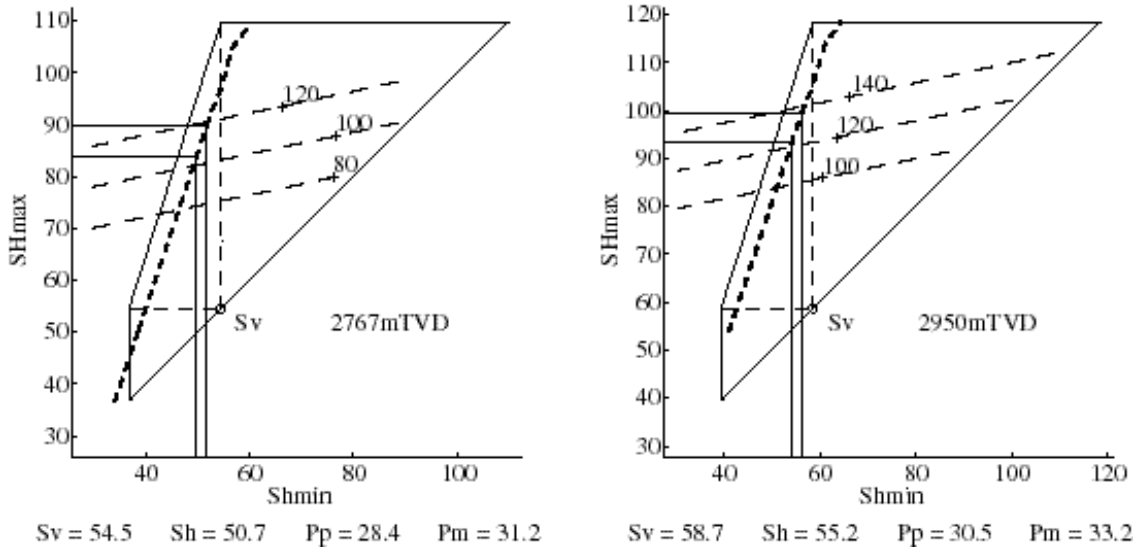

Figure 4.13: Stress polygons showing constrained values of maximum horizontal stress in well 18. See figure 4.5 for explanation.

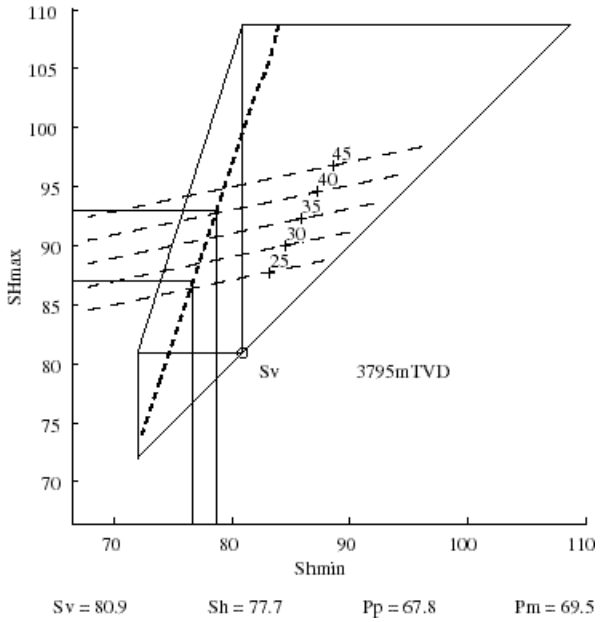

Figure 4.14: Stress polygon showing constrained values of maximum horizontal stress in well 3. See figure 4.5 for explanation.

Constraining S_{Hmax} in well 18

At 2767 mTVD the minimum horizontal stress was determined to be 50.7 MPa (Figure 13). The lower bound of the maximum horizontal stress is 84 MPa. The upper bound of the maximum horizontal stress is 90 MPa. The rock strength from lab measurements is between 30 and 45 MPa. A possible breakout can be seen from the single arm caliper log in this well. The observations of compressive wellbore failure are consistent with the stress state determined from modeling the drilling-induced tensile fractures. The best estimate of the maximum horizontal stress at this depth is determined by taking the mean of the upper and lower bounds (87 MPa).

At 2950 mTVD the minimum horizontal stress was determined to be 55.2 MPa. The lower bound of the maximum horizontal stress is 93 MPa, and the upper bound is 99 MPa. A possible breakout can be seen from the single arm caliper log, but there are no rock strength measurements. The analysis of drilling-induced tensile fractures suggests the rock strength must be less than approximately 120 MPa. The best estimate of the maximum horizontal stress at this depth is determined by taking the mean of the upper and lower bounds (96 MPa).

Constraining S_{Hmax} in well 3

At 3795 mTVD the minimum horizontal stress was determined to be 77.7 MPa (Figure 14). The lower bound of the maximum horizontal stress is 84 MPa and the upper bound is

96 MPa. Severe washouts or breakouts are evident from the single arm caliper log. Sections of this hole are twice the bit size in some places. There are no rock strength measurements in this well. This analysis suggests the rock strength may be as low as 27 MPa or as high as 40 MPa. This is approximately the same rock strength observed in well 18 at a much shallower depth (2767 mTVD). The best estimate of the maximum horizontal stress at this depth is determined by taking the mean of the upper and lower bounds (90 MPa).

4.4.3 Field 2 Summary

The mean orientation of the maximum horizontal stress in wells 8 and 18 can be seen in map view in Figure 2. Well 3 is not included in this figure as it is well beyond the map area. Table 2 summarizes the stress orientation and magnitude data measured in each of the three wells. Figure 15 shows a summary of the stress magnitude results. Minimum horizontal stress data are taken from both the field and nearby wells.

TABLE 2. Stress Tensor in Field 2

Well	Log	SH Azimuth	Quality	Depth (mTVD)	SH Mag. (MPa)	Sh Mag. (MPa)	Sv Mag. (MPa)
3	FMS	80 ˚± 11˚	C	3795	90 ± 6	77.7 ± 1.5	80.9
9	FMS	87.4˚ ± 9˚	D	2800	80 ± 3	49 ± 1	58.2
10	FMS	-	-	-	-	-	-
11	FMS	-	-	-	-	-	-
11A	FMS	-	-	-	-	-	-
16	FMI	-	-	-	-	-	-
18	FMS	97.5˚ ± 18˚	D	2767	87 ± 3	50.7 ± 1	54.5
18	FMS	97.5˚ ± 18˚	D	2950	96 ± 3	55.2 ± 1	58.7

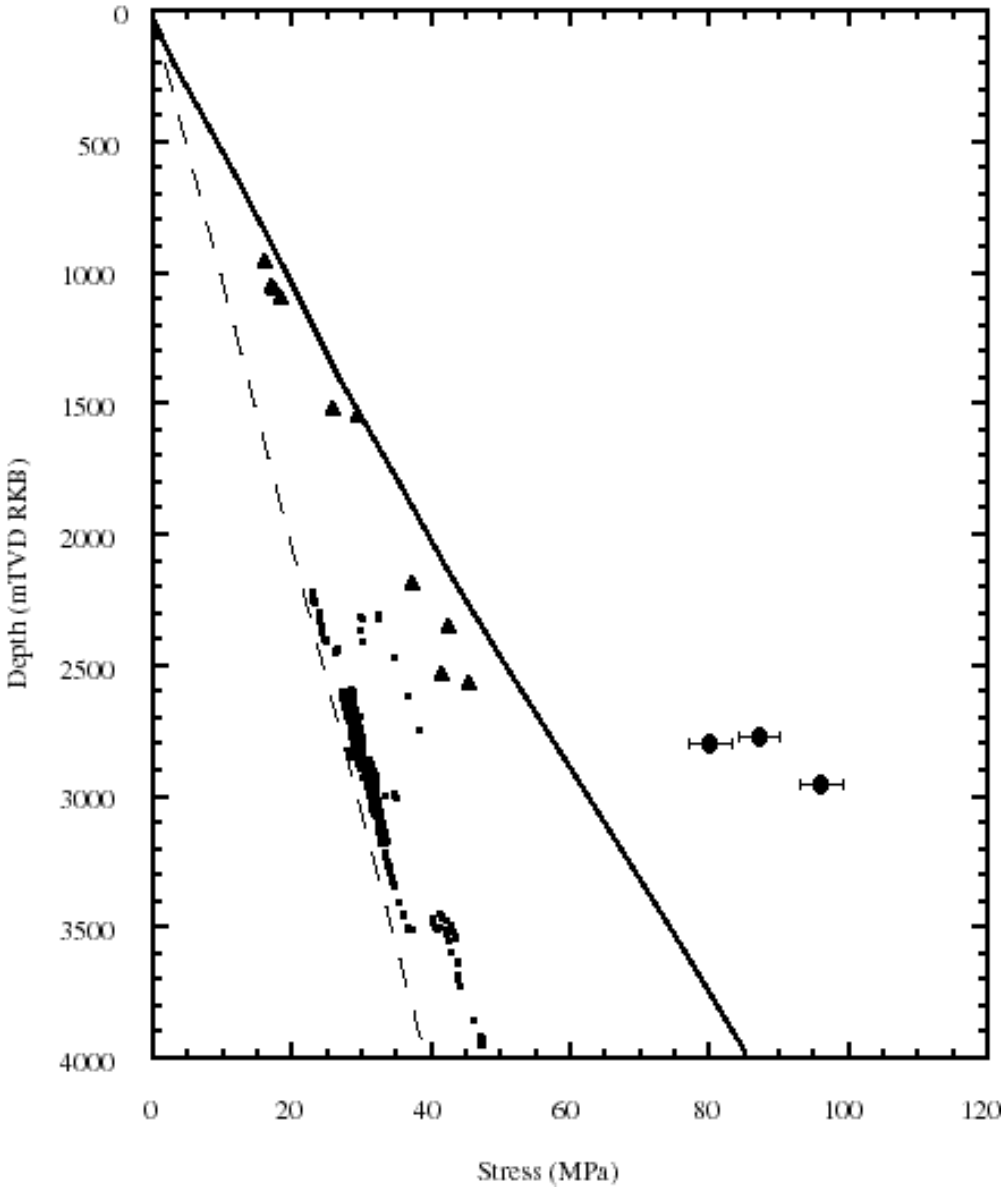

Figure 4.15: Stress vs. depth in Field 2. Hydrostatic pore pressure shown with dashed line. Pore pressure measurements shown with small squares. Minimum horizontal stress shown with triangles. Vertical stress shown with solid line. Maximum horizontal stress shown with circles. Depth is in meters relative to kelley bushing true vertical depth.

4.5 Field 3

4.5.1 Observations of wellbore failure

Figure 16 shows a map of Field 3. Formation MicroScanner and Formation MicroImager (FMS/FMI) logs were examined to determine whether drilling-induced

tensile fractures could be seen in wells 2, 5, 8S, 9, 10, and 10A. Drilling-induced tensile fractures were detected in all of the wells. Examples of this type of data can be seen in Appendix B. The azimuth of the drilling-induced tensile fractures in all wells except well 2 are shown in Figure 17. Well 2 is treated separately because it is far north of the main portion of Field 3. The azimuth of drilling-induced tensile fractures in well 2 is shown in Figure 18. In both figures, black data points represent tensile fractures that are aligned with the axis of the wellbore, and data points representing tensile fractures that are inclined with respect to the axis of the wellbore are shown in gray. Error bars for near-axial tensile fractures show the variation in azimuth of each fracture; while error bars for inclined tensile fractures show the portion of the wellbore circumference spanned by each fracture. Near the center of each plot, bit trips and "wash and ream" operations are shown by horizontal and vertical lines respectively.

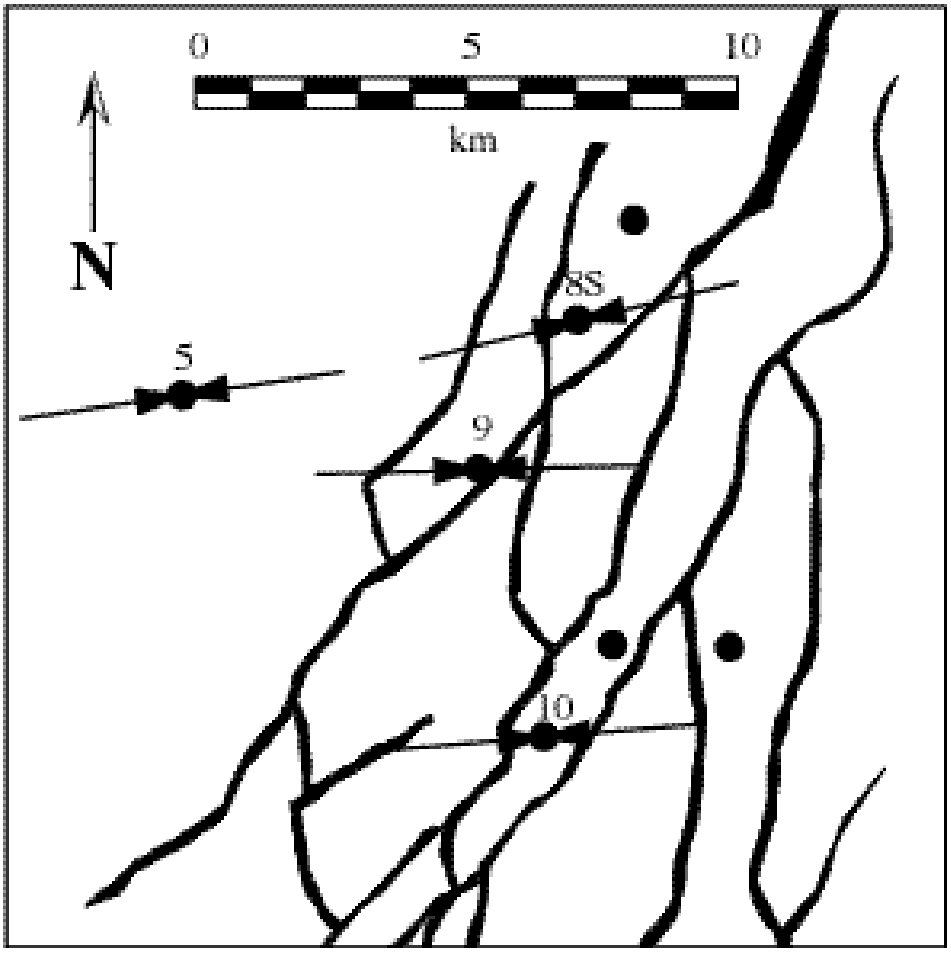

Figure 4.16: Generalized map of Field 3 showing orientation of the maximum horizontal stress (inward pointed arrows), exploration wells (circles), and major faults.

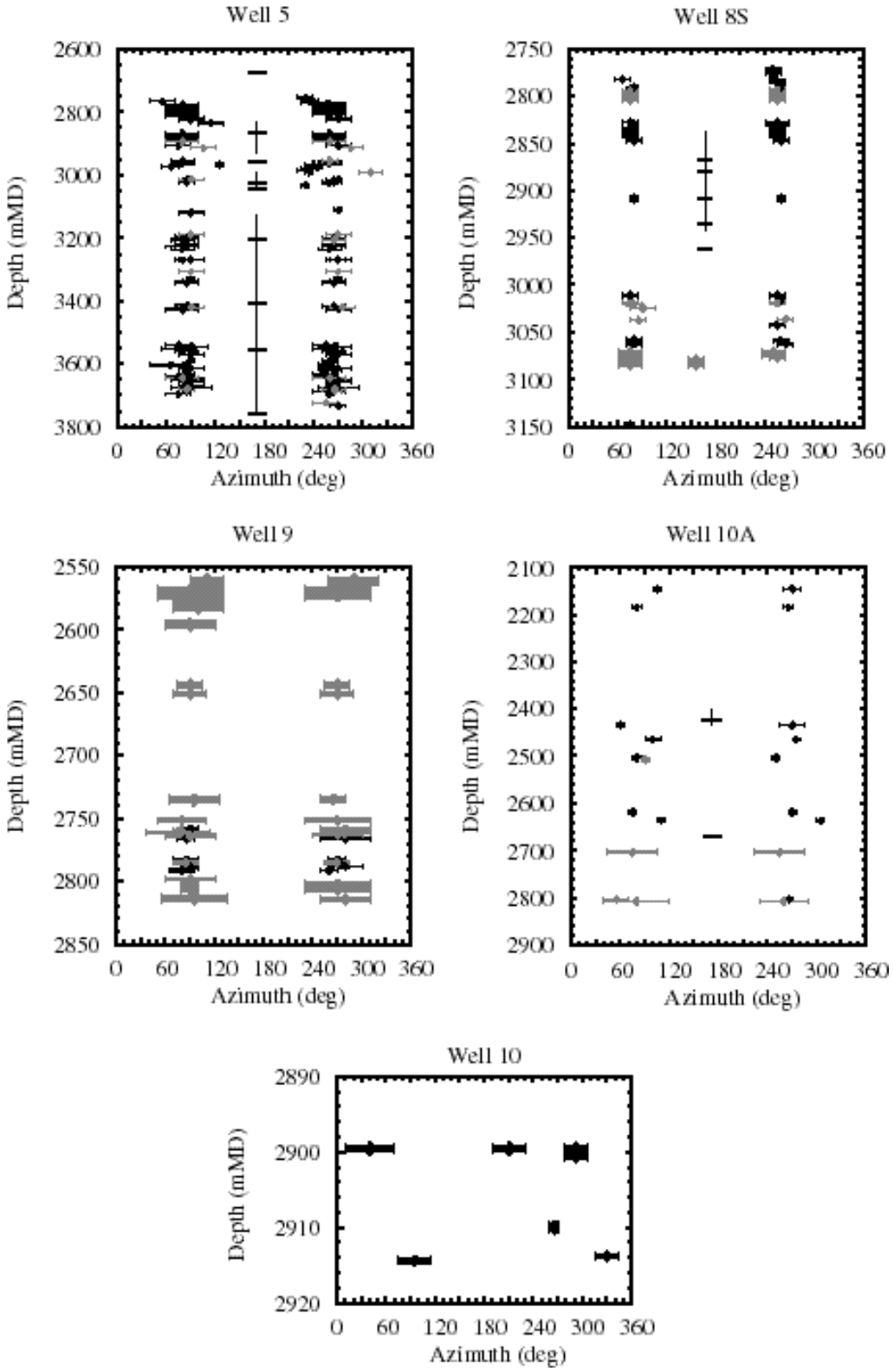

Figure 4.17: Azimuth (degrees from North) of drilling-induced tensile fractures as a function of depth (relative to drilling rig floor) measured along wellbore.

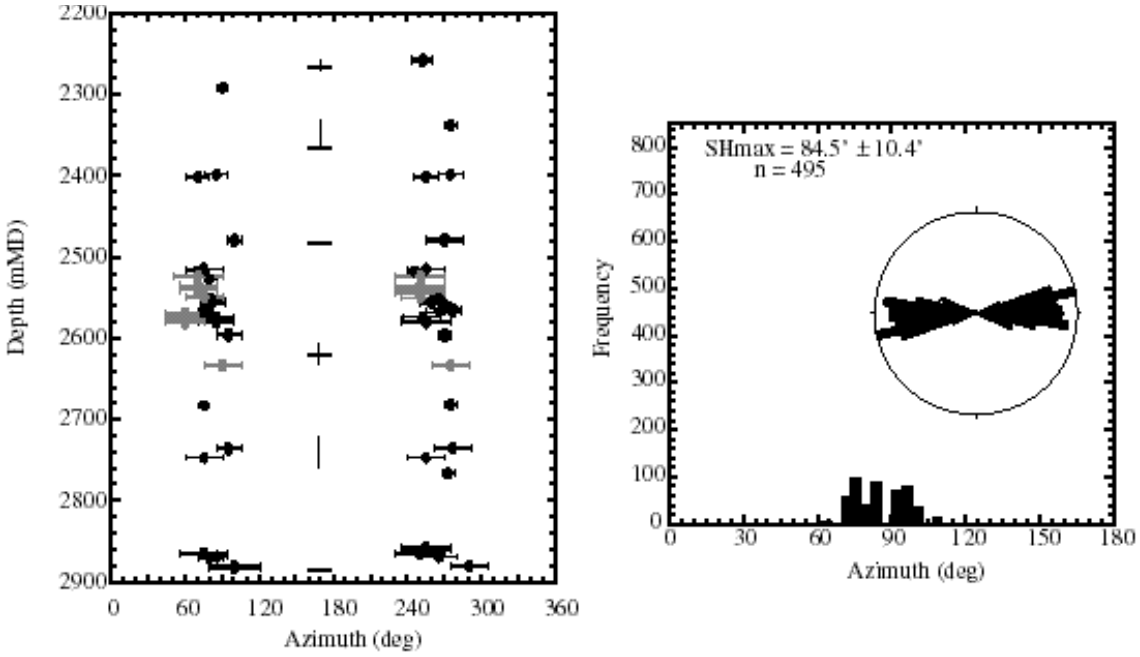

Figure 4.18: Azimuth of drilling-induced tensile fractures as a function of depth measured along wellbore (left) and histogram and rose diagram showing orientation of maximum horizontal stress (right) in well 2.

To determine the orientation of the stress field in this region, the orientation of tensile fractures both aligned and inclined with respect to the wellbore axis will be considered. While the data in well 9 are not as consistent as the other wells, they still provide an orientation of the maximum horizontal stress that is similar to data from the rest of the field. A circular statistical method developed by Mardia (1972) is used to obtain the mean azimuth and standard deviation of the maximum horizontal stress for each well (Figures 18, 19). Well 10 has too little data to claim the tensile fractures are representative of the tectonic stress field. Well 9 has more inclined tensile fractures than the other wells in Field 3. A final well report was not obtained for this well. The analysis of bit trips, washing and reaming, and interaction of this well with the nearby fault was therefore impossible. While the fault may be responsible for the inclined tensile fractures, there are no data available to support this assertion. The orientation of the stress tensor in well 2 is consistent with the mean orientation of the maximum horizontal stress in the four wells to the south.

4.5.2 In situ stress and rock strength

As in Field 1 and Field 2, we utilize SFIB to constrain the maximum horizontal stress magnitudes and to put limits on rock strength. All of the stresses were constrained in the same manner as in Field 1 and Field 2, and a more complete discussion of the process can

be seen in the section on the Field 1. Figures 20, 21, 22, and 23 show the analysis for the maximum horizontal stress, S_{Hmax}, in wells 5, 8S, 10, 10A, and 2 respectively. A stress analysis of well 9 is not conducted since no other data aside from the FMS log was available for this well.

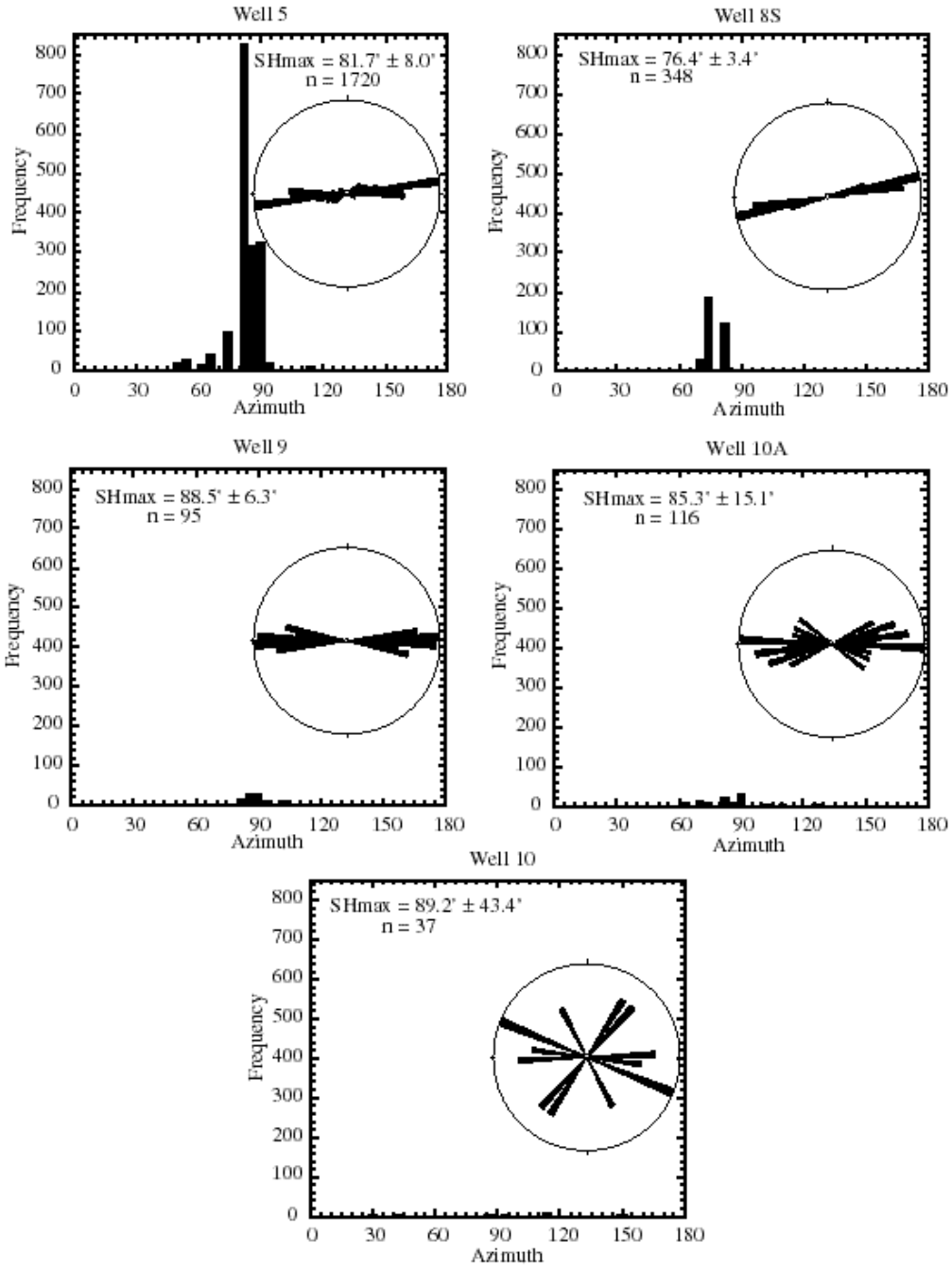

Figure 4.19: Histograms and rose diagrams showing orientation of maximum horizontal stress in Field 3. See Figure 4.4.

Constraining SHmax in well 5

At 2900 mTVD the minimum horizontal stress was determined to be 50.5 MPa (Figure 20). The lower bound of the minimum horizontal stress gives an estimate of the lower bound of the maximum horizontal stress of 70 MPa. The upper bound of the maximum horizontal stress is constrained by the tensile and compressive failure lines. The rock strength measured in the lab was between 10 and 15 MPa at this depth and no breakouts were observed. Therefore, the upper bound of the stress must be such that it lies above the tensile failure line and below the 15 MPa compressive failure line. The point where the tensile failure line meets the 15 MPa compressive failure line defines the highest possible stress state where these two conditions are met. This point defines the upper bounds of both the minimum and maximum horizontal stresses. The upper bound of the minimum horizontal stress is 50.5 MPa and the upper bound of the maximum horizontal stress is 72 MPa. The best estimate of the maximum horizontal stress at this depth is determined by taking the mean of the upper and lower bounds (71 MPa).

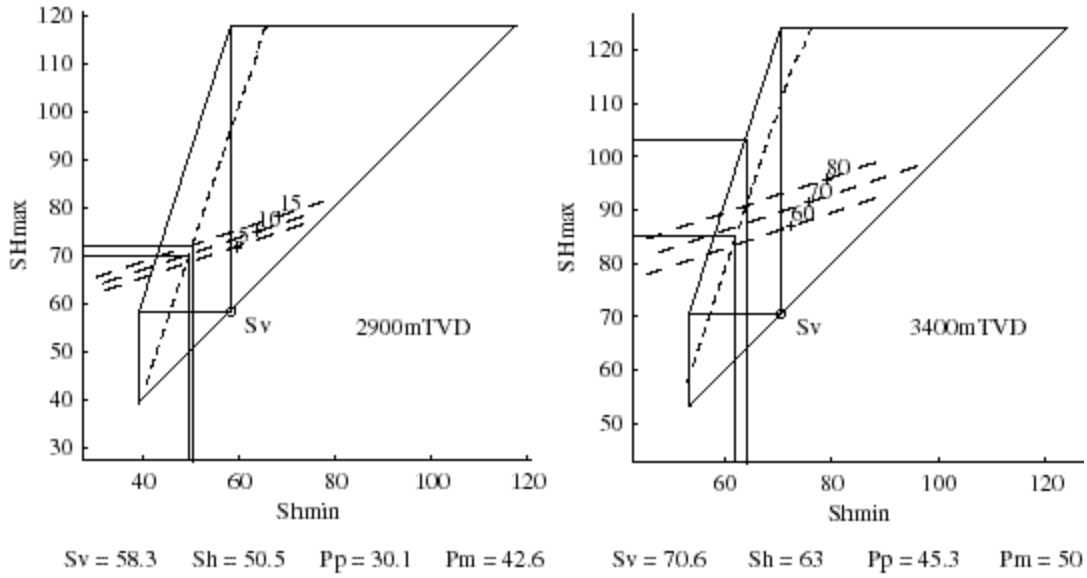

Figure 4.20: Stress polygon showing constrained values of maximum horizontal stress in well 5. See figure 4.5 for explanation.

At 3400 mTVD the minimum horizontal stress was determined to be 63 MPa. The lower bound of the maximum horizontal stress is 85 MPa, and the upper bound from the stress polygon is 103 MPa. In this case no breakout could be seen in the image log or the single arm caliper log. No rock strength measurements were available at this depth. The lower bound of the maximum horizontal stress suggests the rock strength is greater than 65 MPa at this depth. The best estimate of the maximum horizontal stress at this depth is given by lower bound (85 MPa).

Constraining S_{Hmax} in well 8S

At 2780 mTVD the minimum horizontal stress was determined to be 47.7 MPa (Figure 21). The lower bound of the maximum horizontal stress is 71 MPa, and the upper bound from the stress polygon is 92 MPa. No breakouts were observed at this depth and no rock strength measurements were conducted in this well. However, the rock strength in a nearby well is 15 MPa at this depth. This observation is not consistent with the stress state estimated in this well. The rock strength at this depth according to our analysis should be at least 45 MPa. We have no other data that might clarify the stress analysis in this well. The best estimate of the maximum horizontal stress at this depth is given by lower bound (71 MPa).

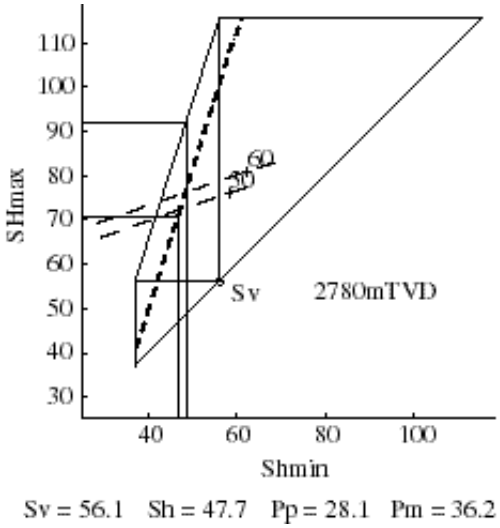

Figure 4.21: Stress polygon showing constrained values of maximum horizontal stress in well 8S. See figure 3.5 for explanation.

Constraining S_{Hmax} in well 10

At 2900 mTVD the minimum horizontal stress was determined to be 51 MPa (Figure 22). The lower bound of the maximum horizontal stress is 79 MPa, and the upper bound from the stress polygon is 100 MPa. In this case no breakout could be seen in the image log or the single arm caliper log. No rock strength measurements were available at this depth. The lower bound of the maximum horizontal stress suggests the rock strength is greater than 80 MPa at this depth. The best estimate of the maximum horizontal stress at this depth is given by lower bound (79 MPa).

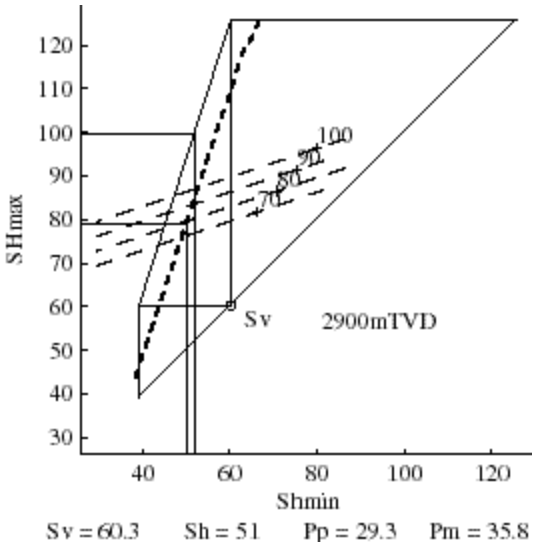

Figure 4.22: Stress polygon showing constrained values of maximum horizontal stress in well 10. See figure 4.5 for explanation.

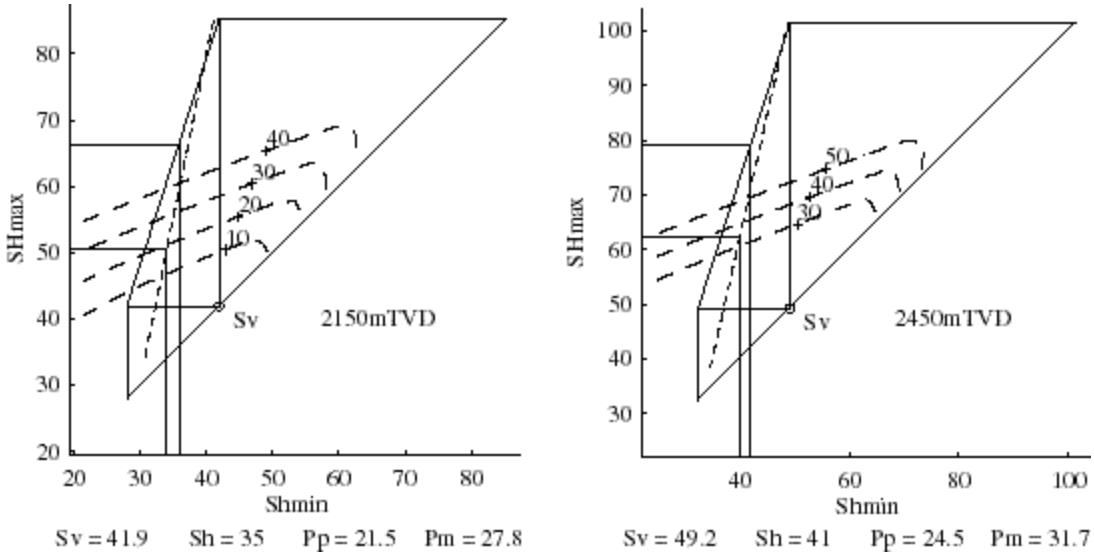

Figure 4.23: Stress polygon showing constrained values of maximum horizontal stress in well 10A. See figure 4.5 for explanation.

Constraining S_{Hmax} in well 10A

At 2150 mTVD the minimum horizontal stress was determined to be 35 MPa (Figure 23). The lower bound of the maximum horizontal stress is 51 MPa, and the upper bound from the stress polygon is 67 MPa. In this case no breakout could be seen in the image log or the single arm caliper log. No rock strength measurements were available at this depth. The lower bound of the maximum horizontal stress suggests the rock strength is greater

than 20 MPa at this depth. The best estimate of the maximum horizontal stress at this depth is given by lower bound (51 MPa).

At 2450 mTVD the minimum horizontal stress was determined to be 41 MPa. The lower bound of the maximum horizontal stress is 62 MPa, and the upper bound from the stress polygon is 79 MPa. In this case no breakout could be seen in the image log or the single arm caliper log. No rock strength measurements were available at this depth. The lower bound of the maximum horizontal stress suggests the rock strength is greater than 35 MPa at this depth. The best estimate of the maximum horizontal stress at this depth is given by lower bound (62 MPa).

Constraining S_{Hmax} in well 2

At 2400 mTVD the minimum horizontal stress was determined to be 37.2 MPa (Figure 24). The lower bound of the maximum horizontal stress is 50 MPa. No caliper data was available for this well so the upper bound of the maximum horizontal stress must be constrained by the stress polygon. The upper bound of the maximum horizontal stress is 68 MPa. The best estimate of the maximum horizontal stress at this depth is given by the lower bound of the maximum horizontal stress (50 MPa).

At 2510 mTVD the minimum horizontal stress was determined to be 39.2 MPa. The lower bound of the maximum horizontal stress is 53 MPa and the upper bound is 71 MPa. The best estimate of the maximum horizontal stress at this depth is given by the lower bound (53 MPa).

At 2695 mTVD the minimum horizontal stress was determined to be 42 MPa. The lower bound of the maximum horizontal stress is 58 MPa and the upper bound is 77 MPa. The best estimate of the maximum horizontal stress at this depth is given by the lower bound (58 MPa).

4.5.3 Field 3 Summary

Figure 16 shows the mean orientation of the maximum horizontal stress in the four wells with good data in Field 3. Table 3 summarizes the stress data found in each of the wells. Note that the values of the maximum horizontal stresses in well 2 are significantly lower than those found in the Field 3 to the south. Figure 25 shows a summary of the stress results. Minimum horizontal stress data are taken from both the field and nearby wells.

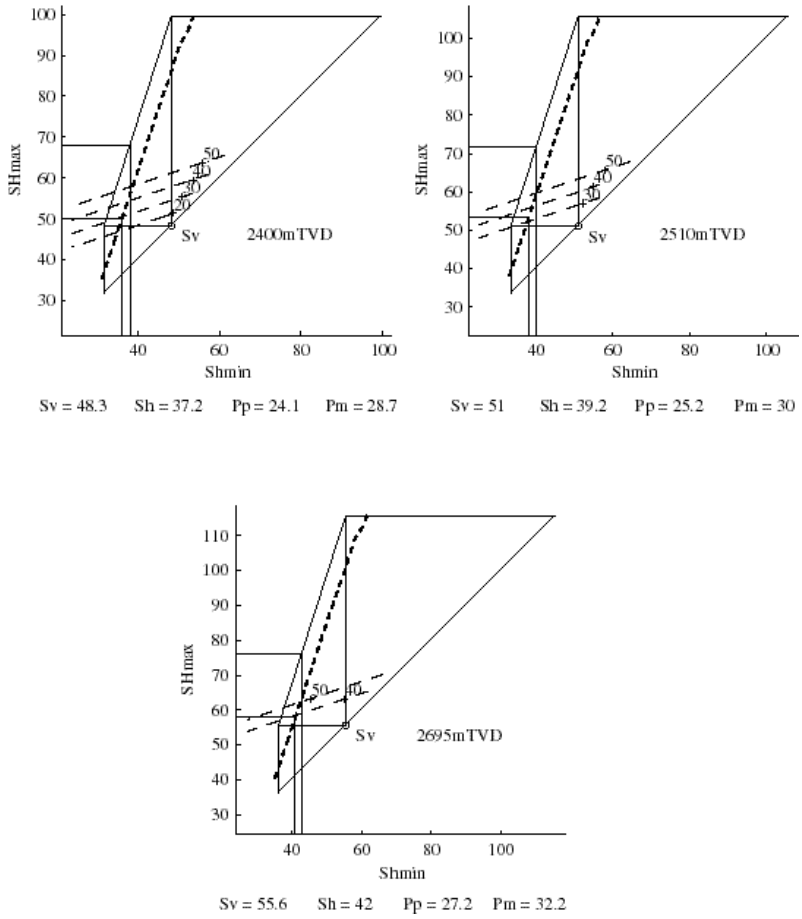

Figure 4.24: Stress polygon showing constrained values of maximum horizontal stress in well 2. See figure 4.5 for explanation.

TABLE 3. Stress Tensor in Field 3

Well	Log	SH Azimuth	Quality	Depth (mTVD)	SH Mag. (MPa)	Sh Mag. (MPa)	Sv Mag. (MPa)
2	FMS	84.5˚ ± 10.4˚	A	2400	50 + 18	37.2 ± 1	48.3
2	FMS	84.5 ˚± 10.4˚	A	2510	53 + 18	39.2 ± 1	51
2	FMS	84.5˚ ± 10.4˚	A	2695	58 + 19	42 ± 1	55.6
5	FMS	81.7˚ ± 8˚	A	2900	71 ± 1	50.5 - 1	58.3
5	FMS	81.7˚ ± 8˚	A	3400	85 + 18	63 ± 1	70.6
8S	FMS	76.4˚ ± 3.4˚	A	2780	71 + 21	47.7 ± 1	56.1
9	FMI	88.5˚ ± 6.3˚	A	-	-	-	-
10	FMS	89.2˚ ± 43˚	D	2900	79 + 21	51 ± 1	60.3
10A	FMI	85.3˚ ± 15˚	A	2150	51 + 16	35 ± 1	41.9
10A	FMI	85.3˚ ± 15˚	A	2450	62 + 17	41 ± 1	49.2

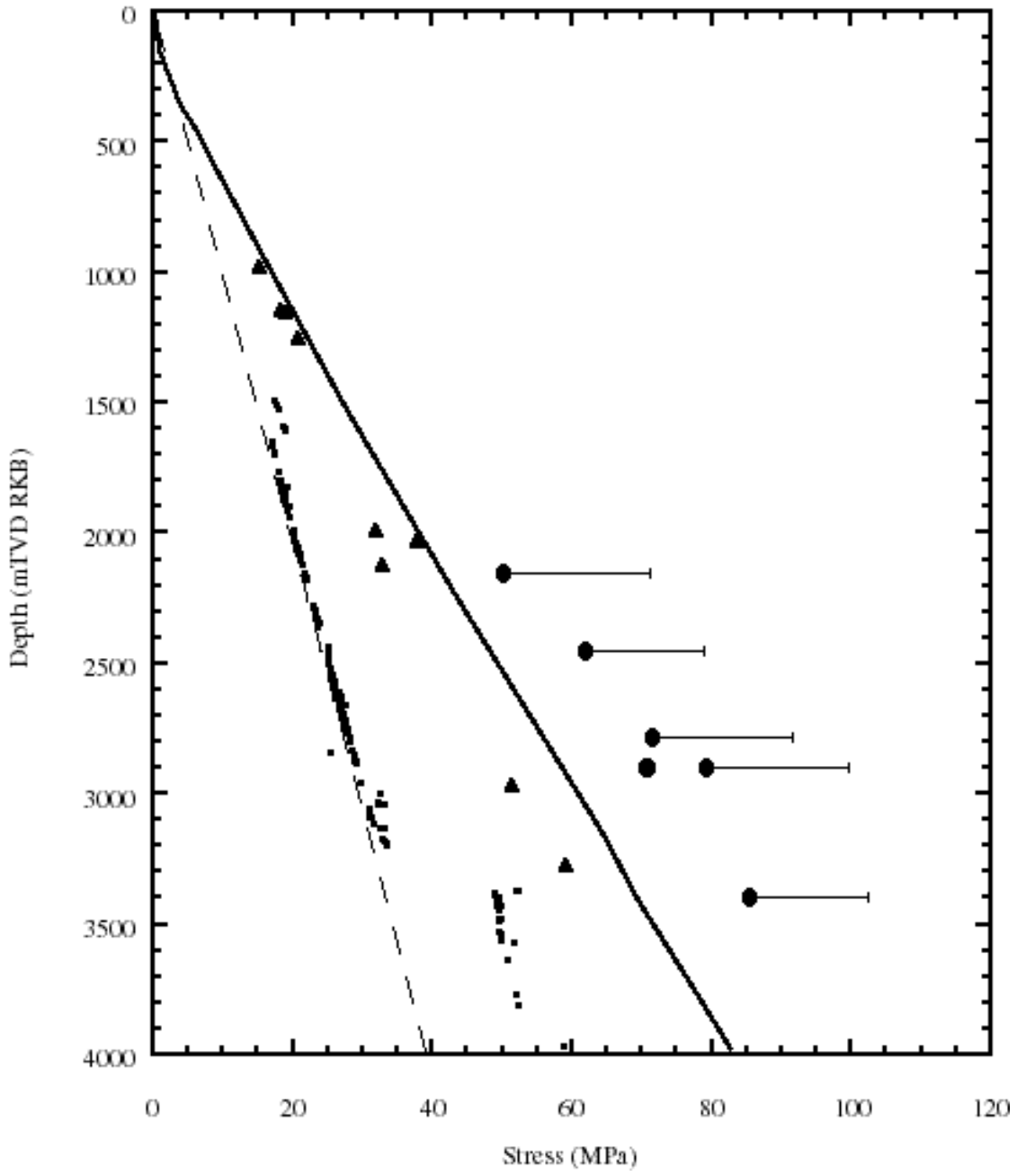

Figure 4.25: Stress vs. depth in Field 3. Hydrostatic pore pressure shown with dashed line. Pore pressure measurements shown with small squares. Minimum horizontal stress shown with triangles. Vertical stress shown with solid line. Maximum horizontal stress shown with circles. Depth is in meters relative to kelley bushing true vertical depth. Data from well 2 are not shown on this plot because well is too far from main field.

4.6 Summary

The orientation and magnitude of the maximum horizontal stress in Field 1, Field 2, and Field 3 has been constrained using drilling-induced tensile fractures, and in some cases breakouts. Most wells yield a consistent orientation of the maximum horizontal stress. Those wells that do not show a consistently oriented direction of maximum horizontal stress either have too little data to confidently constrain the orientation of the stress tensor, or the stress field is perturbed by a nearby fault. The three principal stresses (S_v, S_{hmin}, and S_{Hmax}) are consistent with depth and reflect a strike-slip to reverse faulting stress regime. The maximum horizontal stress is shown to be higher than the vertical and minimum horizontal stresses in all three fields. In general, the maximum horizontal stress orientations rotate from an orientation of approximately 100˚ in the Visund field (Chapter 2) to approximately 90˚ in Field 1 and Field 2, and 80˚ in Field 3. The maximum horizontal stress magnitudes in Visund are slightly higher than the stress magnitudes in Field 1 and Field 2; and those magnitudes are in turn higher than in Field 3, as predicted from finite element modeling of glacial rebound in the northern North Sea by Grollimund and Zoback (2000).

CHAPTER 5

LEAKAGE POTENTIAL ALONG RESERVOIR-BOUNDING FAULTS AND IMPLICATIONS FOR HYDROCARBON COLUMN HEIGHT IN THE NORTHERN NORTH SEA

5.1 Abstract

The question of how faults affect the migration of fluid in petroleum reservoirs is complicated as some faults contribute dramatically to formation permeability, yet others provide effective barriers to fluid flow and separate distinct reservoir pressure compartments. To investigate this question further, we evaluated the state of stress and pore pressure acting on the major faults in four oil and gas fields in the northern North Sea. Many of the faults bound hydrocarbon reservoirs. Our goal is to test the hypothesis that faults that are critically-stressed in the current stress field (i.e., capable of slipping) are permeable (and thus tend to leak), whereas those that are not critically-stressed are more likely to be sealing. An important aspect of this study is to utilize a detailed analysis of the magnitude and orientation of all three principal stresses in a number of wells in each field. These data, along with information on pore pressure, allowed us to resolve the shear and effective normal stress acting on distinct ~100 m x 100 m elements of individual fault planes. By comparing the stress state resolved on each fault element to expected stress at failure (using the concept of the Coulomb Failure Function) we have created color-shaded maps showing the proximity to fault slip (and hence leakage) along each fault. Fault reactivation and hydrocarbon leakage in this area appears to be caused by three factors: (1) a recent increase in the compressional stress associated with postglacial rebound, (2) locally elevated pore pressure, in part due to the presence of natural gas in some hydrocarbon reservoirs abutting faults, and (3) fault orientations that are nearly optimally-oriented for frictional slip in the present-day stress field. We demonstrate that the combination of these three factors may have recently induced fault slippage and gas leakage along sections of previously sealing reservoir-bounding faults in some fields, whereas in others, the stress and pore pressure are not sufficient to cause fault reactivation. We show that only in cases where reservoir-bounding faults are not potentially active, the pore pressure difference across faults can become quite high. Hence, the leakage potential (or dynamic capacity) of reservoir-bounding faults seems to control the potential hydrocarbon column heights in each field.

5.2 Introduction

The question of how faults affect the migration of fluid in petroleum reservoirs is complicated, as faults are known to act as both barriers and conduits. Some faults contribute dramatically to formation permeability (Dholakia, et al., 1998) and allow hydrocarbon migration between different reservoir units (Finkbeiner et al., 2001), yet others provide effective barriers separating distinct reservoir compartments (Hunt, 1990).

In this paper we consider the effect of fault reactivation on fluid flow at a field-wide scale in the northern North Sea in the context of in situ stress and pore pressure. We test the hypothesis that faults which are critically stressed in the current stress field (i.e., capable of slipping) are permeable, whereas those that are not critically stressed are not permeable. A number of permeability studies in fractured and faulted crystalline rock appear to confirm this hypothesis (Sibson, 1981; Barton et al., 1995, 1998; Hickman et al., 1998). Studies in hydrocarbon reservoirs in sedimentary basins in the Gulf of Mexico (Finkbeiner et al., 2001) and on a single fault in the northern North Sea (Wiprut and Zoback, 2000) also appear to confirm that critically stressed faults are responsible for promoting hydrocarbon leakage and migration.

In this study we expand on the work presented by Wiprut and Zoback (2000) in the Visund field. The point of departure of this work from our previous work is that we include greater detail about leakage from the A-Central fault as well as addressing leakage potential on major seismically-detected faults throughout Visund, Field 1, Field 2, and Field 3 in the northern North Sea. Figure 1 shows a map of the northern North Sea. A rough outline of the Viking graben is shown by the hatchered area. We focus here specifically on the influence of buoyant gas columns in hydrocarbon reservoirs on the sealing capacity of reservoir-bounding faults. We further address the effect of critically stressed faults and water-phase pore pressure on the potential height of hydrocarbon columns. Finkbeiner et al. (2001) showed that only small amounts of hydrocarbon could be trapped against reservoir-bounding faults near frictional failure, whereas larger columns could be trapped against faults of different orientation, or with lower water-phase pore pressures, initially further from failure.

5.3 Determining Fault Reactivation, Leakage Potential, and Column Height

Figure 2 shows conceptually how we apply the hypothesis that buoyant hydrocarbons can increase the pore pressure and trigger fault reactivation. As gas accumulates in a permeable reservoir bounded by a sealing fault, the pore pressure at the fault-reservoir interface increases because the pore-pressure gradient in the gas is considerably less than the hydrostatic gradient owing to the extremely low density of gas. As the height of the gas column increases, at some point the pore pressure will be sufficient to induce fault slip, providing a mechanism to increase fault permeability and allow leakage from the reservoir.

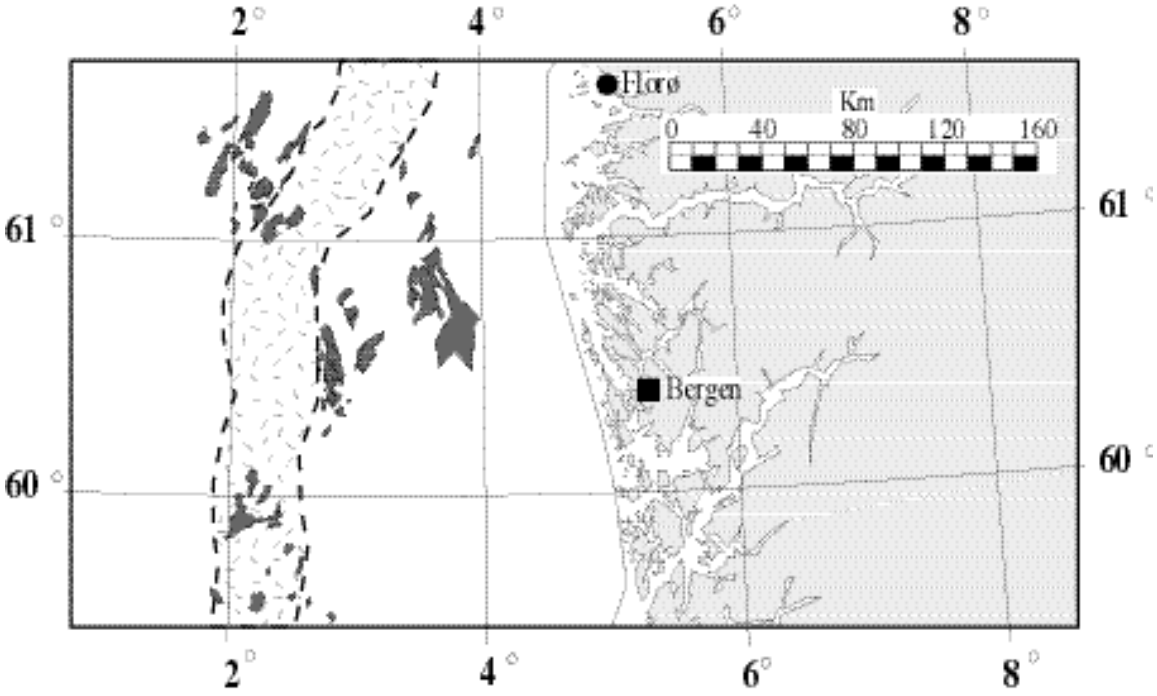

Figure 5.1: Map of northern North Sea showing the west coast of Norway and major offshore oil and gas discoveries. A rough outline of the Viking graben is indicated by the hatchered area. Map modified from Norwegian Petroleum Directorate, 1997.

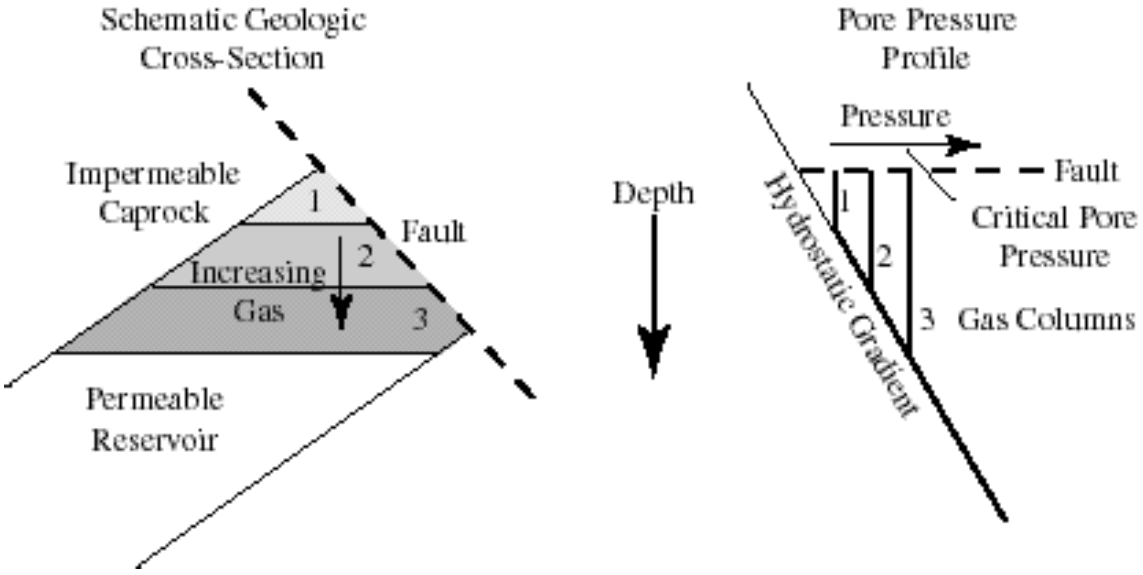

Figure 5.2: Conceptual model showing increase in pore pressure at a reservoir-bounding fault as a result of an increasing gas column in the reservoir.

To evaluate the hypothesis that parts of critically stressed faults are permeable and are the cause of localized leakage, we resolve the stress orientations and stress magnitudes we

determine in each field (see Appendix) onto distinct ~100 m x 100 m triangular elements on individual fault planes to calculate the shear and normal stress on each part of the fault. We use Coulomb frictional failure to determine which fault element is expected to slip. Coulomb frictional failure is defined in Eqn. 1, where τ is the shear stress, σ_n is the effective

$$\tau = \mu\sigma_n \qquad \text{Eqn. 1}$$

normal stress, and μ is the coefficient of sliding friction. Given that the effective normal stress is the difference between the normal stress (S_n) and the pore pressure (P_p), we solve Eqn. 1 to determine the pore pressure at which a fault element will begin to slip (Eqn. 2).

$$P_p = S_n - \tau/\mu \qquad \text{Eqn. 2}$$

We refer to this pore pressure as the critical pore pressure. In order to calculate the shear and normal stress we determine the orientation of the unit normal to the fault element in a coordinate system defined by the stress field. Figure 3A shows a fault element defined in the stress coordinate system. S_1, S_2, and S_3 are the principal stresses, a, b, and c are the vertex points of the fault element, $\hat{\mathbf{n}}$ is the unit normal to the fault element, and **t** is the traction acting on the surface of the fault element. The unit normal to the fault element is defined in Eqn. 3, where f and g are any two vectors defined by the points a, b, and c. The

$$\hat{\mathbf{n}} = \frac{\mathbf{f} \times \mathbf{g}}{|\mathbf{f}||\mathbf{g}|} \qquad \text{Eqn. 3}$$

traction acting on the fault plane is the product of the stress tensor and unit normal vector (Eqn. 4). The stress tensor is defined in Eqn. 5. We obtain the stress magnitudes from an analysis of drilling-induced tensile fractures and breakouts (Wiprut and Zoback, 2000).

$$\mathbf{t} = \mathbf{S}\,\hat{\mathbf{n}} \qquad \text{Eqn. 4}$$

$$\mathbf{S} = \begin{bmatrix} S_1 & 0 & 0 \\ 0 & S_2 & 0 \\ 0 & 0 & S_3 \end{bmatrix} = \begin{bmatrix} S_{Hmax} & 0 & 0 \\ 0 & S_v & 0 \\ 0 & 0 & S_{hmin} \end{bmatrix} \qquad \text{Eqn. 5}$$

Taking the dot product of the unit normal vector and the traction vector gives the magnitude

of the normal stress (Eqn. 6), and the magnitude of the shear stress is determined by the Pythagorean theorem (Eqn. 7). We calculate the critical pore pressure at which the fault

$$S_n = \hat{\mathbf{n}} \cdot \mathbf{t} \qquad \text{Eqn. 6}$$

$$\tau^2 = \mathbf{t}^2 - S_n^2 \qquad \text{Eqn. 7}$$

element will slip using equations 2, 6, and 7 and by assuming a coefficient of sliding friction of 0.6 (Byerlee, 1978). Figure 3B shows a graphical representation of the preceding calculation. A fault element is plotted as a point within the 3-D Mohr circle according to the shear and normal stress resolved on the fault element. The slope of the Coulomb frictional failure line passing through the fault element point uniquely defines the critical pore pressure where the failure line intersects the normal-stress axis. The critical pore pressure is compared to a reference pore pressure line drawn through the data, and the difference is called the critical pressure perturbation. This value shows how close the fault element is to slipping given the pore pressure in the reservoir, and hence is a measure of the leakage potential.

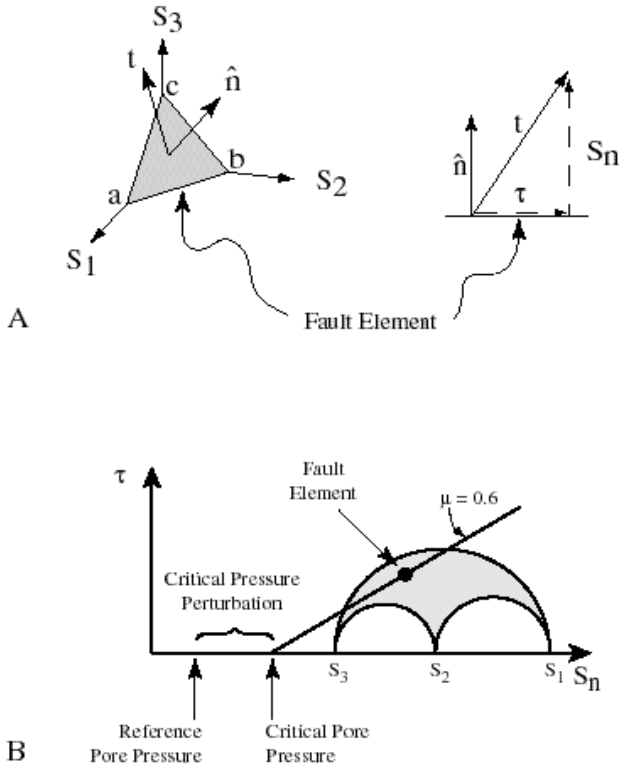

Figure 5.3: A: Orientation of a fault element in stress field. B: Mohr-Coulomb plot showing determination of critical pore pressure and comparison to reference pore pressure.

Figure 4 demonstrates the combined effect of high water-phase pore pressure and leakage along reactivated faults on the height of the hydrocarbon column. Pore-pressure-induced faulting and leakage may be a dynamic mechanism that acts to control the hydrocarbon capacity of reservoirs bounded by faults. Because high water-phase pore pressure brings the fault closer to the critical pore-pressure for failure, the potential hydrocarbon column height is diminished.

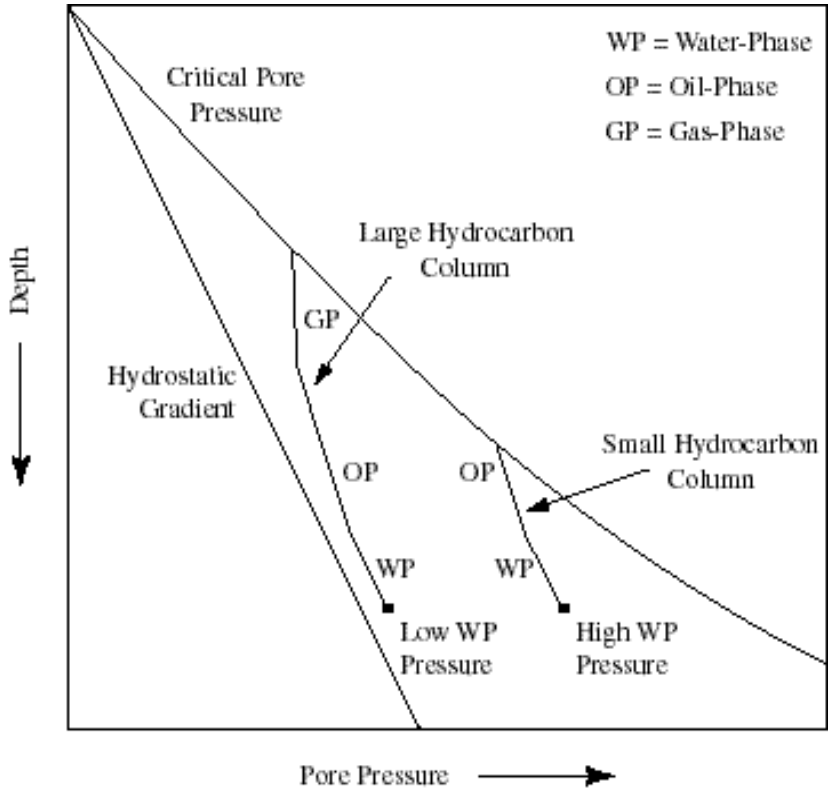

Figure 5.4: Schematic diagram showing effect of high water-phase pressure on potential hydrocarbon column height. High water-phase pore pressures greatly diminish the potential height of the hydrocarbon column.

5.4 Visund, Field 1, Field 2, and Field 3

The Visund field is located offshore Norway in the easternmost major fault block of the Tampen spur (Færseth et al., 1995) along the western edge of the Viking graben. The reservoir is divided into several oil and gas compartments, some of which are separated by the A-Central fault (Figure 5). Hydrocarbon columns were detected in the Brent group, which is the primary reservoir, as well as in the Statfjord and Amundsen formations. As shown in Figure 5A, low seismic reflectivity along the southern part of the A-Central fault at the top Brent reservoir horizon is interpreted to be the result of gas leakage from the

reservoir. The data in this region are very high quality and there are no changes in lithology that might account for the change in seismic reflectivity. Figure 5A also shows the mean orientation of the maximum horizontal stress determined in five wells in and near the Visund field from observations of drilling-induced tensile wall fractures (Moos and Zoback, 1990; Brudy and Zoback, 1993, 1999). Drilling-induced tensile wall fractures have been shown to be reliable indicators of the direction of the maximum horizontal stress (Brudy et al., 1997, Wiprut and Zoback, 2000).

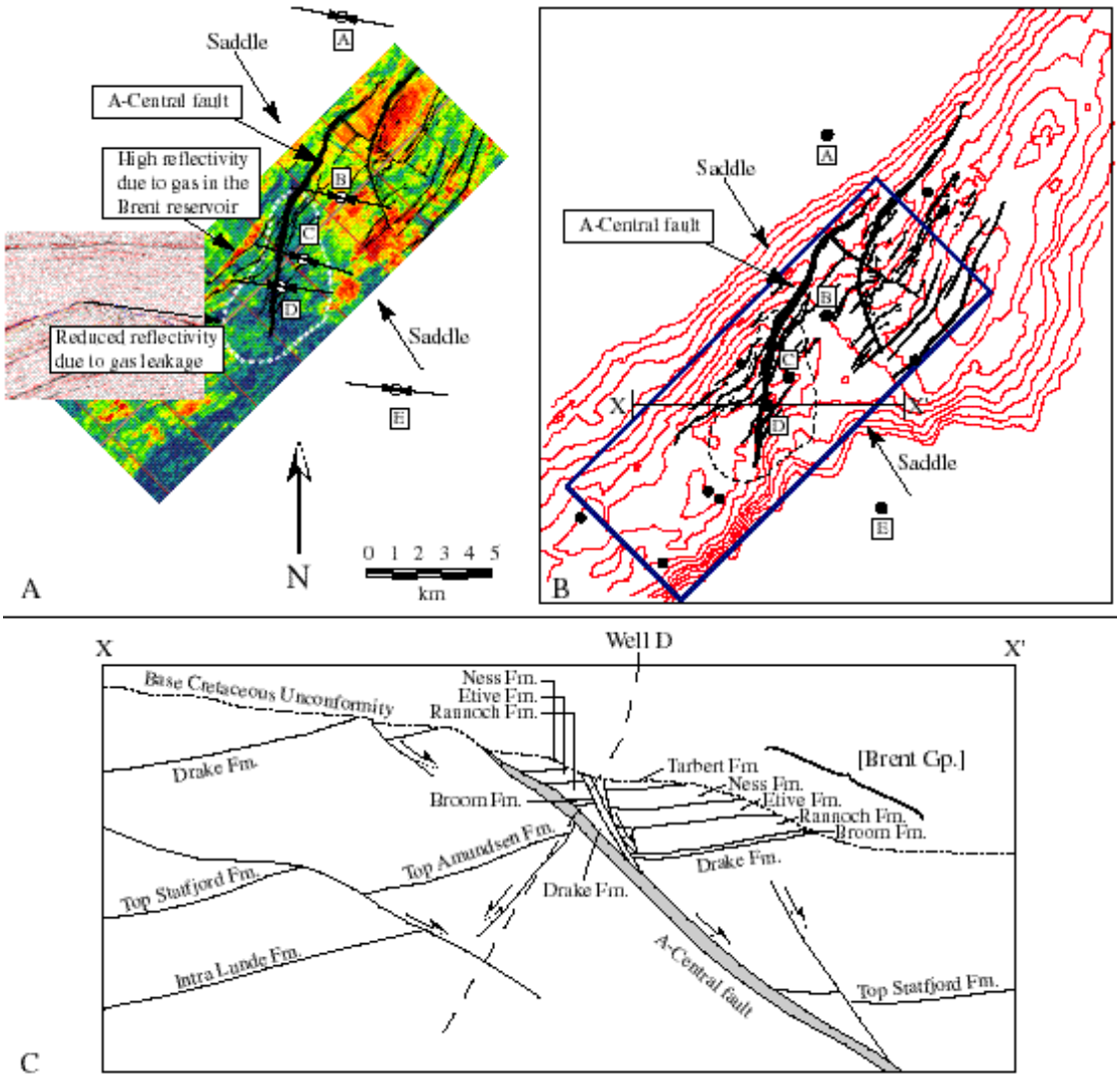

Figure 5.5: A: Map view of Visund field showing seismic reflectivity of reservoir horizon as well as mean orientation of maximum horizontal stress in five wells (A-E). B: Contour map of top Brent reservoir horizon. Saddle defines local structural low along reservoir horizon. C: East-west cross-section through Visund field. Cap rock defined by short-dashed base Cretaceous unconformity. Trajectory of well D through A-Central fault shown with long dashes.

Figure 5B shows a contour map of the top Brent reservoir horizon (red lines), with the faults, lateral extent of gas leakage (dashed line, see Fig. 5A), and outline of the map area shown in Figure 5A (blue rectangle) superimposed on the structural contours. Exploration wells which yielded stress and pore pressure data are shown with black circles. The Brent reservoir consists of a ridge running northeast-southwest with a saddle crossing perpendicular to the ridge between wells B and C. Comparison of the maps in Figures 5A and 5B shows the ridge is trapping gas along most of its length except for the portion of the ridge defined by the dashed low-reflectivity area. In the lower part of Figure 5B, the southern boundary of the Brent reservoir plunges steeply into the Viking graben. This is the result of a large northeast-southwest trending graben-bounding fault which intersects the southern end of the A-Central fault. The effect of the graben-bounding fault can be seen in Figure 5A as well, where there is a sharp transition from high to low reflectivity in the southern portion of the map.

Figure 5C shows a schematic cross-section running approximately east-west through well D and the A-Central fault. The A-Central fault developed during the Jurassic as a normal fault with an ~60˚ dip (Færseth et al., 1995) and as much as 300 m of normal throw (Linn Arnesen, Norsk Hydro, 1998, personal communication). Since that time, the fault appears to have rotated and now dips between 30˚ and 45˚. The other major faults in Visund generally dip 20˚ to 40˚ to the east, with some smaller antithetic faults dipping to the west.

Figure 6A shows a map of Field 3 with the faults and mean orientation of the maximum horizontal stress determined in four wells in this area. Other exploration wells which yielded stress and pore pressure data are shown by black circles. Figure 6B shows a schematic cross-section through two wells in the field along the line W-W'. The Brent reservoir in Field 3 typically dips between 3˚ and 10˚ to the east and southeast in individual fault blocks, but overall becomes shallower to the south-southeast in this region. Reservoir-bounding faults in Field 3 generally strike in two directions, with a northeast-southwest striking set of faults cross-cutting a north-south striking set. The faults typically dip between 50˚ and 60˚ throughout the field. Three east-west oriented cross-sections cut through wells A and F along lines X-X', Y-Y', and Z-Z', and are shown in Figure 7. Cross-section Y-Y' indicates there is some amplitude dimming above the fault east of well A, which is interpreted to be the result of gas leakage from the reservoir.

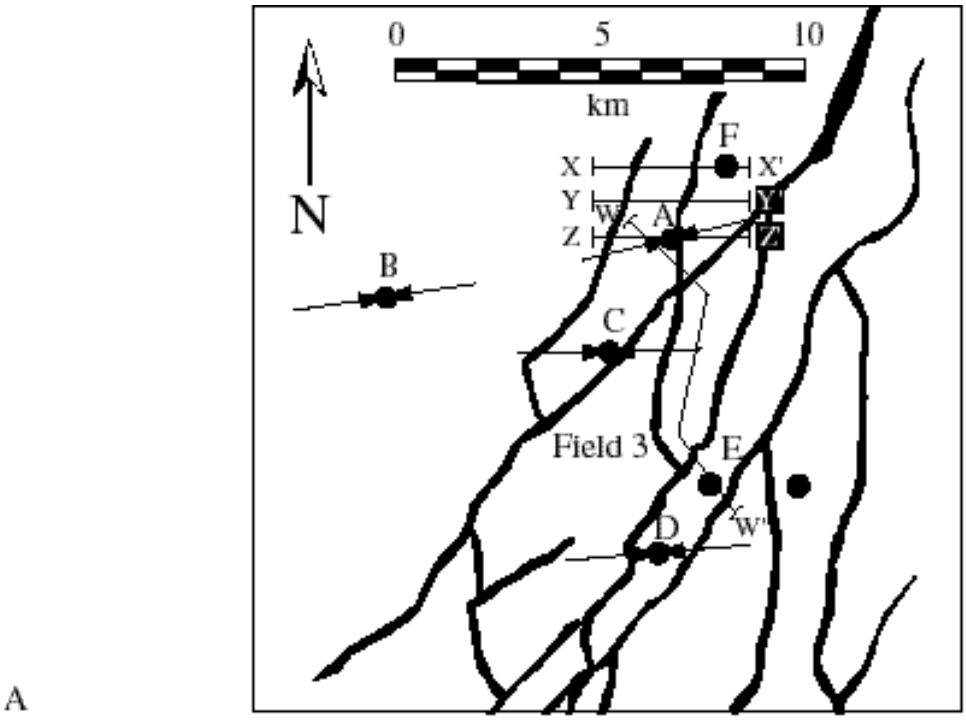

A

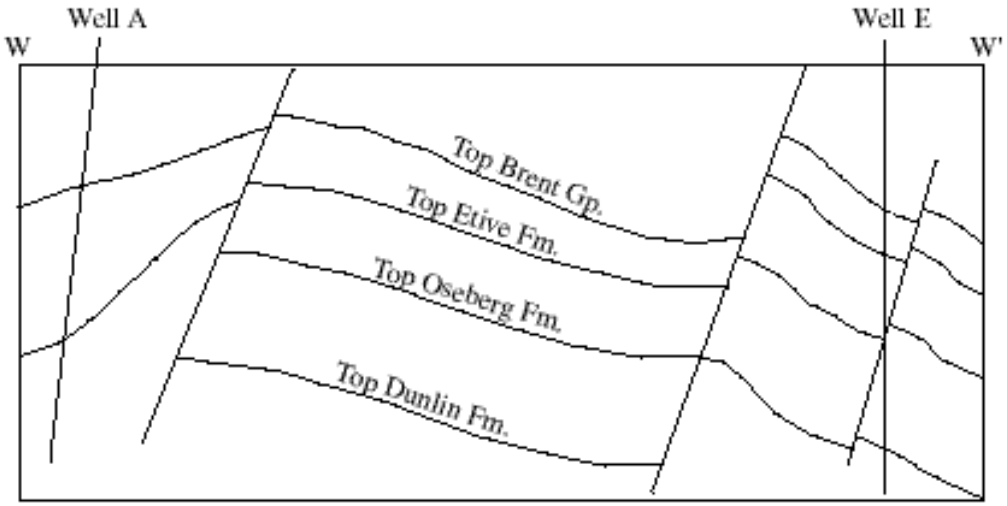

B

Figure 5.6: A: Generalized map of Field 3 field showing orientation of the maximum horizontal stress (inward pointed arrows), exploration wells (circles), and major faults. Cross-sections X-X', Y-Y', and Z-Z' are shown in figure 7. B: Schematic cross-section through two wells in the Field 3. Structural dips are generally to the east and southeast.

Figure 8A shows a map view of the Field 1 and Field 2 with the faults and mean orientation of the maximum horizontal stress determined in five wells in this area. Other exploration wells which yielded stress and pore pressure data are shown by black circles. Field 1 is a small discovery approximately 5km west of Field 2. Reservoirs in Field 1 are quite deep with Brent reservoir sandstones encountered between approximately 3500 and 4100 meters. Both Field 1 and Field 2 are filled from sources to the west, and structural dips are to the east between approximately 1˚ to 10˚ in Field 1 and between 2˚ to 14˚ in Field 2. Figure 8B shows a schematic cross-section through well F in Field 2 which gives a generalized picture of the structure in this area. Major reservoir-bounding faults in this area strike approximately north-south, and dip to the west between 40˚ and 55˚.

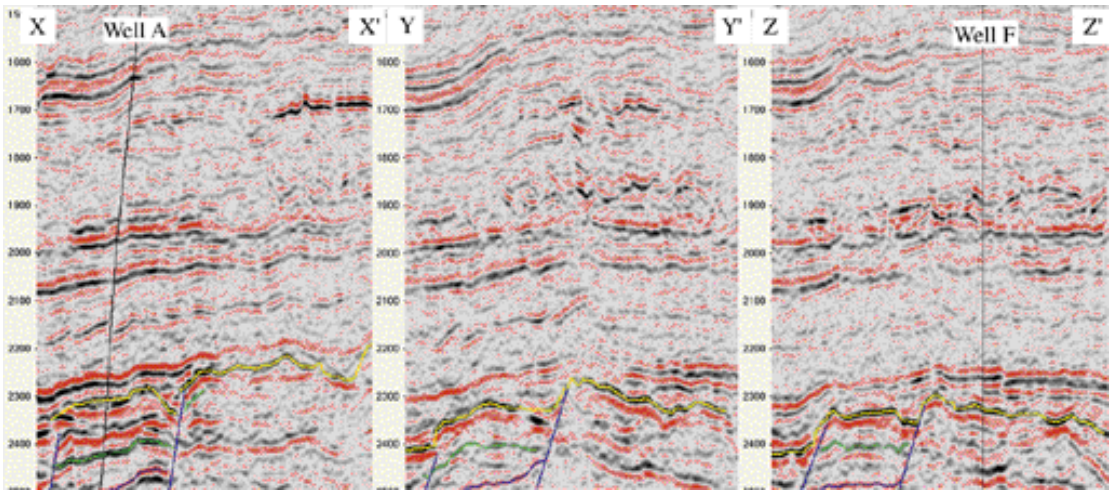

Figure 5.7: East-West seismic sections through well A (left panel), and well F (right panel). Middle panel shows leakage along reservoir-bounding fault between two wells inferred from reduced seismic amplitudes.

Figure 9 shows summaries of the in situ stress and pore-pressure data for Visund (A) and Field 1 (B) over the depth ranges of principal interest. Stress and pore pressure data in Field 2 and Field 3 are shown in Figure 10A and 10B respectively. The pore-pressure data are direct measurements made in the reservoir. The vertical stress was derived by using the average overburden gradient across each field. We calculated the overburden in each well by integrating density logs. The data for the minimum horizontal stress were derived from analysis of carefully conducted leak-off tests (LOTs). The magnitude of the maximum horizontal principal stress was determined from analysis of drilling-induced tensile fractures (following Zoback et al., 1993; Brudy et al., 1997). Determinations of stress magnitude and orientation in Visund are described in detail by Wiprut and Zoback (2000). Determination of stress magnitude and orientation in Field 1, Field 2, and Field 3 is

discussed in the Chapter 3.

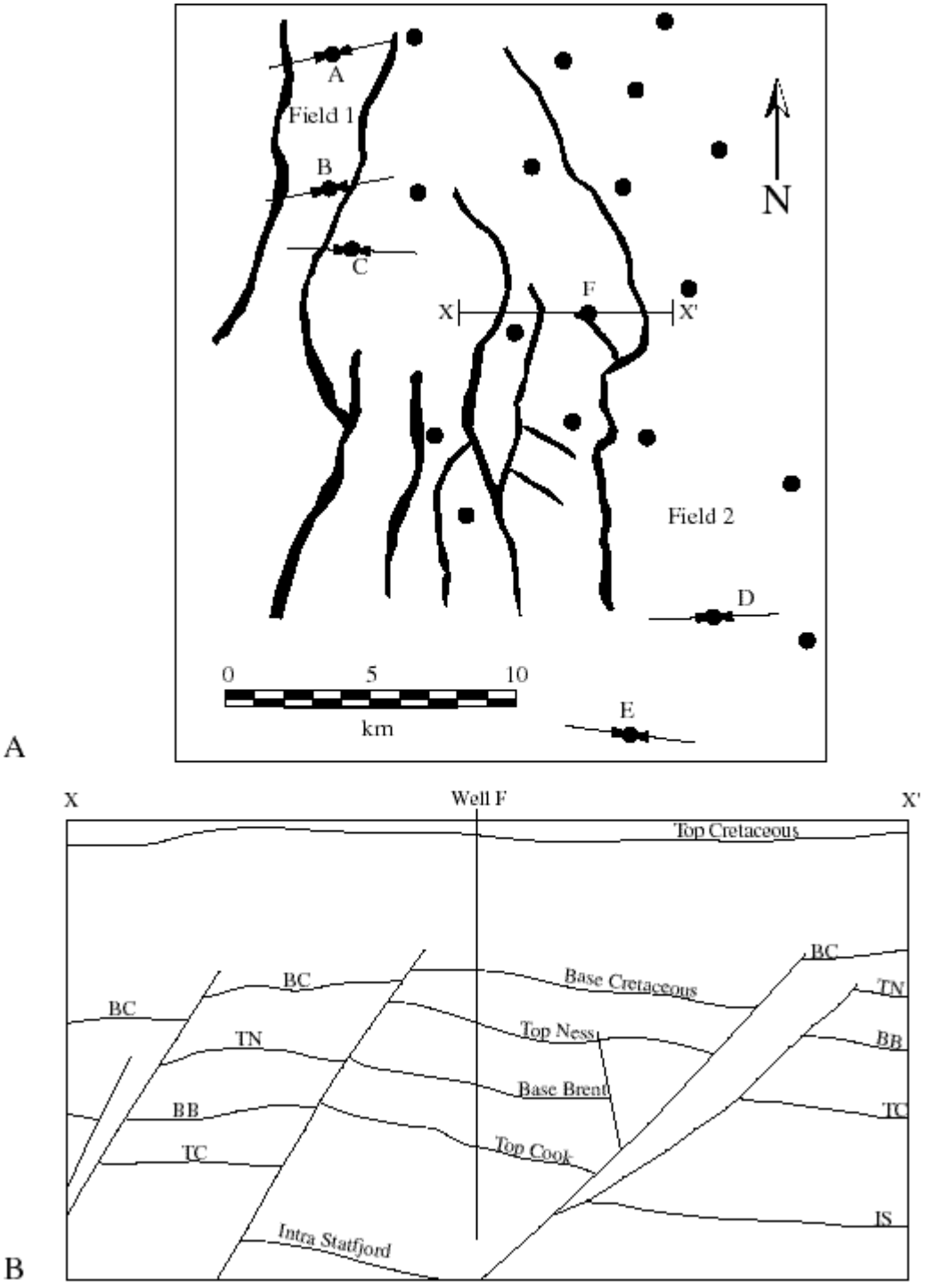

Figure 5.8: A: Generalized map of Field 1 and Field 2 showing orientation of the maximum horizontal stress (inward pointed arrows), exploration wells (circles), and major faults. B: East-west cross section along X-X' passing through well F in the Field 2. Major faults generally dip steeply west.

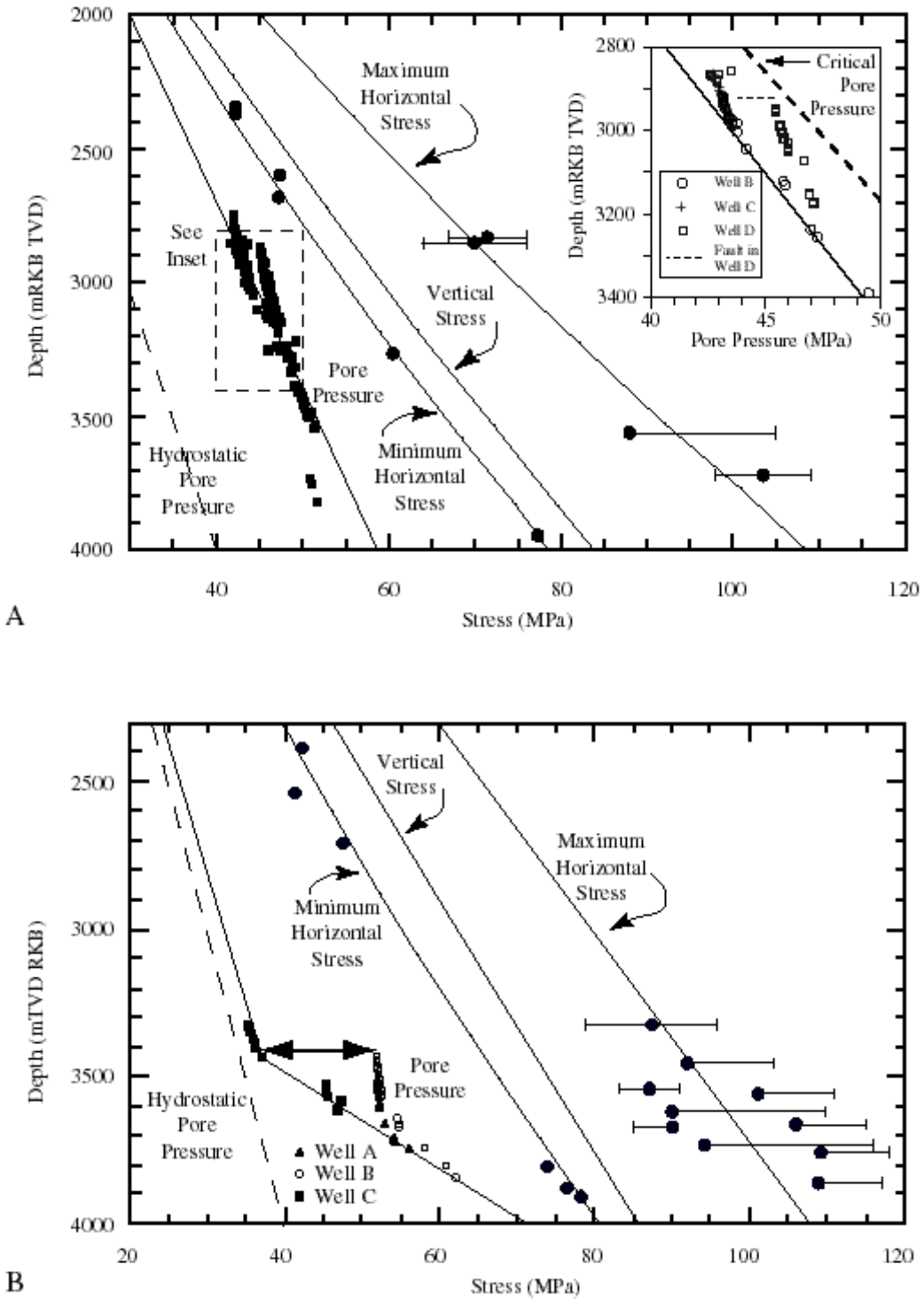

Figure 5.9: In-situ stress and pore-pressure data obtained from wells throughout Visund (A) and Field 1 (B). Best-fit lines to data are shown. Depths are meters relative to kelly bushing, true vertical depth. A: Inset shows pore-pressure measurements in three wells drilled close to A-Central fault. B: See text for explanation of arrow.

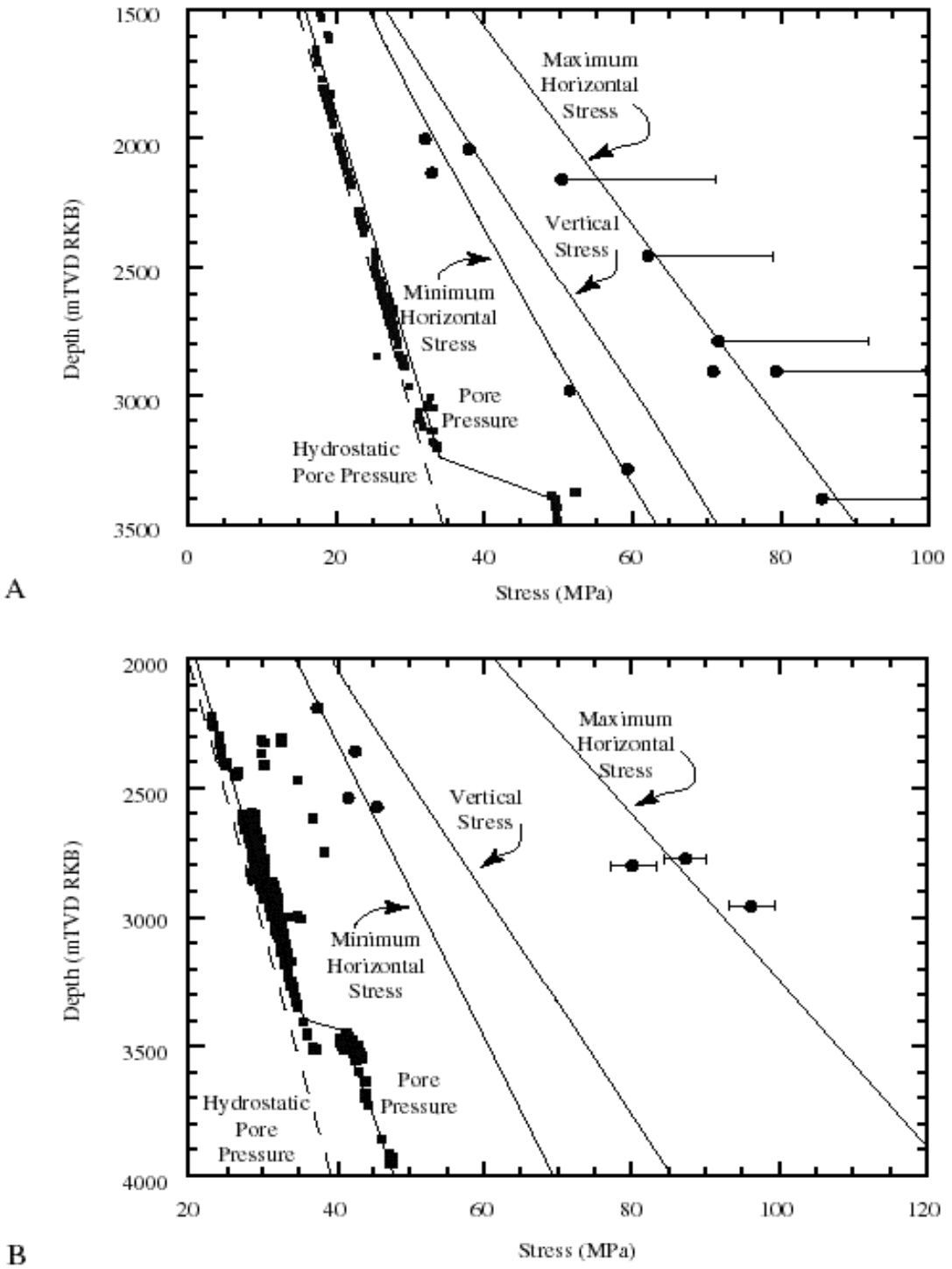

Figure 5.10: Stress versus depth in Field 3 (A) and Field 2 (B). Depth is measured in meters, true vertical depth relative to kelly bushing. Hydrostatic pore pressure is shown by a long-dashed line. Pore pressure data are shown with small squares. Minimum horizontal stress is shown with large triangles. Vertical stress is shown by solid line. Maximum horizontal stress is shown by large circles.

Pore pressures in Visund are significantly above hydrostatic throughout the reservoir (Figure 9A). The inset of Figure 9A shows a detailed view of the pore-pressure measurements in the three wells closest to the A-Central fault. Well D was deviated to penetrate the A-Central fault at 2933m true vertical depth (indicated by the horizontal dashed line), whereas wells B and C were drilled vertically. The steep pressure gradient in well D is the result of light oil rather than free gas. A free gas cap was not detected in well D, which is consistent with the reduced seismic reflectivity shown in Figure 5A. The pore-pressure data in well D are discussed in more detail subsequently.

Pore pressures in Field 1 remain nearly hydrostatic until 3500 meters, where they increase rapidly (Figure 9B). There is a marked pore-pressure difference between wells A and B on the hanging wall side of a major north-south trending fault in Field 1, and well C on the footwall side of the fault. Pore pressures in wells A and B follow a steep gas gradient toward the top of the hydrocarbon column, whereas the pore pressures in well C appear to primarily mirror the hydrostatic gradient. The pore pressure difference across the fault between wells B and C is shown by the arrow and is approximately 15 MPa.

Pore pressures in both Field 2 and Field 3 remain hydrostatic until approximately 3400 meters, where there is an increase in pore pressure in both fields (Figure 10). The reservoir is highly overpressured in Field 3 and in Field 2 there is only moderate overpressure. Both pore pressure trends continue to mirror the hydrostatic gradient in the overpressured sections. A number of anomalous pore pressure measurements in the shallower parts of Field 2 come from approximately 5 wells scattered throughout the region, and do not reflect the overall pore pressure trend in any one compartment (Figure 10B).

Note that the maximum horizontal stress is distinctly larger than the vertical stress, and the minimum horizontal stress is nearly equal to the vertical stress across the study area. This result is consistent with the strike-slip and reverse-slip stress field indicated by earthquake focal-plane mechanisms (at 5 to 30 km depth) in this part of the North Sea (Lindholm et al., 1995). As earthquakes along passive continental margins such as Norway's are quite rare, a number of investigators have suggested that the compressional stress observed in this region may be related to lithospheric flexure associated with Pleistocene deglaciation (Stephansson, 1988; Klemann and Wolf, 1998; Grollimund et al., 1998). If this interpretation is correct, the existence of the current compressional stress in this area is a geologically recent (~10,000-15,000 yr. old) phenomenon. However, there have been studies claiming longer-term compression in the North Sea inferred from inversion structures observed offshore Norway (Rohrman et al., 1995; Vågnes et al., 1997), and bordering other sections of the northeast Atlantic Margin (Doré and Lundin, 1996). These studies generally indicate compression may have started with ridge push from Meso-

Cenoczoic time and extended into the Neogene.

5.5 Leakage Potential & Hydrocarbon Column Height

Figure 11 shows a perspective view, looking down to the north, of all the major faults in the Visund field. The perspective view in this figure creates distortions, therefore the scales are approximate. The five wells which provided data for the maximum horizontal stress are labeled, and other wells which provided pore pressure data are shown as white circles. The faults are colored to indicate the likelihood of leakage along the surfaces. The color shows the difference between the critical pore pressure we calculate and the reference pore pressure line shown in Figure 9A. This difference is called the critical pressure perturbation (see previous explanation and Figure 3B). Red colors indicate that a small increase in pore pressure (<~7 MPa) is enough to bring the fault to failure. Blue colors indicate that the pore pressure must rise significantly (>20 MPa) before those parts of the fault will begin to slip in the current stress field. Figure 11 seems to indicate that many faults in the Visund field should be slipping and leaking hydrocarbons. However, our maps only indicate the potential for hydrocarbon leakage along any fault, and do not imply any fault with red colors is currently leaking. The reservoir must abut the fault in the proper place, there must be hydrocarbons present to leak, and the pore pressure must be high enough to reactivate the fault in order for the leakage to take place.

Figure 12 shows leakage potential maps for Field 1, Field 2, and Field 3. Comparison of Figures 11 and 12 shows that the shallowly dipping faults in Visund generally have the highest likelihood of leakage. Field 3 is also quite likely to leak from many of the more steeply dipping northeast-southwest trending faults, and is less likely to leak from the north-south trending faults. The north-south oriented steeply dipping faults in Field 1 and Field 2 have the lowest likelihoods of leakage.

As noted previously, there is evidence of hydrocarbon leakage in Visund (Figure 5A). The evidence for gas leakage in the immediate vicinity of the A-Central fault points to the fault as the possible conduit by which hydrocarbons are escaping from the reservoir. Figure 13 shows two views of the A-Central fault as determined from three-dimensional seismic reflection data. In the upper part of Figure 13, a simplified map view of the fault is shown along with the orientation of the maximum horizontal stress in the three wells closest to the fault. The shaded area shows the lateral extent of gas leakage (simplified from Figure 5A). In the lower part of Figure 13, a perspective view of the approximately east-dipping fault surface is shown. A dark circle on the fault plane indicates the point where well D penetrates the A-Central fault. Note that the largest part of the fault that is most likely to

slip (i.e., shaded in red) is located along the same part of the fault where leakage seems to be occurring. Thus, there appears to be a good qualitative correlation between the critically-stressed-fault criterion and the places along the fault where leakage appears to be occurring.

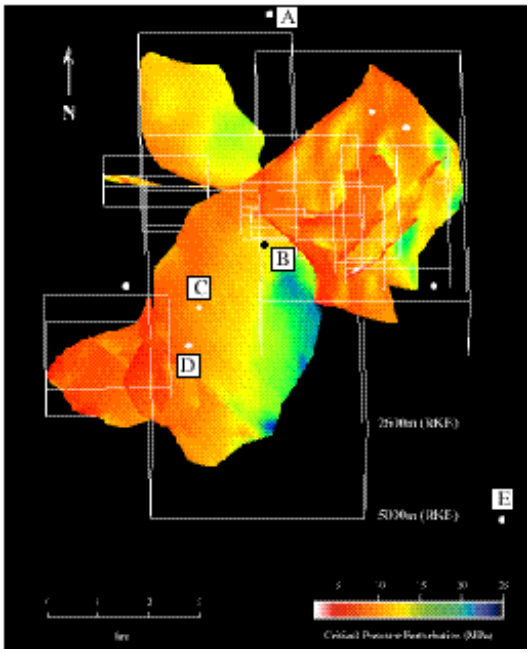

Figure 5.11: Perspective view of fault surfaces in Visund showing leakage potential. The A-Central fault is shown with depths listed on the bounding box. Perspective view is colored to show excess pore pressure needed to induce fault slip in the current stress field. Note the scales are approximate, as the perspective view creates distortions.

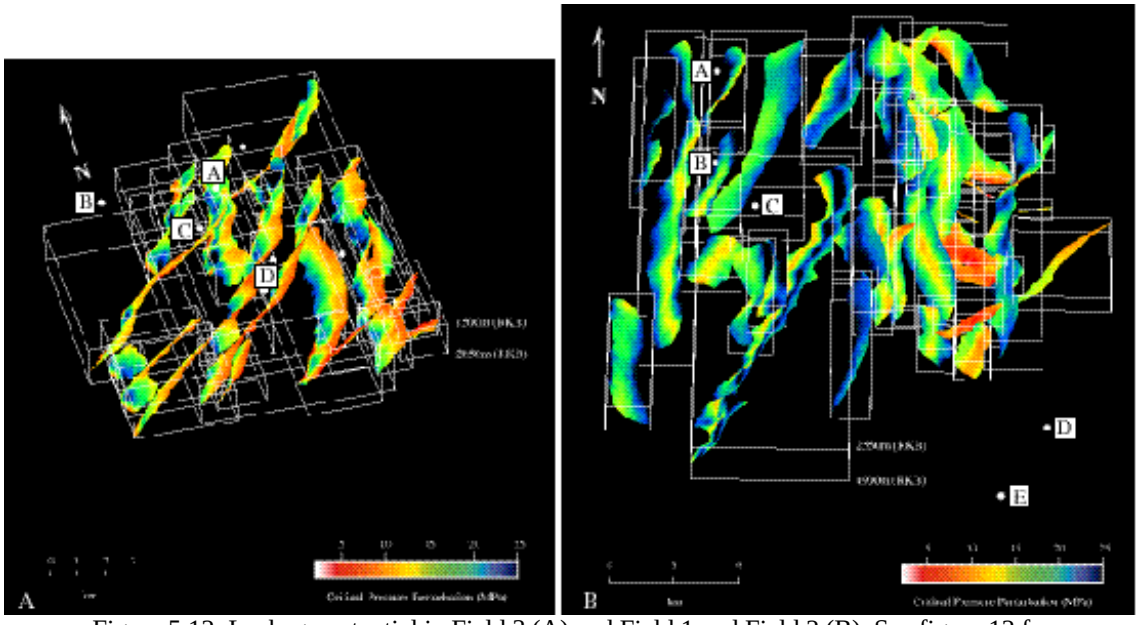

Figure 5.12: Leakage potential in Field 3 (A) and Field 1 and Field 2 (B). See figure 12 for explanation.

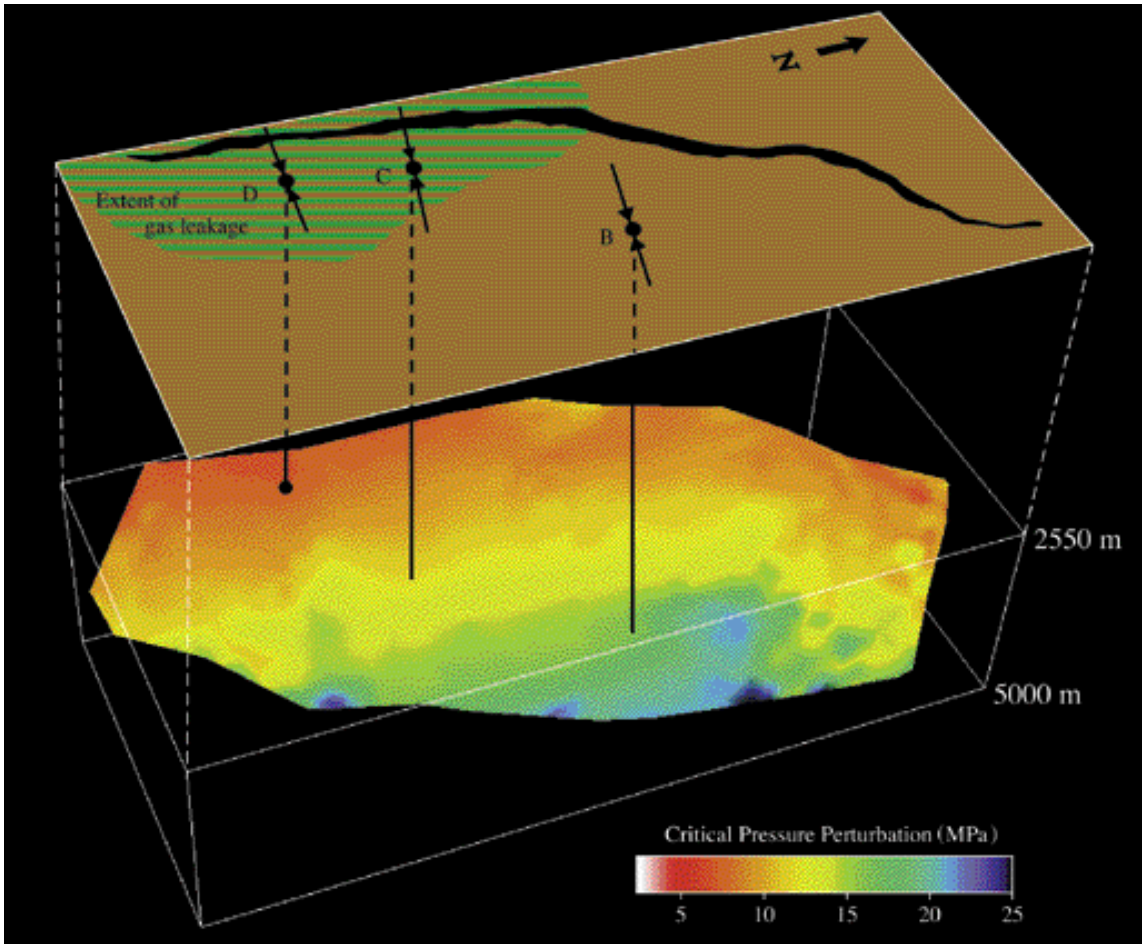

Figure 5.13: Map view and perspective view of A-Central fault as determined from three-dimensional seismic reflection survey. Map view shows region of gas leakage inferred from reduced seismic reflectivity (Fig. 5A). Perspective view is colored to show excess pore pressure needed to induce fault slip in the current stress field. The part of the fault that is most likely to slip corresponds to that which appears to be leaking.

Because well D penetrates the fault in this area, we can evaluate the correlation between the gas leakage and our prediction of leakage more quantitatively. As shown in the inset of Figure 9A, the pressure below the fault (indicated by the position of the dashed horizontal line) is within ~1 MPa of the theoretical critical pore pressure for fault slippage (the thick dashed line). This value is several megapascals above the reference pore pressure, just as predicted in Figure 13. Above the fault, pore pressures are significantly reduced, indicating that there is poor pressure communication across the fault. The A-Central fault is connected at its southern end with the graben-bounding fault described previously, preventing hydrocarbons from migrating from the footwall to the hangingwall. Geochemical analysis of gas from both sides of the fault indicates that the hydrocarbons are derived from different sources (i.e., no fluid flow across the fault) (Arnd Wilhelms, Norsk Hydro, 1998, personal

communication). It is interesting to note that although the pore pressure in the footwall appears to have caused the A-Central to slip and leak, both the footwall and hangingwall show reduced seismic reflectivity. Increased permeability resulting from fault slip seems to influence pore pressure compartments on both sides of the fault. The pore pressures shown in the inset of Figure 9A indicate wells B, C, and D are in the same pressure compartment on the hangingwall, yet well B does not penetrate an area of reduced reflectivity. This is the result of the saddle shown in Figure 5B. The local structural low provided by the saddle effectively separates the gas in well B from wells C and D. Because leakage appears to be localized to the region where the fault is most likely to slip, fault slip rather than capillary-pressure effects seem to be responsible for the gas leakage. Thus, in this case, as with cases reported by Barton et al. (1995), Hickman et al. (1998), and Finkbeiner et al. (1998), fault slip appears to have principally promoted fault-parallel flow.

We also previously noted evidence of hydrocarbon leakage in Field 3 (Figure 7). Figure 12A shows that the lowest critical pressure perturbation along this fault between wells A and F is approximately 10 MPa. As shown in Figure 6B, the reservoir intersects the fault at 2540 meters, and the shallowest pore pressure measurement in this reservoir is at the gas-oil contact at 2600 meters. A 60 meter column of gas above 2600 meters increases the pore pressure approximately 3 MPa above the background pore pressure. This results in a pore pressure acting at the fault that is 7 MPa below the pore pressure we calculate is needed to activate the fault in the current stress field. Two factors may contribute to the discrepancy between the observed gas leakage and the predicted pore pressure needed to cause the leakage. First, the maximum horizontal stress used at this depth may underestimate the actual stress. Because the upper bound of S_{Hmax} was poorly constrained in well A, the lower bound was used as the best estimate of the maximum horizontal stress. Second, the pore pressure on the footwall side of the fault may be higher than in the hangingwall, but no pore pressure data were available for well F.

Geochemical studies of hydrocarbons from Field 3 and a field to the south indicates there is a southward migration of gas. The migration of hydrocarbons might be expected due to the overall trend of the Brent reservoir becoming shallower to the south south-east in this area, but the individual fault blocks dip to the east and south-east, which would encourage migration in a west and north-westerly direction. We speculate that in order for hydrocarbons to migrate to the south and south-east, the reservoir bounding faults might be conducting hydrocarbons along strike. However, we have no direct observations indicating hydrocarbons are being conducted along these faults.

Examination of seismic cross-sections in Field 1 and Field 2 showed no evidence of hydrocarbon leakage, and there is no evidence of hydrocarbon migration at the present in

these fields. Note that most of the faults in Field 1 and Field 2 do not show any significant potential for leakage compared to Visund and Field 3 (Figures 11, 12B). This is primarily the result of the faults being poorly oriented for frictional failure in the current stress field. Figure 12B shows our analysis predicts there should be no leakage and it also shows the reservoirs may potentially maintain large pore pressure differences across compartments. According to our analysis, the major fault to the east of well B in Field 1 can potentially maintain up to approximately 15 to 17 MPa pore pressure difference across its surface at the weakest points. The pore pressure data in this field show a pressure difference of approximately 15 MPa between the pore pressure trend used to create Figure 12B and the hydrocarbon column supported by the major fault east of well B (Figure 9B, see arrow).

In Field 2, the stress data come from wells far outside the field (Figure 8A). In order to create leakage potential maps in all of the fields, the stress data must be extrapolated throughout each field. We combine the stress and pore pressure data across the entire field into a single one-dimensional model that varies with depth, and extrapolate this model across the entire field. Therefore, there is some uncertainty about the leakage analysis in areas far removed from the wells with stress data. The leakage analysis in this field is therefore not as reliable as in Field 1, Field 3, or Visund. However, the results are still consistent with the observation that the faults are not conducting hydrocarbons in the field. A few smaller east-west trending faults appear to be capable of leaking in Field 2. Examination of these faults indicates they are not large enough to separate pore pressure compartments.

In Visund the hydrocarbon column heights were smaller than expected (Roald Færseth, Norsk Hydro, 2000, personal communication). Because the water-phase pore pressure was so high in Visund, and the faults so close to slipping and leaking, we believe this prevented larger hydrocarbon columns from accumulating in the reservoir. We show Field 3 is slightly less likely to leak than Visund, but the pore pressures are predominantly hydrostatic. However, because the faults in Field 3 may conduct hydrocarbons to the south, the hydrocarbon column height is limited. Field 1 and Field 2 have a very low likelihood of leakage and appear to be capable of maintaining large columns of hydrocarbon in the deeper reservoirs where the faults are unlikely to slip and leak.

We speculate that the direction of fault slip may be controlling the direction of hydrocarbon leakage and migration in sedimentary basins. Perhaps gouging of the fault surfaces creates preferred paths of fluid flow within the fault itself. For example, in Visund, where the fault slip was most likely in a reverse sense, the hydrocarbons were not conducted perpendicular to the fault or along strike, but were conducted up dip into the cap rock. In Field 3, where the most well-oriented faults are likely to move in a strike-slip sense,

the hydrocarbons appear to be migrating along strike to the south into Troll. In the case where leakage is seen above the fault in Field 3, the fault is poorly oriented for strike-slip motion, and may be moving in a reverse sense. This is an unexpected correlation that should be investigated further in other fields, as it is quite different from the simple increase in permeability that seems to be observed in crystalline rock studied by Barton et al. (1995, 1998) and Hickman et al. (1998). It is, however, consistent with the observation of up dip hydrocarbon migration made by Finkbeiner et al. (2001) in Gulf of Mexico normal faults.

APPENDIX A

QUALITY RANKING SYSTEM FOR STRESS ORIENTATION FROM DRILLING INDUCED TENSILE FRACTURES

A.1 Quality ranking system

Zoback and Zoback (1989) defined a quality ranking system for stress orientation data which established a qualitative measure of the reliability of the data and the degree to which the different stress indicators represented the tectonic stress field. The types of data they considered were focal mechanisms, wellbore breakouts, hydraulic fractures, petal centerline fractures, overcore, fault slip, and volcanic vent alignment. This study represents the first almost exclusive use of drilling-induced tensile fractures to determine the orientation of the present-day stress field. Because this is a relatively new technique for constraining the in-situ stress a new quality ranking system had to be created to asses the reliability of this data. Table 1 shows the new ranking system. Note that all of the fractures were required to be at least 0.2 meters in length in order to be considered genuine tensile fractures. In cases where the data appeared predominantly on one side of the hole the tensile fractures had to appear on both sides of the hole at some point in order to be recognized as drilling-induced tensile fractures and not tool marks.

TABLE A1.

Quality A	Quality B	Quality C	Quality D
Tensile fractures (either parallel to the wellbore or en-echelon) appear on both sides of hole approximately 180 degrees apart. Ten or more zones of tensile fractures collectively extending over more than 300 meters of the well. S.D. ≤ 12 degrees.	Tensile fractures (either parallel to the wellbore or en-echelon) appear on both sides of hole approximately 180 degrees apart. Six to nine zones of tensile fractures collectively extending over at least 100 meters of the well. S.D. ≤ 20 degrees.	Tensile fractures appear on only one side of hole, but are easily identified as tensile fractures. Four to five zones of tensile fractures collectively extending over at least 30 meters of the well.S.D. ≤ 25 degrees.	Tensile fractures appear on only one side of the hole and are not easily identified as tensile fractures. Less than four zones of tensile fractures collectively extending over less than 30 meters of the well. S.D. > 25 degrees.

S.D. = Standard Deviation

APPENDIX B

EXAMPLES OF DRILLING-INDUCED TENSILE FRACTURES SEEN IN FMS AND FMI LOGS

B.1 Data Examples

Formation MicroImager and Formation MicroScanner data from taken from a number of wells in Visund, well C in Field 1, and well B in Field 3 are shown in the following figures. These plots are “unwrapped” views of the wellbore with the azimuth from north shown along the top of each figure. The gray lines at an azimuth of approximately 270˚ in some of the figures show the pad 1 azimuth, and are used to orient the tool in the hole. Note that in cases where the tensile fractures appear on both sides of the hole they are diametrically opposed, as expected from theory.

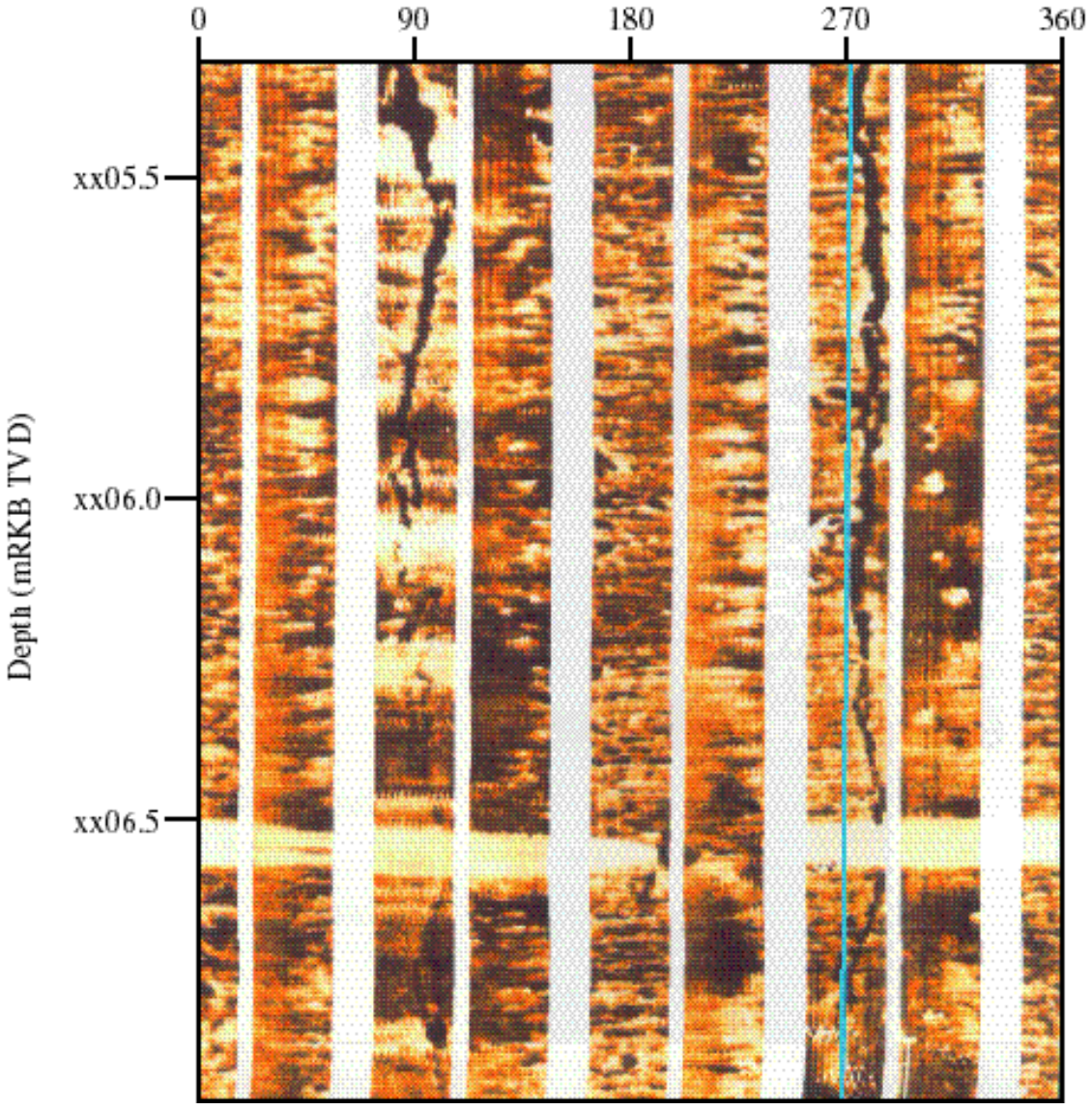

Figure B.1: FMI image of near-axial drilling-induced tensile wellbore failures in Visund well D. The tensile cracks appear at azimuths of approximately 90˚ and 270˚ in this plot.

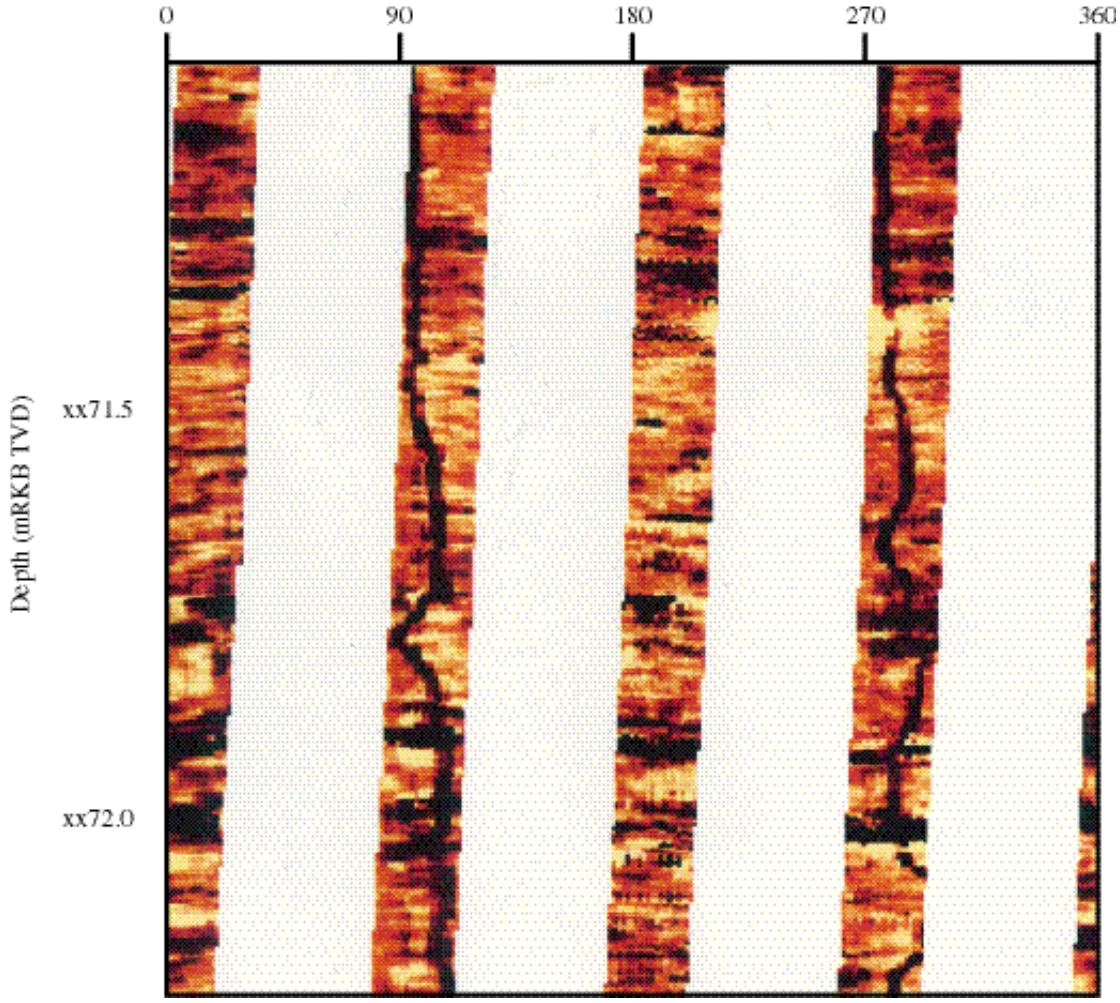

Figure B.2: FMS image of near-axial drilling-induced tensile wellbore failures in Field 1 well C. The tensile cracks appear at azimuths of approximately 100˚ and 280˚ in this plot.

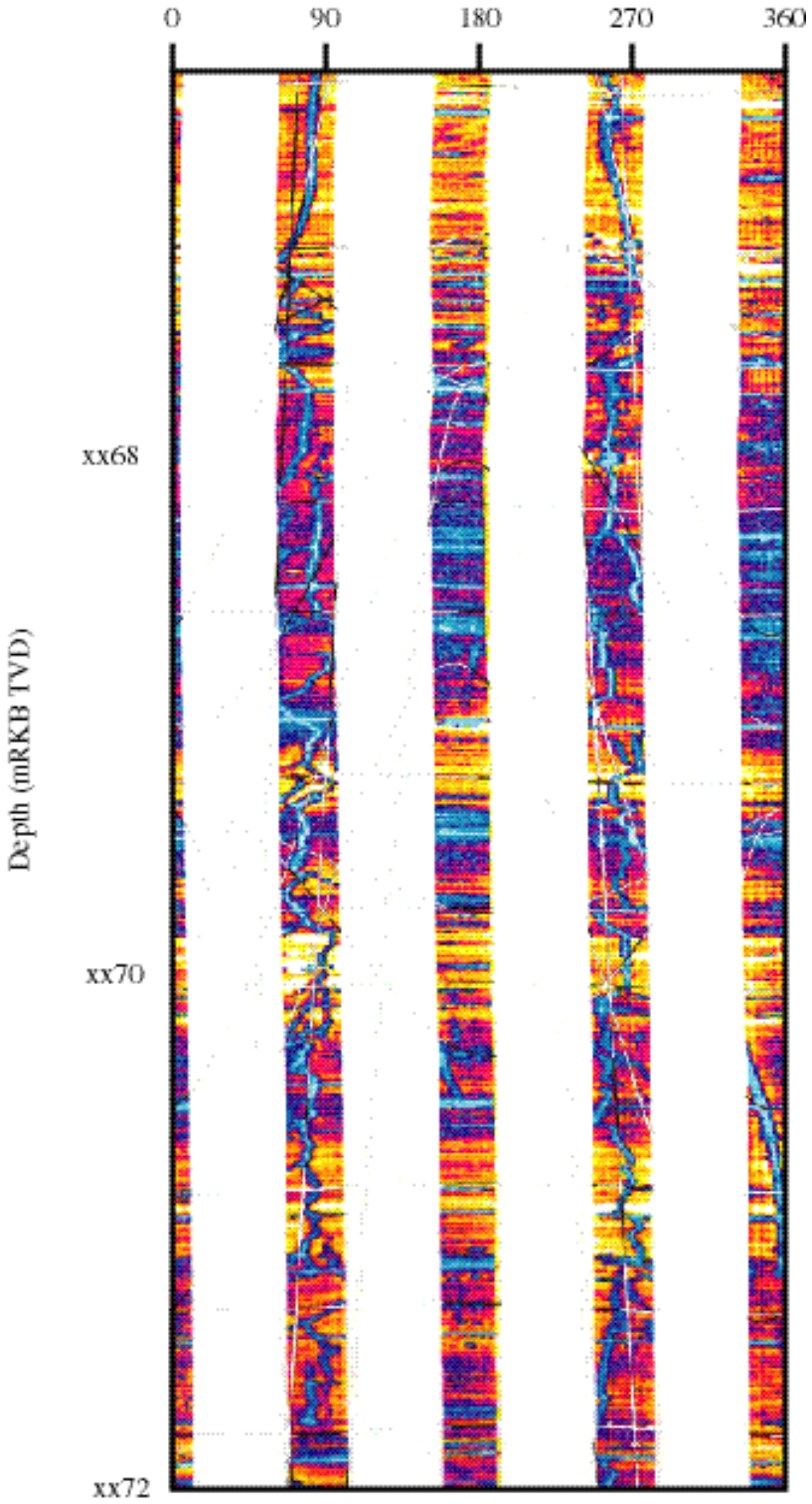

Figure B.3: FMS image of near-axial drilling-induced tensile wellbore failures in Field 3 well B. The tensile cracks appear at azimuths of approximately 80˚ and 260˚ in this plot.

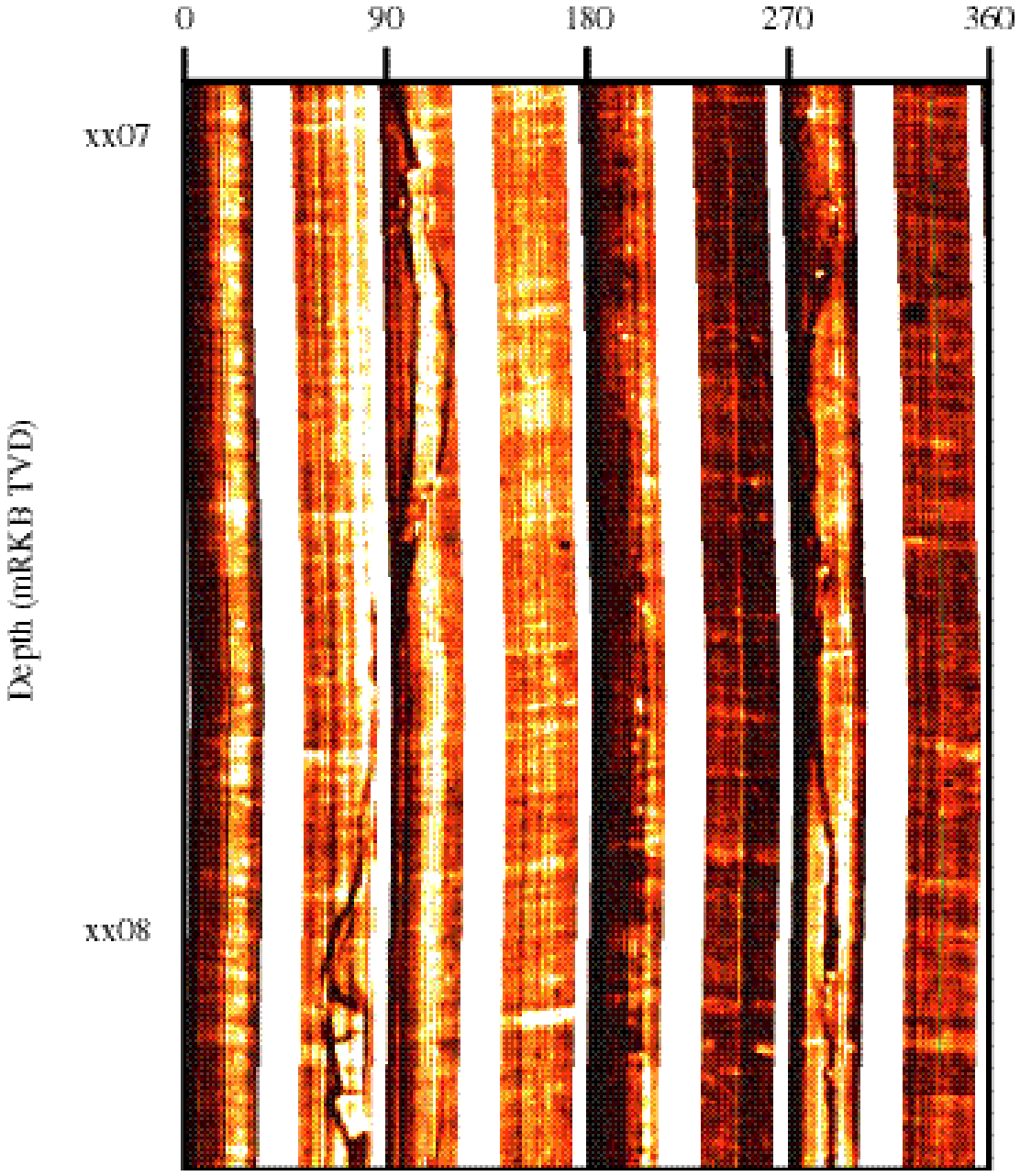

Figure B.4: FMI image of near-axial drilling-induced tensile wellbore failures in Visund well C. The tensile cracks appear at azimuths of approximately 90˚ and 270˚ in this plot.

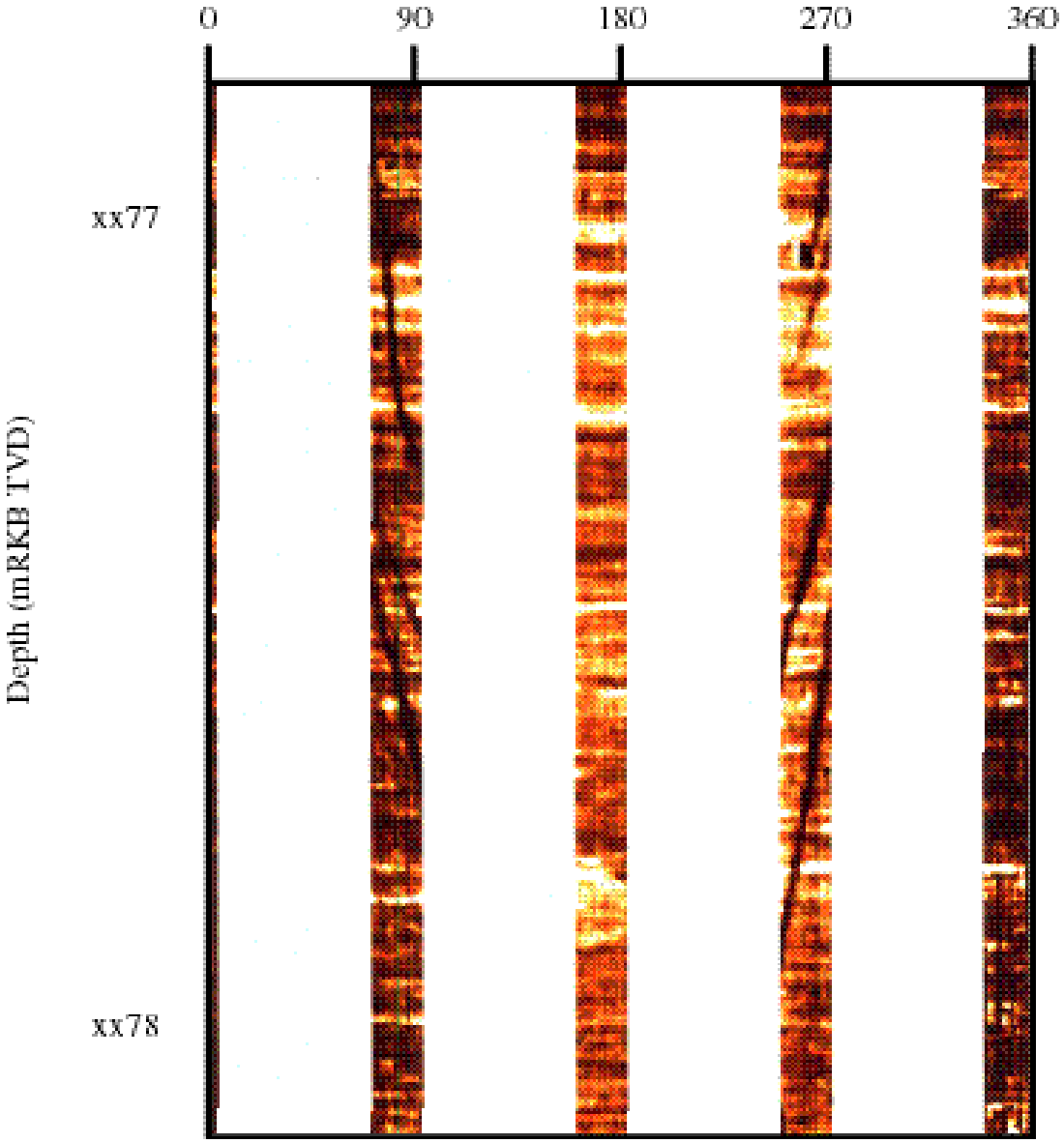

Figure B.5: FMS image of inclined drilling-induced tensile fractures in Visund well A. The tensile cracks appear at azimuths of approximately 80˚ and 260˚ in this plot.

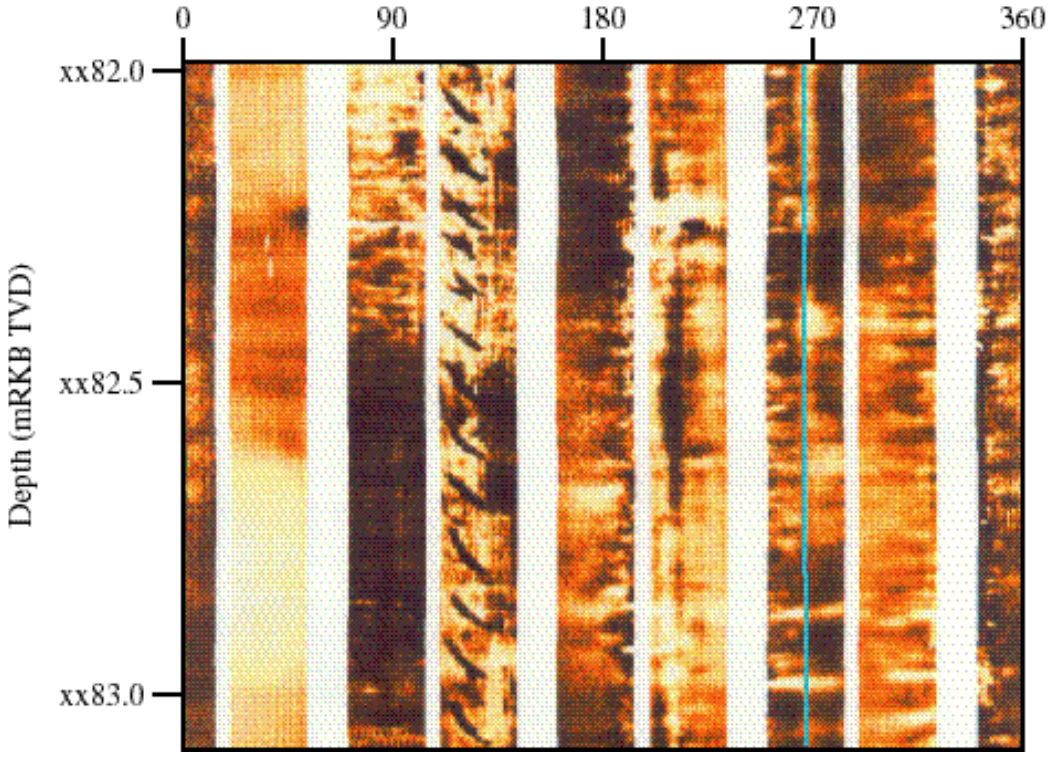

Figure B.6: FMI image of inclined drilling-induced tensile fractures in Visund well D. The tensile cracks appear at an azimuth of approximately 110˚ in this plot. No fractures are observed on the opposite side of the wellbore. This may be the result of reaming of the hole or keyseating in this case.

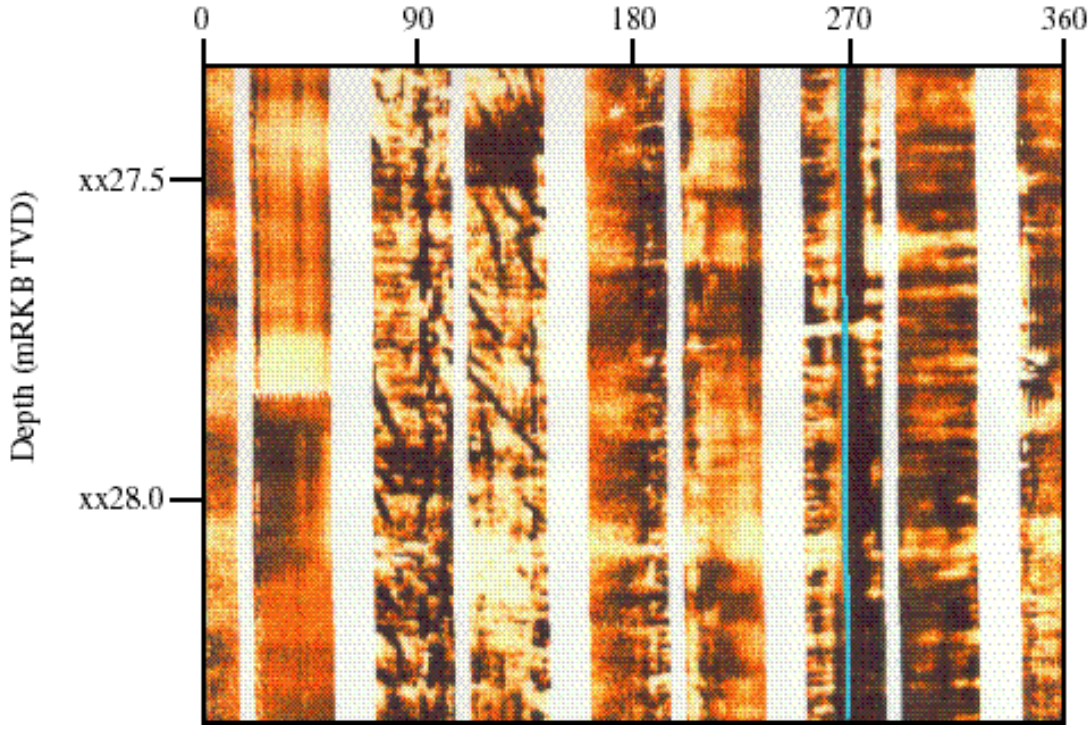

Figure B.7: FMI image of near-axial and inclined drilling-induced tensile fractures in Visund well D. The failures appear between approximately 80˚ and 110˚. Some inclined fractures appear to grow into the near-axial fracture in this image. The dark band beneath the pad 1 azimuth is a keyseat, as the wellbore is deviated in this direction.

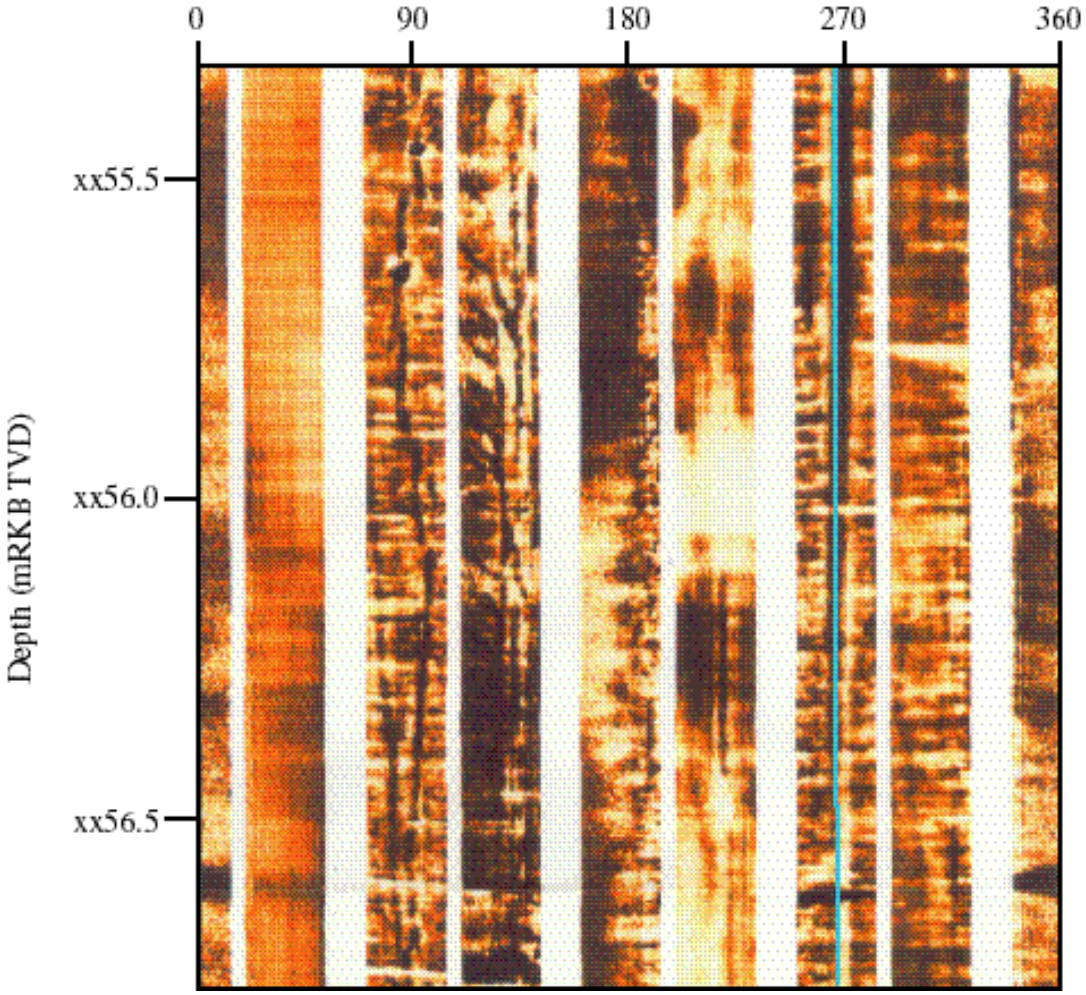

Figure B.8: FMI image of near-axial and inclined drilling-induced tensile fractures in Visund well D. The failures appear between approximately 90˚ and 120˚. There may be a near-axial fracture at 120˚ that has inclined fractures growing toward the main axial fracture at 90˚. A keyseat can be seen at 270˚.

APPENDIX C

USING INCLINED DRILLING INDUCED TENSILE FRACTURES TO CONSTRAIN THE VARIABILITY IN THE ORIENTATION OF THE STRESS TENSOR

Drilling-induced tensile fractures which are inclined with respect to the axis of a wellbore can be used to constrain the variability in the orientation of the stress tensor. Tensile fractures that are aligned with the axis of a vertical wellbore indicate the principal stresses are vertical and horizontal. Deviations of the principal stresses from vertical and horizontal will cause inclined drilling-induced tensile fractures to form in a vertical well, and the inclination of these fractures relative to the axis of the wellbore is related to the difference in orientation between the wellbore and the stress field. The program Stress and Failure of Inclined Boreholes (SFIB, Peska and Zoback, 1995) has been generalized to deal with cases in which the wellbore is deviated, and we use it here to analyze inclined drilling-induced tensile fractures in Visund.

In Visund wells 6, 8, 10S, and 11 we observe sporadic occurrences of tensile fractures inclined with respect to the axis of the wellbore (Chapter 2, Figure 2.2). Because only well 10S has a significant number of inclined fractures, we focus on this well. We split the inclined fractures into two sets, depending on the azimuth at which they formed (Figure C.1a). Fractures that formed at an azimuth of approximately 100˚ are shown in gray, and those at approximately 300˚ are shown in black. There are fewer tensile fractures at 300˚ due to the keyseating in well 10S, which tends to erode the tensile fractures. The azimuth of the data on this side of the hole is biased as a result, and does not show the expected average azimuth of 280˚. Figure C.1b shows the inclination of the fractures as a function of depth. We measure the fracture inclination counter-clockwise from the downhole direction (see insets of Figure C.1b). The fractures in this hole are typically inclined less than about 30˚ and more than about 150˚ (i.e. the angle between the fracture and the wellbore axis is typically less than about 30˚ to either side). Fig. C.1b shows that there is not a clear tendency for the fractures to be preferentially inclined in one direction. Fig. C.1c shows the azimuth of the inclined fractures plotted as a function of the inclination. The fractures generally fall into four groups. Each cluster represents fractures that have formed on the same side of the hole (e.g. at an azimuth of 100˚) at similar inclinations. The majority of data show the fractures are rotated less than 25˚ from the axial orientation on both sides of the hole. We use this observation to constrain the maximum deviation of the stress tensor from the typical orientation of vertical and horizontal. The gray and black lines shown in the middle of the figure illustrate the simplified observations of the inclined tensile fractures in well 10S. Inclined fractures formed at azimuths ranging between 60˚ and 150˚ on one side of the hole, and between 270˚ and 340˚ on the opposite side. The inclinations of the tensile fractures range between near-axial fractures (0˚) to 50˚ and from 115˚ back to near-axial fractures (180˚). We are able to reproduce the occurrence and orientation of the inclined tensile fractures shown in Figure C.1c using only minor perturbations to both the

orientation of the stress tensor and the mud weight in well 10S.

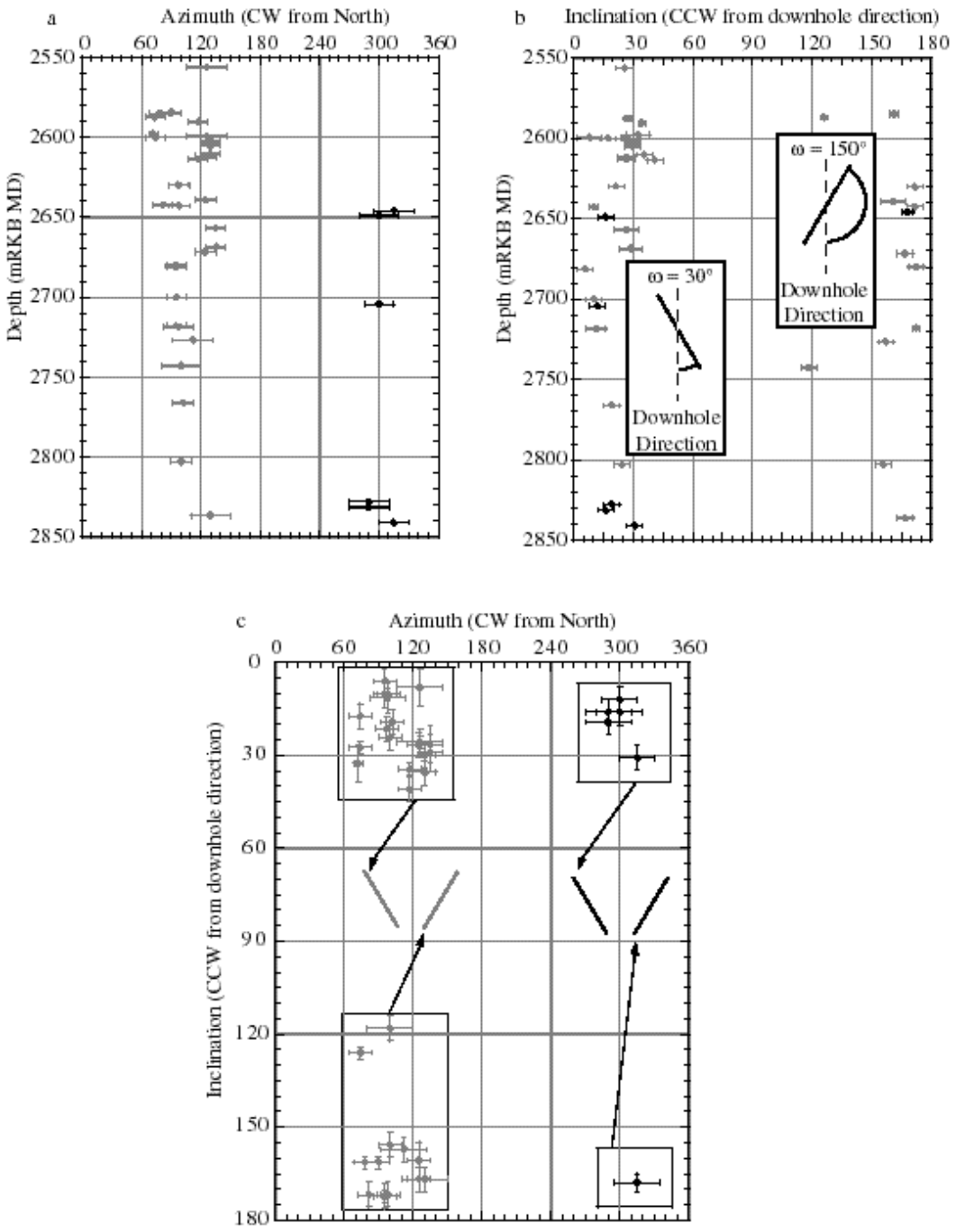

Figure C.1: a) Azimuth of inclined fractures versus measured depth. Fractures are split into two groups depending on side of the hole where they formed. b) Inclination of fractures with respect to downhole direction versus measured depth. Inclination of fractures remains relatively small throughout hole and has an average value of approximately 25˚ or 155˚. c) Azimuth of inclined fractures versus inclination measured counter-clockwise (ccw) from downhole direction. Simplified observations are shown in center of plot.

Figure C.2 shows the expected minimum tangential (hoop) stress and corresponding fracture inclination (omega) as a function of the azimuth within the wellbore. The azimuth within the wellbore is different from the azimuth of the wellbore (defined as an angle measured clockwise from north) and is defined as the angle measured clockwise from the low side of an inclined well (when looking down the hole) to a tensile or compressive failure. The low side of an inclined hole is easiest to imagine as the place where water would run if poured down the hole. In the first analysis we rotate S_{Hmax} 10˚ counter-clockwise (assuming a vertical principal stress), and increase ΔP by 3 MPa to a total of 9 MPa (Figure C.2a). Tensile fractures are expected to form when the minimum tangential stress exceeds the tensile rock strength. Because we assume the rock has zero tensile strength, tensile fractures should form when the minimum tangential stress at the wellbore wall becomes negative. In Figure C.2a the tensile rock strength is shown by the dashed zero stress line, and the minimum tangential stress is shown with the solid sinusoid. The gray shaded regions show the expected azimuths within the wellbore where tensile fractures should form. That is, they show the extent of the wellbore wall in tension. Hatched areas along the omega axis show the range of possible inclinations for the inclined fractures. This is determined by looking at how much of the thick-dashed fracture inclination line falls within the gray shaded region. According to this analysis, tensile fractures will form at any inclination between 155˚ and 25˚ (i.e. the maximum inclinations possible are ±25˚ from the wellbore axis). The two gray and the two black lines shown in the lower portion of the plot correspond to these inclinations. The lines also correspond to azimuths within the well from about 165˚ to 185˚, and from 345˚ to 5˚. Because well 10S is inclined to the west at an azimuth of 280˚, fractures that form at azimuths within the wellbore close to 0˚ and 180˚ (the low and high sides of the inclined hole) are in fact forming at azimuths measured from north of approximately 100˚ and 280˚. This model matches very well with the observations shown in Figure C.1. Fig. C.2b is the same as Fig. C.2a, except the azimuth of SHmax is rotated 10˚ clockwise. This analysis provides similar results to those found from Fig. C.2a. Thus, the stress state measured in Visund (Chapter 2) for well 10S predicts both the azimuth and inclination of the inclined tensile fractures, consistent with our observations from the FMI log.

The azimuth and inclination of the inclined tensile fractures can similarly be predicted by perturbing the vertical and minimum horizontal stresses by only 10˚ in any direction. Figure C.3 shows a cartoon demonstrating this. Therefore, the overall stress tensor can be accurately described with vertical and horizontal principal stresses, however the orientation of the stress tensor clearly deviates from this approximation by small amounts which can be estimated by modeling the inclined tensile fractures. The maximum inclination of the

tensile fractures to the wellbore axis is an indication of how much the stress tensor deviates from the orientation determined by examining tensile fractures aligned with the axis of the wellbore.

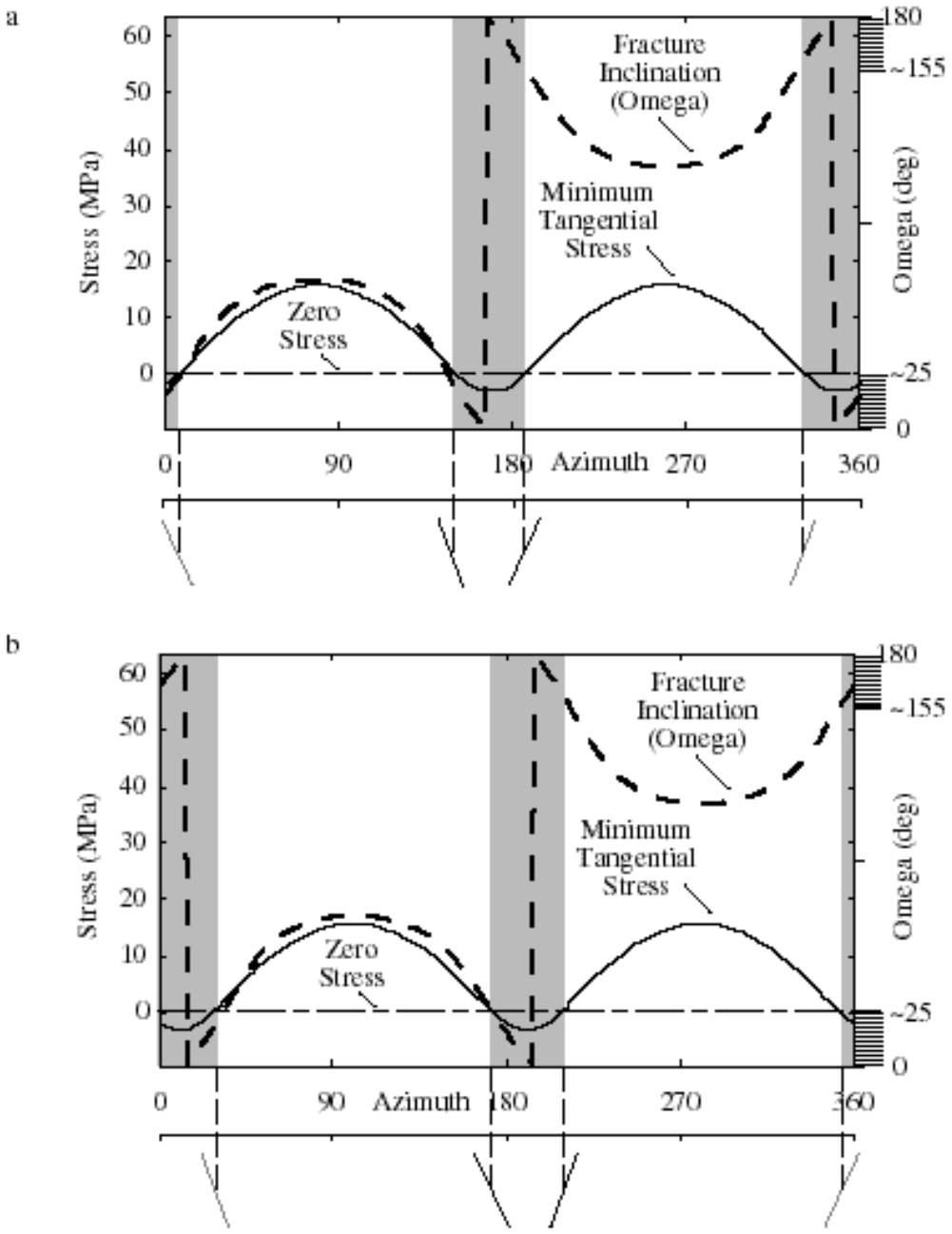

Figure C.2: a) Minimum tangential stress (hoop stress) around the well for a stress state in which the maximum horizontal stress has been rotated 10˚ counter-clockwise. A slight increase in the differential fluid pressure of 3 MPa is used in this analysis. The gray and black lines below the plot show the expected range of orientations of the inclined tensile fractures. In this case, the fractures should be inclined less than 25˚ or more than 155˚ (gray and black lines respectively). b) This plot is the same as in (a), except the maximum horizontal stress is rotated 10˚ clockwise.

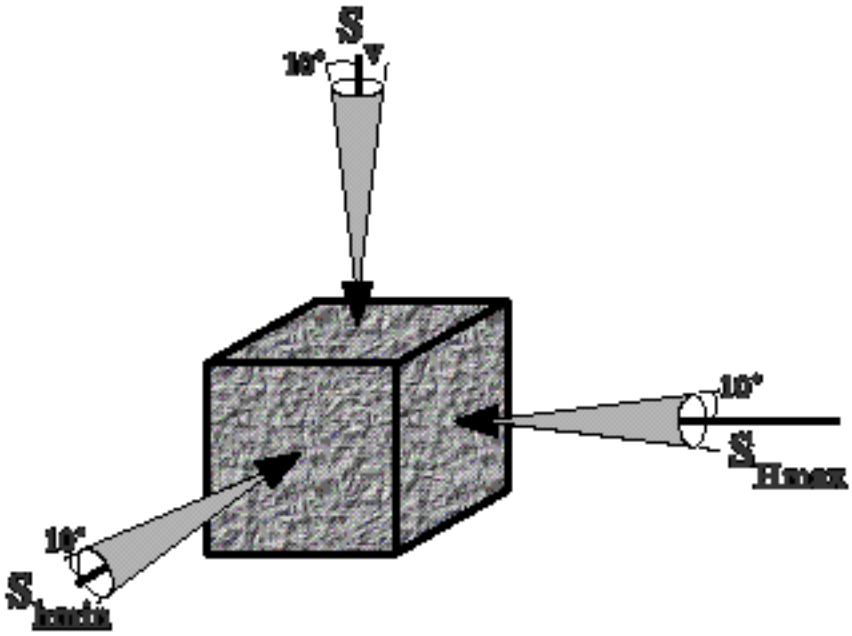

Figure C.3: Stress tensor in Visund. Cones show the variability in stress orientation as determined by modeling inclined drilling-induced tensile fractures.

APPENDIX D

INFLUENCE OF THERMOPOROELASTICITY ON DRILLING-INDUCED TENSILE FRACTURES

D.1 Introduction

The initiation of drilling-induced tensile fractures is influenced by a number of factors such as the stress anisotropy around the wellbore, differences between the mud and pore pressures, and thermal stresses. In this study we examine the influence of thermal stresses on the formation of drilling-induced tensile fractures using thermoporoelasticity and compare the steady state solution (SSS) of Moos and Zoback (1990) used in Chapters 2 and 4 with the exact analytical solution (EAS) derived by Li et al (1998). This work follows the work of Colmenares and Zoback (2000) which compared the SSS, EAS, and a numerical thermoporoelastic approach used by Brudy and Kjørholt (1999). The work of Colmenares and Zoback shows the Brudy and Kjørholt approach does not provide reasonable results, and that the SSS is a good approximation of the EAS for the input values provided by Brudy and Kjørholt (1999). In this study we use the input values of stress, temperature, and material properties from well 10S in the Visund field to explore the differences between the SSS and EAS.

D.2 Input data and results

Tensile fractures in well 10S stopped at a depth of approximately 2830 mTVD. The thermally-induced tangential stresses at the wellbore wall were modeled using the BSFO module of SFIB. The material properties are shown in table 1. Material properties were derived from published measurements of various rocks. The reference is shown in the third column. The parameters are shown in table 2. Parameters reflect measurements made in the wellbore at the appropriate depth, or values derived from direct measurements in the wellbore. The final column in both tables shows whether the value was required for input into either the SSS, EAS, or both. Note that significantly more data is required to arrive at a value for the EAS. While the EAS should be more accurate than the SSS, the opportunity to introduce error is far greater with the EAS because of the greater number of input parameters an material property values required for this solution.

Figure 1 shows a comparison of the output values of the SSS and EAS. The SSS shows the added tensile stress at the wellbore wall as a result of the cooling is only 1.3 MPa. The EAS shows the wellbore does not go into tension until approximately 100 minutes (1hr, 40min) have elapsed, and reaches the maximum tension of 0.6 MPa after 10000 minutes (6days, 22hrs, 40min). The tensile stresses caused by cooling are small in both cases, supporting our claim in Chapter 2 that the stress perturbation due to cooling in this field is insignificant. Note that the resulting stress from the SSS is very similar to the EAS. This

supports the claim of Colmenares and Zoback (2000) that the Moos and Zoback (1990) approximation is sufficient to estimate the stresses caused by cooling of the wellbore.

TABLE D1.

Material Property	Value	Reference	EAS/SSS
Skempton's Coeff.	0.6	-	EAS
Biot Coefficient	1	Fjær et al. (1992)	EAS/SSS
Coeff. of Int. Friction	1	-	EAS/SSS
Fluid Diffusivity	5.5×10^{-7} m^2/s	Somerton(1992)	EAS
Thermal Diffusivity	1.8×10^{-6} m^2/s	Somerton (1992)	EAS
Coeff. Therm. Expan.	1.8×10^{-5} $°K^{-1}$	Somerton (1992)	EAS/SSS
Co. Ther. Exp. (mud)	1.67×10^{-4} $°K^{-1}$	Somerton (1992)	EAS
Poisson's Ratio	0.25	Jumikis (1983)	EAS/SSS

TABLE D2.

Parameter	Value	EAS/SSS
S_{Hmax}	71.5 MPa	EAS/SSS
S_v	55.1 MPa	EAS/SSS
S_{hmin}	53.2 MPa	EAS/SSS
Pore Pressure	42.9 MPa	EAS/SSS
Mud Weight	49 MPa	EAS/SSS
Delta T	-30	EAS/SSS
Young's Modulus	1.8 GPa	SSS
Bulk Modulus	0.72 GPa	EAS
Permeability	1.37 D	EAS
Porosity	0.2	EAS
Tau	168.7	SSS
Density	2000 kg/m^3	EAS/SSS

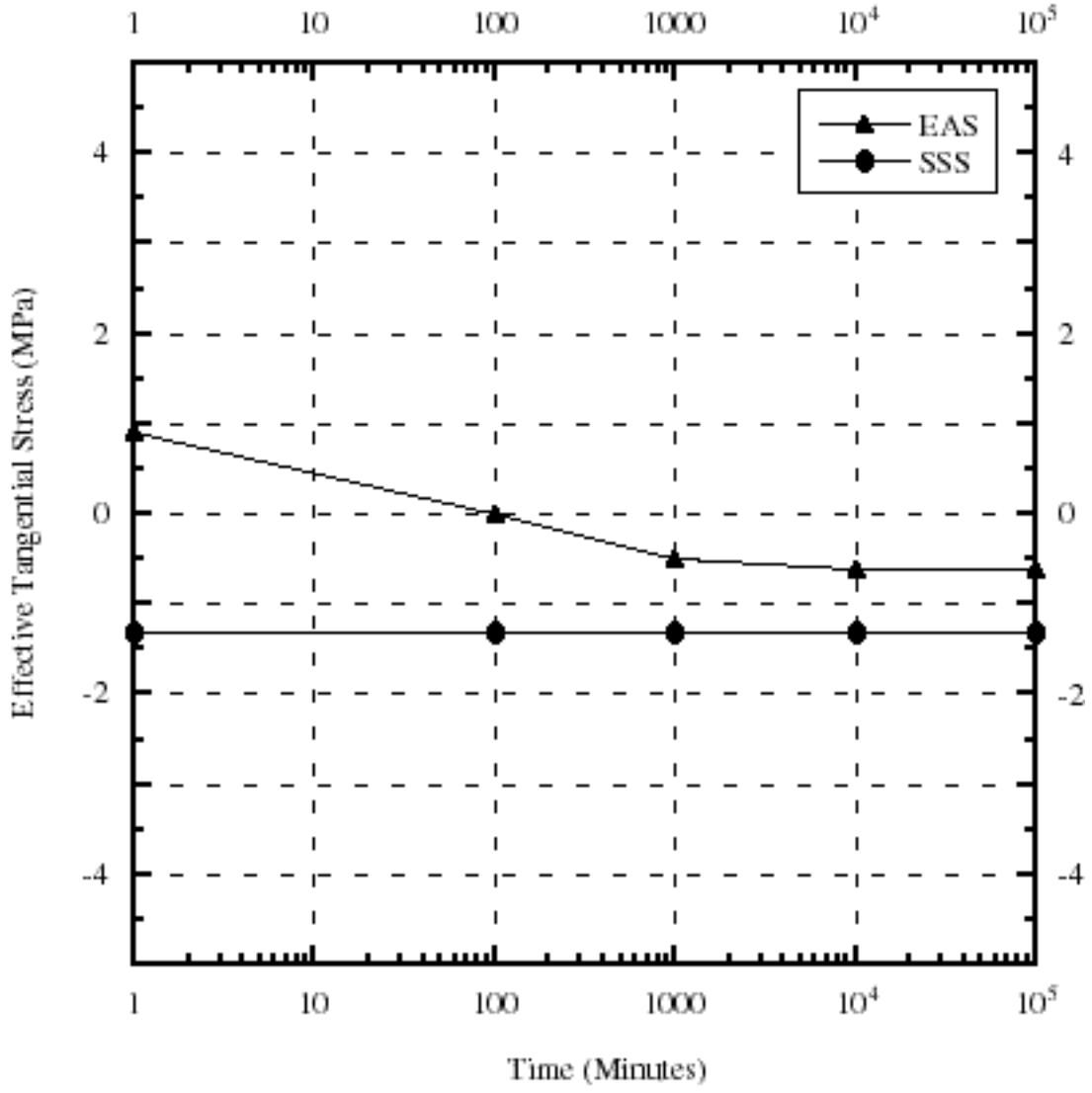

Figure D.1: Effective tangential stress at the wellbore wall as a function of time for the exact analytical solution (EAS, triangles) and the steady state solution (SSS, circles). When errors from the model inputs are considered, the two solutions are essentially identical after 10000 minutes.

REFERENCES

Aadnoy, B. S., 1990. In-situ stress direction from borehole fracture traces: J. Pet. Sci. Eng., 4, 143-153.

Ayatollahi, M. S., J. Noorishad, and P. A. Witherspoon, 1983. Stress-fluid flow analysis of fractured rock. J. Eng. Mech., 109, 1-13.

Barton, C.A., Hickman, S.H., Morin, R., Zoback, M.D., and Benoit, D., 1998, Reservoir-scale fracture permeability in the Dixie Valley, Nevada, geothermal field, in Proceedings of SPE/ISRM Rock Mechanics in Petroleum Engineering, Trondheim, Norway, v. 2, Society of Petroleum Engineers, p. 315-322.

Barton, C.A., and M.D. Zoback, 1994. Stress perturbations associated with active faults penetrated by boreholes; possible evidence for near-complete stress drop and a new technique for stress magnitude measurement. J. Geophys. Res., 99:5, 9373-9390.

Barton, C.A., Zoback, M.D., and Moos, D., 1995, Fluid flow along potentially active faults in crystalline rock: Geology, v. 23, p. 683-686.

Borgerud, L. and E. Svare, 1995. In-situ stress field on the Norwegian Margin, 62˚-67˚ north. in Proceedings of the Workshop on Rock Stresses in the North Sea, Trondheim, Norway, Feb 13-14, SINTEF Rock and Mineral Engineering, p. 169-178.

Bratli, R. K. and R. Risnes, 1981. Stability and failure of sand arches. Soc. Pet. Eng. J., April, 236-248.

Brudy, M., 1995. Determination of in-situ stress magnitude and orientation to 9 km depth at the KTB site. Doctoral Thesis: Karlsruhe.

Brudy, M., and Zoback, M.D., 1993, Compressive and tensile failure of boreholes arbitrarily-inclined to principal stress axes: Application to the KTB boreholes, Germany: International Journal of Rock Mechanics and Mining Sciences and Geomechanics Abstracts, v. 30, p. 1035-1038.

Brudy, M., and Zoback, M.D., 1999, Drilling-induced tensile wall-fractures: implications for determination of in-situ stress orientation and magnitude: International Journal of Rock Mechanics and Mining Sciences, v. 36, p. 191-215.

Brudy, M., Zoback, M.D., Fuchs, K., Rummel, F., and Baumgaertner, J., 1997, Estimation of the complete stress tensor to 8km depth in the KTB scientific drill holes: Implications for crustal strength: Journal of Geophysical Research, v. 102, p. 18453-18475.

Byerlee, J. D., 1978. Friction of Rocks: Pure and Applied Geophysics, 116, 615-629.

Castillo, D.A. and Zoback, M.D., 1994. Systematic variations in stress state in the southern San Joaquin valley: Inferences based on well-bore data and contemporary seismicity. American Association of Petroleum Geologists Bulletin, 78:8, 1257-1275.

Dart, C., O. H. Inderhaug, O. Kløvjan, and C. Ottesen, 1995. Present day stress regime in the Barents Sea from borehole breakout. in Proceedings of the Workshop on Rock Stresses in the North Sea, Trondheim, Norway, Feb 13-14, SINTEF Rock and Mineral Engineering, p. 179-190.

Doré, A.G., and Lundin, E.R., 1996. Cenozoic compressional structures on the NE Atlantic margin: nature, origin and potential significance for hydrocarbon exploration. Petroleum Geoscience, V.2, 299-311.

Ekstrom, M.P, C.A. Dahan, M.Y.Chen, P.M. Lloyd, D.J. Rossi, 1986. Formation imaging with microelectrical scanning arrays. In: Transactions of the SPWLA Annual Logging Symposium. 27, BB1-BB21.

Engelder, T. and Fischer, M.P., 1994. Influence of poroelastic behavior on the magnitude of minimum horizontal stress, Sh, in overpressured parts of sedimentary basins. Geology, 22, 949-952.

Færseth, R.B., Sjøblom, T.S., Steel, R.J., Liljedahl, T., Sauar, B.E., and Tjelland, T., 1995, Tectonic controls on Bathonian-Volgian syn-rift successions on the Visund fault block, northern North Sea, in Steel, R.J., et al., eds., Sequence stratigraphy on the northwest European margin: Elsevier, Amsterdam, p. 325-346.

Fejerskov, M. ,1996. Determination of in-situ rock stresses related to petroleum activities on the Norwegian continental shelf. Doctoral Thesis: Department of Geology and Mineral Resources Engineering, Norwegian University of Science and Technology.

Fejerskov, M., A. M. Myrvang, C. Lindholm, and H. Bungum, 1995. In-situ rock stress pattern on the Norwegian continental shelf and mainland. in Proceedings of the Workshop on Rock Stresses in the North Sea, Trondheim, Norway, Feb 13-14, SINTEF Rock and Mineral Engineering, p. 191-201.

Finkbeiner, T., Zoback, M.D., Stump, B., and Flemings, P., 1998, In situ stress, pore pressure, and hydrocarbon migration in the South Eugene Island Field, Gulf of Mexico, in Mitchell, A., and Grauls, D., eds., Overpressures in petroleum exploration, workshop proceedings: Elf Aquitaine Memoir 72, Pau, France, p. 103-110.

Fjær, E., Holt, R.E., Horsrud, P., Raaen, A.M. and Risnes, R. 1992. Petroleum related rock mechanics. Developments in Petroleum Science v. 33, Chilingarian, G.V., ed. Elsevier.

Gaarenstroom, L., R. A. J. Tromp, M. C. de Jong, and A. M. Brandenburg, 1993. Overpressures in the Central North Sea: implications for trap integrity and drilling safety. Geology of Northwest Europe: Proceedings of the 4th Conference (J. R. Parker, ed.), 1305-1313.

Gough, D. I. and Bell J. S., 1981. Stress orientations from borehole wall fractures with examples from Colorado, east Texas, and northern Canada: Can. J. Earth Sci., 19, 1358-

1370.

Grollimund, B., and Zoback, M.D., 2000, Post glacial lithospheric flexure and induced stresses and pore pressure changes in the northern North Sea, Tectonophysics (in press).

Grollimund, B., Zoback, M.D., and Arnesen, L., 1998, Flexurally-induced stresses in the northern North Sea: Preliminary comparison of observation and theory, in Proceedings of SPE/ISRM Rock Mechanics in Petroleum Engineering, Trondheim, Norway, v. 1, Society of Petroleum Engineers, p. 189-198.

Hickman, S., Sibson, R., and Bruhn, R., 1992, Introduction to special section: Mechanical interaction of fluids in faulting: Journal of Geophysical Research, v. 100, p. 8749-8764.

Hickman, S.H., Zoback, M.D., and Benoit, R., 1998, Tectonic controls on fault-zone permeability in a geothermal reservoir at Dixie Valley, Nevada, in Proceedings of SPE/ISRM Rock Mechanics in Petroleum Engineering, Trondheim, Norway, v. 1, Society of Petroleum Engineers, p. 79-86.

Healy, J.H., Rubey, W.W., Griggs, D.T., and Raleigh, C.B., 1968, The Denver earthquakes: Disposal of waste fluids by injection into a deep well has triggered earthquakes near Denver, Colorado: Science, v. 161, p. 1301-1310.

Hermanrud, C., B. Norgard, H. Mari, C. Fichler, A. Rornes, R. Heggland, 1997. Studies of hydrocarbon migration; an important discipline in hydrocarbon exploration. AAPG Bulletin, 81-8, 1383.

Hunt, J.M., 1990, Generation and migration of petroleum from abnormally pressured fluid compartments: American Association of Petroleum Geologists Bulletin, v. 74, p. 1-12.

Jumikis, A.R., 1983. Rock Mechanics. Series on Rock and Soil Mechanics Vol. 7. Trans Tech Publications.

Jørgensen, T., and R.K. Bratli, 1995. In-situ stress determination and evaluation at the Tampen Spur area. in Proceedings of the Workshop on Rock Stresses in the North Sea, Trondheim, Norway, Feb 13-14, SINTEF Rock and Mineral Engineering, p. 240-249.

Kennedy, B.M., Kharaka, Y.K., Evans, W.C., Ellwood, A., DePaolo, D.J., Thordsen, J., Ambats, G., and Mariner, R.H., 1997, Mantle fluids in the San Andreas fault system, California: Science, v. 278, p. 1278-1281.

Klemann, V., and Wolf, D., 1998, Modeling of stresses in the Fennoscandian lithosphere induced by Pleistocene glaciations: Tectonophysics, v. 294, p. 291-303.

Linde, A.T., Sacks, I.S., Johnston, M.J.S., Hill, D.P., and Bilham, R.G., 1994, Increased pressure from rising bubbles as a mechanism for remotely triggered seismicity: Nature, v. 371, p. 408-410.

Lindholm, C.D., Bungum, H., Villagran, M., and Hicks, E., 1995, Crustal stress and tecton-

ics in Norwegian regions determined from earthquake focal mechanisms, in Proceedings of the Workshop on Rock Stresses in the North Sea, Trondheim, Norway, Feb 13-14, SINTEF Rock and Mineral Engineering, p. 77-91.

Mardia, K.V., 1972. Statistics of directional data. Academic Press, 357p.

Moos, D., and Zoback, M.D., 1990, Utilization of observations of well bore failure to constrain the orientation and magnitude of crustal stresses: Application to continental, Deep Sea Drilling Project, and Ocean Drilling Program boreholes: Journal of Geophysical Research, v. 95, p. 9305-9325.

Müller, B., Zoback, M. L., Fuchs, K., Mastin, L., Gregersen, S., Pavoni, N., Stephansson, O., and Ljunggren, C., 1992. Regional patterns of tectonic stress in Europe: J. Geophys. Res., 97:B8, 11,783-11,803.

Nur, A. M., and J. Walder, 1990. Time-dependent hydraulics of the Earth's crust. In: Geophysics Study Committee, National Research Council, 1990, The role of fluids in crustal processes. National Academy Press, 113-127.

Paillet, F.L. and K. Kim, 1987. Character and distribution of borehole breakouts and their relationship to in situ stresses in deep Columbia River Basalts. J. Geophys. Res., 92:7, 6223-6234.

Peska, P. and Zoback, M. D., 1995. Compressive and tensile failure of inclined well bores and determination of in situ stress and rock strength: J. Geophys. Res., 100:B7, 12,791-12811.

Peska, P. and M. D. Zoback, 1996. Stress and failure of inclined boreholes. Stanford University Department of Geophysics.

Plumb, R.A. and Cox, J.W., 1987. Stress directions in eastern North America determined to 4.5 km from borehole elongation measurements. Journal of Geophysical Research, v.90, 5513-5522.

Plumb, R. A. and Hickman, S. H., 1985. Stress induced borehole elongation: a comparison between the four-arm dipmeter and the borehole televiewer in the Auburn geothermal well: J. Geophys. Res., 90, 5513-5521.

Raleigh, C.B., Healy, J.H., and Bredehoeft, J.D., 1976, An experiment in earthquake control at Rangeley, Colorado: Science, v. 191, p. 1230-1237.

Rohrman, M., van der Beek, P., Andriessen, P., Cloetingh, S., 1995. Meso-Cenozonic morphotectonic evolution of southern Norway: Neogene domal uplift inferred from apatite fission track thermochronology. Tecnonics, V.14, No.3, 704-718.

Sahagian, D.L., and Proussevitch, A.A., 1992, Bubbles in volcanic systems: Nature, v. 359, p. 485.

Shamir, G. and M.D. Zoback, 1992. Stress orientation profile to 3.5 km depth near the San

Andreas Fault at Cajon Pass, California. J. Geophys. Res., 97:4, 5059-5080.

Sibson, R.H. 1981. Fluid flow accompanying faulting: field evidence and models. *In*: Simpson, D.W. and Richards, P.G. (eds) Earthquake prediction: an international review, American Geophysical Union Maurice Ewing Series for Geophysical Monographs, v.4, 593-603.

Sibson, R.H., 1992, Implications of fault-valve behaviour for rupture nucleation and recurrence, in Mikumo, T., Aki, K., Ohnaka, M., Ruff, L.J., and Spudich P.K.P., eds., Earthquake source physics and earthquake precursors: Tectonophysics, v. 211., p. 283-293.

Somerton, S., 1992. Thermal properties and temperature-related bahavior of rock/fluid systems. Elsevier.

Stephansson, O., 1988, Ridge push and glacial rebound as rock stress generators in Fennoscandia: Bulletin of the Geological Institutions of the University of Uppsala, N.S., v. 14, p. 39-48.

Sturtevant, B., Kanamori, H., and Brodsky, E.E., 1996, Seismic triggering by rectified diffusion in geothermal systems: Journal of Geophysical Research, v. 101, p. 25269-25282.

Teufel, L. W.,1992. Production-induced changes in reservoir stress state; applications to reservoir management. In: SEG Annual Meeting Expanded Technical Program Abstracts with Biographies. 62, 1381.

Trimmer, D., D. Bonner, C. H. Heard, and A. Duba, 1980. Effect of pressure and stress on water transport in intact and fractured gabbro and granite. J. Geophys, Res., 85, 7059-7071.

Tsang, Y. W. and P. A. Witherspoon, 1981. Hydromechanical behavior of a deformable rock fracture subject to normal stress. J. Geophys. Res., 86, 9287-9298.

Vågnes, E., Gabrielsen, R.H., Haremo, P., 1998. Late Cretaceous-Cenozoic intraplate contractional deformation a the Norwegian continental shelf: timing, magnitude and regional implications. Tecnonophysics, V.300, 29-46.

Vernik, L., M. Bruno, and C. Bovberg, 1993. Empirical relations between compressive strength and porosity of siliciclastic rocks. Int. J. Rock Mech. Min. Sci. & Geomech. Abstr., 30:7, 677-680.

Wiprut, D.J., and Zoback, M.D., 2000, Constraining the full stress tensor in the Visund field, Norwegian North Sea: Application to wellbore stability and sand production. International Journal of Rock Mechanics and Mining Sciences. v.37, 317-336.

Wiprut, D., and Zoback, M.D., 2000, Fault reactivation and fluid flow along a previously dormant normal fault in the northern North Sea. Geology. 28:7, 595-598.

Wiprut, D. J., M. D. Zoback, P. Peska, and T. H. Hanssen, 1997. Constraining the full

stress tensor from observations of drilling-induced tensile fractures and leak-off tests: application to borehole stability and sand production on the Norwegian margin. Int. J. Rock Mech. & Min. Sci. 34:3-4, Paper No. 00365.

Zhang, Y. Z., M. B. Dusseault, and R. K. Bratli, 1995. Simulating stresses in overpressured zones using a finite element approach. in Proceedings of the Workshop on Rock Stresses in the North Sea, Trondheim, Norway, Feb 13-14, SINTEF Rock and Mineral Engineering, p. 108-126.

Zoback, M. D., Apel, R., Baumgärtner, J., Brudy, M., Emmermann, R., Engeser, B., Fuchs, K., Kessel, W., Rischmüller, H., Rummel, F., and Vernik, L., 1993. Upper crustal strength inferred from stress measurements to 6 km depth in the KTB borehole: Nature, 365, 633-635.

Zoback, M. D., C. A. Barton, M. Brudy, C. T. Chang, D. Moos, P. Peska, and L. Vernik, 1995. A review of some new methods for determining the in situ stress state from observations of borehole failure with applications to borehole stability and enhanced production in the North Sea. in Proceedings of the Workshop on Rock Stresses in the North Sea, Trondheim, Norway, Feb 13-14, SINTEF Rock and Mineral Engineering, p. 6-21.

Zoback, M.D., and Harjes, H.P., 1997, Injection-induced earthquakes and crustal stress at 9km depth at the KTB deep drilling site, Germany: Journal of Geophysical Research, v. 102, p. 18477-18491.

Zoback, M. D., Moos, D., Mastin, L. and Anderson, R. N., 1985. Wellbore breakouts and in-situ stress: J. Geophys. Res., 90, 5523-5530.

Zoback, M. L., 1992. First and second order patterns of tectonic stress: the world stress map project. J. Geophys. Res., 97:11, 703-711.

Zoback, M.L., and Zoback, M.D., 1980. Faulting patterns in north-central Nevada and strength of the crust. Journal of Geophysical Research, 85:B1, 275-284.

Zoback, M.L., and Zoback, M.D., 1980. State of stress in the coterminous United States: Journal of Geophysical Research, v.85, 6113-6156.

Zoback, M.L., and Zoback, M.D., 1989. Tectonic stress field of the continental United States, in Pakiser, L.C., and Mooney, W.D., Geophysical framework of the continental United States: Boulder, Colorado, Geological Society of America Memoir 172.